Exploiting Near Field and Surface Wave Propagation for Implantable Devices

by

Jordan Besnoff

Department of Electrical and Computer Engineering
Duke University

Date: ____________________________
Approved:

Matthew Reynolds, Co-Supervisor

Steven Cummer, Co-Supervisor

Loren Nolte

Jeffrey Krolik

Angel Peterchev

Dissertation submitted in partial fulfillment of the requirements for the degree of
Doctor of Philosophy in the Department of Electrical and Computer Engineering
in the Graduate School of Duke University
2014

Abstract

Exploiting Near Field and Surface Wave Propagation for Implantable Devices

by

Jordan Besnoff

Department of Electrical and Computer Engineering
Duke University

Date: __________________________
Approved:

Matthew Reynolds, Co-Supervisor

Steven Cummer, Co-Supervisor

Loren Nolte

Jeffrey Krolik

Angel Peterchev

An abstract of a dissertation submitted in partial fulfillment of the requirements for
the degree of Doctor of Philosophy in the Department of Electrical and Computer
Engineering
in the Graduate School of Duke University
2014

Abstract

This thesis examines the bandwidth shortcomings of conventional inductive coupling biotelemetry systems for implantable devices, and presents two approaches toward an end-to-end biotelemetry system for reducing the power consumption of implanted devices at increased levels of bandwidth. By leveraging the transition zone between the near and far field, scattering in the near field at UHF frequencies for increased bandwidth at low power budgets can be employed. Additionally, taking advantage of surface wave propagation permits the use of single-wire RF transmission lines in biological tissue, offering more efficient signal routing over near field coupling resulting in controlled implant depth at low power budgets.

Due to the dielectric properties of biological tissue, and the necessity to operate in the radiating near field to communicate via scattered fields, the implant depth drives the carrier frequency. The information bandwidth supplied by each sensing electrode in conventional implants also drives the operating frequency and regime. At typical implant depths, frequencies in the UHF range permit operation in the radiating near field as well as sufficient bandwidth.

Backscatter modulation provides a low-power, high-bandwidth alternative to conventional low frequency inductive coupling. A prototype active implantable device presented in this thesis is capable of transmitting data at 30 Mbps over a 915 MHz link while immersed in saline, at a communication efficiency of 16.4 pJ/bit. A prototype passive device presented in this thesis is capable of operating battery-free, fully immersed in saline, while transmitting data at 5 Mbps and consuming 1.23 mW. This prototype accurately demodulates neural data while immersed in saline at a distance of 2 cm. This communication distance is extended at similar power budgets by exploiting surface wave propagation along a single-wire transmission line. Theoretical models of single-wire RF transmission lines embedded in high permittivity and conductivity dielectrics are validated by measurements. A single-wire transmission line of radius 152.4 μm exhibits a loss of 1 dB/cm at 915 MHz in saline, and extends the implant depth to 6 cm while staying within SAR limits.

This work opens the door for implantable biotelemetry systems to handle the vast amount of data generated by modern sensing devices, potentially offering new insight into neurological diseases, and may aid in the development of BMI's.

To my Mom and Dad, and to my brother Jamie and sister Shaina – you are all the reason I strive for success

Contents

List of Tables

List of Figures

List of Abbreviations

ADC Analog to digital converter. 3

AM Amplitude modulation. 48, 49

ASIC Application specific integrated circuit. 13, 69, 88

BMI Brain-machine interface. 1, 6

DC Direct current. 2, 52

EM Electromagnetic. 3, 22–24, 29, 30, 43, 144, 157, 158, 162

FCC Federal communications commission (exists in the USA). 3

HF High frequency. 2, 31, 130

IC Integrated circuit. 73, 131

IMD Implantable microelectronic device. 4

ISI Intersymbol interference. 51, 52

ISM Industrial, scientific, and medical radio band. In North America, the UHF ISM band ranges from 902 – 928 MHz. 4, 60, 117, 118, 130

Mbps Megabits per second. 4

PM Phase modulation. 49

Q Quality factor. 2, 3, 31, 40, 41, 47, 50–52, 57

RF Radio frequency. 1, 8, 110

SAR Specific absorption rate. 10, 12, 60, 132

SNR Signal to noise ratio. 18, 22, 132

SWTL Single wire transmission line. 109, 110, 115–122, 126–128, 133, 134

TEM Transverse electromagnetic. 144–146

UHF Ultra High Frequency (300 MHz – 1 GHz). 4, 5, 11, 56, 57, 59, 60, 62, 67, 117, 118, 130

VNA Vector network analyzer. 115

List of Symbols

σ_a Alternating field conductivity, measured in S/m. 26, 27

σ_e Equivalent conductivity, measured in S/m. 26, 27, 29, 30, 144, 146, 159–162

σ_s Static field conductivity, measured in S/m. 26, 27, 158

σ Conductivity, measured in S/m. 26

$\tan\delta_a$ Alternating electric loss tangent. 27

$\tan\delta_e$ Effective electric loss tangent. 26, 27, 29

$\tan\delta_s$ Static electric loss tangent. 27

a Radius of small loop antenna (meters). 17

α Attenuation constant (Np/m). 29, 30, 33, 162

$\vec{B}$ Complex spatial magnetic flux density (webers/square meter). 27, 157, 158

β Phase propagation constant (rad/m). 29, 150, 151, 162

$\vec{\mathcal{B}}$ Time-varying magnetic flux density (webers/square meter). 156, 157, 161

D Maximum antenna dimension, in units of meters. 20, 23, 138, 144, 150, 151, 154

δ Skin depth. 30

$\vec{D}$ Complex spatial electric flux density (coulombs/square meter). 24, 157, 158

$\vec{\mathcal{D}}$ Time-varying electric flux density (coulombs/square meter). 156, 157, 160

$\vec{E}$ Complex spatial electric field intensity (volts/meter). 18, 26, 157, 158, 162

ϵ_0 Permittivity of free space, 8.854×10^{-12} F/m. 25, 100, 145, 146, 151, 161

ϵ Permittivity, measured in F/m. xxiii, 23–26, 158, 160

$\vec{\mathcal{E}}$ Time-varying electric field intensity (volts/meter). Function of time and space: $\vec{\mathcal{E}} = \vec{\mathcal{E}}(x, y, z; t)$. 24, 156, 157, 159–161

ϵ' Real part of permittivity (ϵ). 25–27, 29, 144, 159–162

ϵ'_e Effective real part of permittivity. 27

E_ϕ Complex spatial electric field in the ϕ direction. 17, 145

ϵ'' Imaginary part of permittivity (ϵ). 25–27

ϵ''_e Effective imaginary part of permittivity. 27

ϵ''_r Imaginary part of relative permittivity. 25

ϵ'_r Real part of relative permittivity. 25, 30, 161

E_r Complex spatial electric field in the r direction. 15

E_r Electric field component in the radial direction using spherical coordinates, in units of V/m. 151

ϵ_r Relative permittivty. 25

η Wave impedance (material dependent). 15, 17, 20, 144–146

E_θ Complex spatial electric field in the θ direction. 15, 20, 145

γ_ρ^d Propagation constant in the ρ direction in dielectric wire coating. 98

γ_ρ^m Propagation constant in the ρ direction in surrounding dielectric medium. 100

γ Propagation constant. 29, 162

γ_z Propagation constant in z (axial) direction. 100

$\vec{H}$ Complex spatial magnetic field intensity (amperes/meter). 18, 26, 27, 157, 158, 161, 162

$\vec{\mathcal{H}}$ Time-varying magnetic field intensity (amperes/meter). 156, 157, 159–161

H_ϕ Complex spatial magnetic field in the ϕ direction. 15, 145

H_r Complex spatial magnetic field in the r direction. 17

H_θ Complex spatial magnetic field in the θ direction. 17, 145

I Electric current, measured in Amps. 15, 17, 151

$\vec{J}$ Complex spatial current density (amperes/square meter). 157

$\vec{\mathcal{J}}$ Time-varying current density (amperes/square meter). 157

$\vec{J}_c$ Complex spatial conduction electric current density (amperes/square meter). 26, 158

$\vec{\mathcal{J}}_c$ Time-varying conduction electric current density (amperes/square meter). 156

$\vec{\mathcal{J}}_d$ Time-varying displacement electric current density (amperes/square meter). 156, 157

$\vec{J}_i$ Complex spatial impressed (source) electric current density (amperes/square meter). 26, 158

$\vec{\mathcal{J}}_i$ Time-varying impressed (source) electric current density (amperes/square meter). 156, 159–161

k Wavenumber (spatial) - equivalent to $\frac{2\pi}{\lambda}$. 15, 17–20, 138, 143, 145

k_0 Wavenumber in free space. 100

k_d Complex wavenumber in dielectric wire coating. 100

k_m Complex wavenumber in surrounding dielectric medium. 100

λ Wavelength. xxiv, 19, 20, 23, 138, 143, 144, 150, 154

l Wire length (meters). 15

$\vec{\mathcal{M}}_d$ Time-varying displacement magnetic current density (volts/square meter). 156, 157

$\vec{M}_i$ Complex spatial impressed (source) magnetic current density (volts/square meter). 158

$\vec{\mathcal{M}}_i$ Time-varying impressed (source) magnetic current density (volts/square meter). 156, 159–161

P Point in space. 148, 151, 153

PL Total path loss. 23

PL_a Path loss due to absorption of electromagnetic energy. 23

PL_s Path loss due to spreading effects. 23

P_r Received power. 18

q_{ev} Complex spatial electric charge density (coulombs/cubic meter). 157, 158

$\mathcal{Q}_{ev}$ Time-varying electric charge density (coulombs/cubic meter). 156, 157, 160, 161

q_{mv} Complex spatial magnetic charge density (webers/cubic meter). 157, 158

$\mathcal{Q}_{mv}$ Time-varying magnetic charge density (webers/cubic meter). 157, 161

Δr Difference in path length between the middle of the phase front and a separate point on the phase front. 152–154

r' Distance from midpoint of antenna to point in space. xxv, 148–151

r Distance from point on antenna to point in space. 15, 17, 18, 20, 23, 143, 145, 146, 148–154

θ Angle between antenna and line r'. 148–151

μ_0 Permeability of free space, $4\pi \times 10^{-7}$ H/m. 28, 100, 145, 146, 161

μ_r Relative magnetic permeability (dimensionless). 28

μ Magnetic permeability, measured in H/m. 23, 24, 28–30, 34, 42, 43, 144, 158–162

μ' Real part of magnetic permeability. 28, 161

μ'' Imaginary part of magnetic permeability. 28

μ_r'' Imaginary part of relative magnetic permeability. 28

μ_r' Real part of relative magnetic permeability. 28, 161

c Speed of light in a vacuum – approximately 2.998×10^8 meters/sec. 161

v Wave propagation speed (meters/sec). 161

ω Angular frequency, measured in radians/second. 23, 25–30, 38, 39, 41–46, 144, 151, 157, 158, 162

Acknowledgements

I consider myself very lucky to have had the opportunity to work with a great group of people over the past 5 years, and they have all helped me grow as a person and researcher, and aided in guiding me to where I am today. First, I have to thank my advisor, Matthew Reynolds, for guiding me through this entire process. Thank you for all the help over the past few years, from Skype sessions while you were traveling to discussions in lab. I want to especially thank you for helping me set up and run experiments as well as interpret results, and for drilling it into my head that they often take quite some time to complete (which I did learn eventually)! I also want to thank you for supporting me during my time as a PhD student by seeking out funding from various sources. And finally, thank you for understanding what it's like to take 4 graduate level classes, read academic papers, pursue research, write papers, and take exams all in the same semester. I hope that we can stay in touch, and look forward to our future collaborations.

I would also like to thank the rest of the lab, both current and past members, during my time as a PhD student: Chris Tralie, Kris Spaeth, Joshua Ensworth, Daniel Arnitz, Travis Deyle, and Stewart Thomas. I really appreciate all the discussions in lab and couldn't have reached this point without all of you. I want to extend a special thank you to Stewart Thomas, who not only provided and helped design the biotelemetry chip used in a large amount of my experiments, but also provided a great deal of support toward the final months of my time as a PhD student. Stewart,

thank you so much for all the discussions, bits of code, help with experiments, and letting me ask tons of questions while we were holding down the fort in lab.

I also want to thank all of my friends – those from home, Camp Laurelwood, here at Duke, and those on my many soccer and volleyball teams – for all the support thrown my way during my time as a graduate student. I can't thank all of you enough. A very special shout out goes out to Zach Mancher, Sam Kantrow, Josh Barrows, Craig Barrows, Mark Williams, and Amir Norman. You've all been a huge source of support during my long career as a "college" student, and I really appreciate all the phone calls, annual trips, and visits (both planned and unplanned). I wouldn't be who I am without you guys.

A thank you also goes out to my siblings, Jamie Besnoff and Shaina Besnoff. Both of you have always been there for me, and have had to put up with me for quite some time now (you both deserve some sort of medal!). You've both given me huge amounts of strength to succeed in life, and have always shown support for all my endeavors. The future for all of us look bright.

And finally, I owe the biggest thank you to my parents, Shelley Besnoff and Ron Besnoff. Without you, I most certainly wouldn't be the person I am today, and wouldn't be able to call myself a Dr. I can't express enough how much I appreciate all the sacrifices you've made, and continue to make, for me. Thank you for pushing me to always strive to be the best I can be in everything that I do, and for being there for me always. I think the only true way for me to show my appreciation is a gift of a beach house and RV (that will happen someday...).

1

Introduction

1.1 Biosignal Acquisition

The acquisition of biological signals is of interest to biologists, neurologists, and those involved in animal behavioral studies, and is a critical component of emerging health monitoring systems. The ability to transmit this data outside the body is of particular interest for characterizing neural activity for brain-machine interfaces (BMI's) [1], recording brain activity and other physiological signs of freely moving animals [2, 3, 4], for monitoring cardiovascular pressure and blood flow [5], and for improving visual prosthetics [6].

A common method for transmitting biological signals to an external digitization and storage system involves the use of transcutaneous connectors, directly connecting the external system to the region of interest [1]. Transcutaneous connectorized signal acquisition circumvents having to operate with radio frequency (RF) in the environment of highly conductive and lossy biological tissue and fluid, as well as placing the burden of storage, amplification, and digitization on the external system. Transcutaneous wired connections also provide access to directly stimulate tissue in localized regions.

While tethered biosignal acquisition systems with transcutaneous connectors provide a simple method for recording and stimulation, the connection sites are open wounds and are a source of infection. The bulky wire bundles needed for groups of recording and stimulating electrodes are a common source of failure, maintenance, and cost. Moreover, tethered experiments are not behaviorally representative, as the subject is often restricted in terms of motion and interaction.

Given the issues surrounding biosignal acquisition systems utilizing transcutaneous wired connections, a shift to fully implantable wireless systems is an attractive alternative. A wireless implantable system removes the need for transcutaneous connectors and bulky wire bundles, and in the case of passive (battery-free) implantable devices, allows for a maintenance free, chronic recording device. Due to the highly conductive nature of biological tissue [7], inductive coupling using magnetically coupled coils provides a means for wirelessly powering and communicating with implanted devices without causing excess heating of the surrounding tissue. Since the early 1980's, the use of inductive coupling for powering and communicating with implanted devices such as pacemakers and cochlear implants has been extensive [8, 9, 10, 11, 12, 13]. To achieve a high coupling coefficient and quality factor (Q), allowing for a greater direct current (DC) efficiency [14], such systems often operate in the high frequency (HF) band, with a common operating frequency of 13.56 MHz.

Inductively coupled biotelemetry systems operate on the same principle as air-core transformers, and only function when the secondary coil is in the reactive near field of the primary coil. This fact, coupled with the high loss environment in biological tissue, forces this systems to operate over very short distances (typically centimeter distances). Communication is achieved through modulation of the secondary coil's impedance, inducing voltage fluctuations at the primary through the

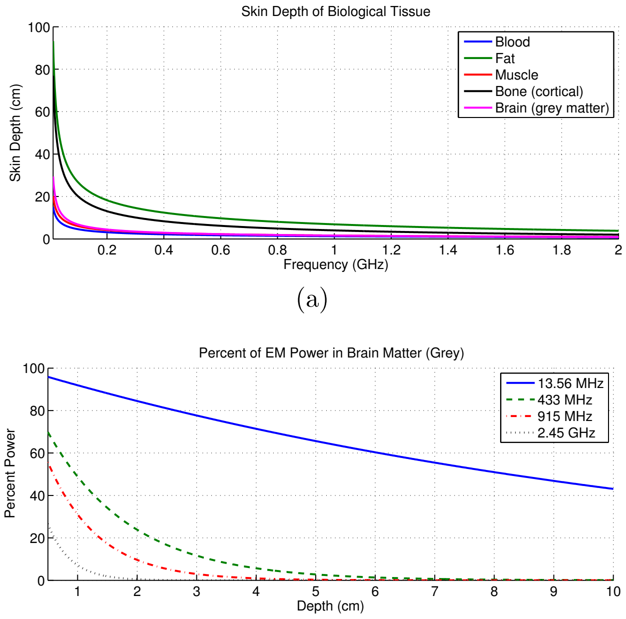

(a)

(b)

FIGURE 1.1: Skin depth of an EM wave in various biological tissues in (a), where the field strength has decayed by $1/e$ or about 37%. In (b), the percent of EM power remaining over distance in brain matter is shown for 13.56 MHz, center of an ISM worldwide band, 433 MHz, center of the ISM band for Region 1, 915 MHz, center of the ISM band for Region 2, and 2.45 GHz, center of a separate worldwide ISM band.

back-coupled magnetic field.

The low operating frequency of typical inductive coupling biotelemetry systems allows for greater signal penetration in biological tissue[1], as signal penetration depth is inversely proportional to frequency. Figure 1.1 shows the penetration depth of an electromagnetic (EM) signal in biological tissue. While lower operating frequencies allow greater signal penetration, they also result in larger coil antenna dimensions, as well as a limited communication bandwidth due to both federal communication commission (FCC) regulations [15] and an inherent tradeoff between range and data transmission speed owing to the Q factor of the coils [16].

The advent of microelectrode arrays capable of recording from hundreds of sites simultaneously and the improvements in analog to digital converter (ADC) tech-

---

[1] See chapter 3 for more detail on signal penetration depth

nology permit biosignal acquisition devices to generate 10's to 100's of megabits per second (Mbps) of data [17, 18]. Additionally, visual prosthetics require large amounts of data to produce high-quality images that allow the user to read text with large fonts [19, 20, 21]. Inductively coupled biotelemetry systems are unable to cope with these large communication bandwidths, and often employ data reduction and compression schemes which aim to reduce the transmitted data rate while preserving critical information. This data reduction results in loss of signal fidelity, and prevents the transmission of raw waveforms.

Designing a wireless implantable biotelemetry system that employs a large communication bandwidth requires an increase in the carrier frequency, which decreases the communication range and increases the circuit complexity and power dissipation. To achieve communication bandwidths of 10's to 100's of Mbps to cope with the raw data generated by modern microelectrode arrays, carrier frequencies in the ultra high frequency (UHF) Industrial, scientific, and medical (ISM) are necessary. This increase in the carrier frequency causes the near field to collapse around the primary coil, and coupled with the highly lossy biological tissue, forces a system in this frequency regime to operate at a fraction of the distance of low frequency inductive coupling systems. Due to these shortcomings in UHF biotelemetry systems, low frequency inductive coupling is often viewed as the only practical method for powering and communicating with implantable devices. This assumption is summarized in the following excerpt from the literature:

> An inductive link between two magnetically coupled coils that constitute a transformer is so far the only viable solution to wirelessly energize high performance implantable microelectronic devices (IMD's) with high power requirements such as neuromuscular stimulators, cochlear implants, and visual prostheses. From *[22]*

This thesis challenges this assumption, and provides a solution toward an end-to-end biotelemetry system capable of supporting deeply implanted devices with high communication bandwidths at low-power budgets by leveraging the transition zone between the near and far field for UHF backscatter modulation and exploiting surface wave propagation to compensate for increased signal loss in tissue.

1.2 Conventional Implantable Devices

Implantable devices have been designed to both monitor specific biosignals and provide stimulation to various areas in clinical and behavioral studies. In order to cope with the highly lossy nature of biological tissues, some systems opt to directly wire the subject to an external system which is used for amplification and digitization of the raw data. Wireless systems have also been developed to avoid the necessity for transcutaneous connectors. These systems favor the use of low operating frequencies for better signal penetration, although this comes at the cost of available bandwidth.

1.2.1 Tethered and Transcutaneous Biosignal Acquisition Systems

With the advent of micromachined electrode arrays, simultaneous recording from many neurons *in vivo* is becoming relatively routine [23, 24]. High-density multielectrode arrays are now available from various commercial and research sources. The weak potentials captured by these high-density multielectrode arrays must be amplified and subsequently digitized. This is often accomplished by an external system through the use of bulky wire bundles and transcutaneous connectors. These wires are a primary source of infection, failure, and manufacturing cost. Additionally, because of possible discomfort and limited range of motion, tethered experiments are generally not behaviorally representative.

An example of a system using this tethered approach has been recently presented in [1], whereby neural signals are recorded from monkeys and used to train a BMI.

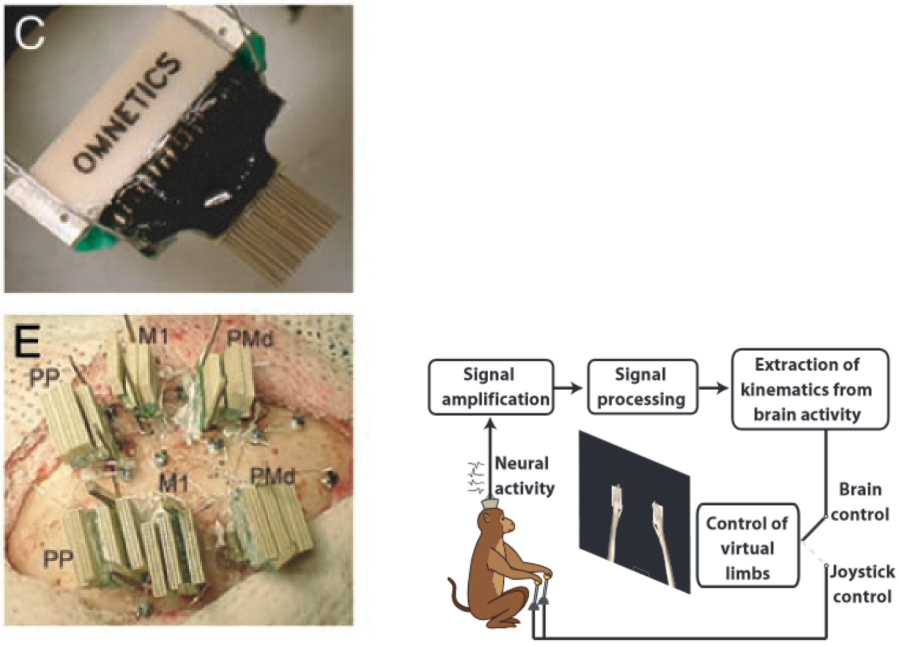

(a) Microwire electrodes and connectors (C) placed in predetermined locations for neural recording (E) (reproduced from [25])

(b) Neural recording system used in [1] with tethered connections

FIGURE 1.2: Example of neural acquisition system using a tethered approach with transcutaneous connectors

Figure 1.2(b) shows the system diagram and Figure 1.2(a) shows a close-up of the transcutaneous connectors. Wire bundles carry the neural signals to an external amplification and digitization system, where a separate wire is needed for each electrode in the high-density array. While this approach is sufficient for the preliminary purposes of characterizing the BMI, a wireless neural recording system employing wireless communication would remove the need for the expensive and inconvenient wires and connectors, which often require maintenance.

1.2.2 Wireless Passive and Semi-passive Devices

Wireless implantable devices remove the need for directly tethering a subject to an external amplification and digitization system by drawing their necessary operating power from an RF interrogation field, using the derived power to drive sensors and

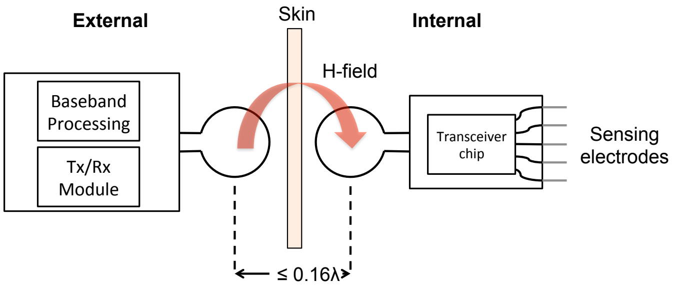

FIGURE 1.3: Diagram of a typical load modulation system used for wireless implantable systems. The antennas are coils that are coupled via the magnetic field, and must operate close together in the reactive near field.

communicate this information back to the transmitting antenna. To achieve better signal penetration into biological tissue, these devices often operate on low-frequency inductive coupling between an external transmitting antenna and the implanted antenna. Typically, communication is achieved through load modulation, whereby the impedance of the internal antenna is altered by switching a load in time with data to be transmitted, causing a voltage fluctuation at the transmitting antenna. This form of coupling lends itself to short range operation, and limited bandwidth.

Inductively coupled load modulation systems are based on transformer coupling between the reader's primary coil and the secondary coil in the implant. This relationship between the two coils is valid if they are within approximately 0.16λ of one another, such that the implant is in the near field of the reader [16]. A typical load modulation system is shown in Figure 1.3, where the antennas are coils in close proximity across a tissue boundary. Most load modulation systems in the literature fall in the HF band.

In typical load modulation systems, the reader and transponder coils are designed to have a high coupling coefficient, and the reader coil is also designed to have a high quality factor (Q) to provide a high efficiency in transferring DC power [14]. Typical operating parameters for a load modulation system are $Q \approx 20$ and $f_0 \approx 13.56$ MHz, resulting in a 3 dB bandwidth of 678 kHz. These system parameters lead to significant attenuation of high frequency data subcarriers.

1.3 Design Challenges

The design of a wireless biotelemetry system capable of low-power, high bandwidth communication with a controlled implant depth incurs many design challenges. Implantable systems are size limited and must be made lightweight so as not to disturb surrounding tissue. This size restriction coupled with the highly conductive dielectric nature of living tissue makes the antenna design, both that of the external and internal unit, critical. Additionally, short guided wavelengths and high loss within living tissue often force implantable systems to operate in a short range regime in the near field, bringing the external antenna close to living tissue. With the external antenna in close proximity to living tissue, the output power of the external system is severely limited by the FCC's maximum RF energy exposure regulations [26]. The system is power limited on the transponder side as well, as it is in direct contact with living tissue and thus cannot heat surrounding tissue to the point of damage. Finally, it is desirable to control implant depth in order to access various tissues, as well as handle multiple implants. A method of routing RF signals within tissue would be beneficial to a wireless implantable system.

The challenges in designing a fully implantable wireless biotelemetry system as shown in Figure 1.4 are expounded upon here.

1.3.1 Size Limitations

In designing a wireless implantable device, the size of the device must be taken into consideration as it will displace living tissue. The implantable device must cause minimal discomfort to the animal, and thus must occupy a small footprint. As the implantable device incorporates the necessary sensors, digitization modules, possible data processing, communication, energy harvesting, and power management,

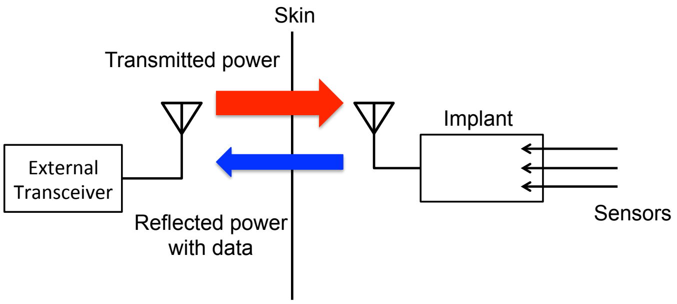

FIGURE 1.4: Proposed system block diagram. The external transceiver creates an RF field, from which the implant draws its operating power. Using this power, it reflects the incoming RF field, modulating it with sensor data.

an integrated circuit (IC) is the logical design choice as it will provide the smallest footprint. The inclusion of a battery on the implantable device, while it can greatly increase communication distance, vastly increases both the size and weight of the device as well as requiring maintenance.

In this work, a maintenance-free design is desired, so a battery-free, passive implantable device is considered. The device also includes the antenna, necessary for both harvesting energy to power the implantable device as well as permit reliable communication with the external system. Shrinking the size of the implantable device results in small antenna designs, and coupled with the highly conductive, lossy dielectric environment, these small antennas tend to be inefficient and low-gain. Antenna design, both that of the external and internal (implantable) antenna becomes critical, as does the choice of frequency.

1.3.2 Power Limitations

Power restrictions arise in this system due to two factors, exposure of living tissue to EM radiation, and direct heating of tissue due to power dissipation.

Limits are placed on the maximum allowable amount of EM radiation into living tissue by the FCC [26]. Essentially, this places strict power restrictions on the external transceiver, as it is responsible for creating the interrogation field for providing both power and a means of communication for the implant device. The figure of merit for EM radiation absorbed by living tissue is the specific absorption rate, or SAR, defined as follows:

$$\mathrm{SAR} = \int_{\text{sample}} \frac{\sigma(\mathbf{r})|\mathbf{E}(\mathbf{r})|^2}{\rho(\mathbf{r})}\, d\mathbf{r} \tag{1.1}$$

where the SAR is defined over a sample of tissue, and measured in W/kg. In the United States, the FCC limits the SAR to a maximum of 1.6 W/kg taken over any 1 g sample of tissue.

As the external antenna is in close proximity to living tissue, Specific absorption rate (SAR) greatly limits transmitted power, affecting the entire system as this energy is needed to both power the implant and provide a means for transmitting sensor data outside of the body.

Additionally, as the implantable device is in direct contact with biological tissue, it must not heat surrounding tissue excessively; only a few degrees Celsius can lead to cell death [27], so the power dissipation on the implantable device must be minimized. This is at odds with the next design challenge, usable bandwidth.

1.3.3 Bandwidth

Shifting the burden of computation to the external system, the implant should be capable of transmitting high-quality, uncompressed data. Data rate increases with increasing signal fidelity, so a system employing a high communication bandwidth is required in order to transmit uncompressed, raw sensor data. This is especially true when it comes to implantable neural devices, as they generate large amounts of data.

One of the common examples of a microelectrode array for neural sensing is the Utah Electrode Array (UEA) [17]. A 10 x 10 UEA digitized at 12 bit precision and sampled at 20 kHz yields an uncompressed data rate of 24 Mbps if on-chip spike sorting (compressive spike detection) is not employed. The implantable device must be capable of handling this large amount of data if the raw sensor data is desired.

1.3.4 Implant Depth and Multiple Implant Sites

Since many implantable devices are forced to operate in the near field, they often suffer from a short communication range, on the order of a few centimeters, typically. EM losses in the near field are greater than those in the far field, and are complex to predict, as even a small change in distance can lead to a vast drop, or increase, in the signal strength. It is thus desirable to have the ability to control the implantation depth of these devices, providing a means for accessing deeper tissues.

Due to the short-range communication of typical implantable systems, multiple external transmitting antennas are often needed to communicate with multiple implants, where a separate antenna is needed for each implant site. In order to avoid the need for a separate antenna for each implant, a method for efficiently routing RF signals throughout tissue is needed, and would remove the burden of excess external transmitters.

1.4 Original Contributions and Document Organization

In this work, it is shown that UHF near field backscatter for implantable devices achieves greater bandwidths than inductively coupled systems at similar power budgets by communicating using scattered fields instead of transformer coupling. A prototype active implantable device presented in this work is able to achieve a bandwidth of 30 Mbps over a 915 MHz link at a communication efficiency of 16.4 pJ/bit, which is similar to the systems shown in Table **??**. A prototype passive device presented in this work operates battery-free, and achieves a transmission rate of 5 Mbps over a 915 MHz link while immersed in saline, and consumes 1.23 mW. This prototype accurately demodulates neural data at an implant depth of 2 cm.

While increasing the carrier frequency permits greater bandwidth, the communication range over the near field link is reduced due to increased signal loss within biological tissue. To overcome this increased signal loss, surface wave propagation is exploited in the form of single-wire RF transmission lines, which permit more efficient routing of RF signals within dielectrics with a high permittivity and conductivity than conventional near field links. A theoretical model for a thin single-wire RF transmission line in dielectrics with large permittivities and conductivities is presented in this work and validated through measurements. A single-wire transmission line of radius 152.4μm exhibits a loss of 1 dB/cm at 915 MHz and extends the implant depth of the presented passive device to 6 cm while staying within SAR limits.

The accomplished original contributions of this work which will be discussed herein are as follows:

- Demonstration of utilizing scattered fields in the radiating near field for active and passive wireless high-bandwidth communication with an implantable device in the UHF ISM band
- Analytic model and supporting measurements for a single-wire transmission line (SWTL) in highly conductive dielectric media
- Characterization of a wirelessly powered biotelemetry device integrated with a SWTL
- Measurement and characterization of an implantable device integrating a SWTL, antenna, and sensor; an end-to-end implantable biotelemetry system

This document is organized as follows:

Chapter 2 presents the theory behind the radiation zones surrounding antennas, the boundary between the near and far fields, and the existence of the transition zone between the near and far fields which supports backscatter modulation. Chapter 3 explains the theory of near field communication in lossy dielectrics such as biological tissue, and how scattering can be used in near field to enhance communication bandwidth over conventional inductive coupling techniques. In Chapter 4, a proof-of-concept experiment is presented using a custom segmented loop antenna and near field backscatter device showing that high-bandwidth scattering is possible in the near field in lossy dielectrics. A previously described [28] passive application specific integrated circuit (ASIC) implementation, complete with a transmitting and receive base station, is also presented with a custom miniaturized octagonal segmented loop antenna design that is capable of sensing, transmitting, and demodulating multichannel biological data at high communication bandwidths while consuming little power. Chapter 5 presents an analytical model and supporting measurements for an efficient single-wire transmission line immersed in a lossy dielectric, for the purpose of providing a more efficient method of routing signal power and data in a lossy environment than near field coupling. In chapter 6, a full end-to-end system integrating the single-wire transmission line and ASIC near field backscatter biotelemetry device is presented, allowing low-power, high-bandwidth biotelemetry with a controlled implant depth. Finally, in chapter 7, a conclusion of this work is presented along with future work pertaining to this system, as well as new avenues that can be explored due to this work.

2

Electromagnetic Propagation From Radiation Sources

A source of electromagnetic radiation, be it a simple current-carrying wire or complex antenna, existing in a dielectric, free space or otherwise, gives rise to both stored and emitted electric and magnetic fields. The interaction of these fields with one another and the environment creates what is known as a *radiation pattern*, which describes the electromagnetic propagation in the vicinity of the radiation source with regard to direction and field strength.

Understanding the electromagnetic propagation characteristics of a radiation source is critical in the design of antennas, shielding, and communication systems. The propagation characteristics of an antenna often guide the operating principles of wireless communication systems. Such is the focus here, as the antenna will drive important aspects of the system's functionality, namely communication range.

It can be shown that the emitted electromagnetic fields from an antenna can be divided into specific zones, each having a distinct set of properties, affecting the communication link differently. The distinction between operating zones is important, as it defines the type of possible communication between a transponder and receiving antenna.

2.1 Existence of Radiation Zones of Antennas

The existence of distinct radiation zones surrounding an antenna can be most clearly seen by observing the radiated fields from simple electric and magnetic antennas. The fields emitted by a simple half-wave electric dipole, such as a whip antenna, and the fields emitted by a magnetic dipole, such as a loop antenna, illustrate the existence of distinct radiation zones.

2.1.1 Fields Emitted By A Half-Wave Electric Dipole Antenna

A simple half-wave electric dipole antenna, such as that shown in Figure 2.1, consists of two separate "arms," each one quarter wavelength in length. The antenna is driven by a source of current at the feed point between the two "arms."

The emitted fields surrounding the half-wave dipole can be derived using Maxwell's equations, with the resulting electric and magnetic fields [29, 30]:

$$E_\theta = j\eta \frac{k^2 I l \sin\theta}{4\pi} \left[\frac{1}{kr} + \frac{-j}{(kr)^2} + \frac{-1}{(kr)^3} \right] e^{-jkr} \tag{2.1}$$

$$H_\phi = j \frac{k^2 I l \sin\theta}{4\pi} \left[\frac{1}{kr} + \frac{-j}{(kr)^2} \right] e^{-jkr} \tag{2.2}$$

$$E_r = \eta \frac{I l k^2 \cos\theta}{2\pi} \left[\frac{1}{(kr)^2} + \frac{-j}{(kr)^3} \right] e^{-jkr} \tag{2.3}$$

where I is the injected current in amps, l is the physical wire length in meters, k is the wavenumber in meters^{-1}, ω is the angular frequency in rads/second, η is the impedance of the medium surrounding the antenna, θ is the angle between the zenith's wire axis and the observation point, and r is the distance from the source to the observation point in meters.

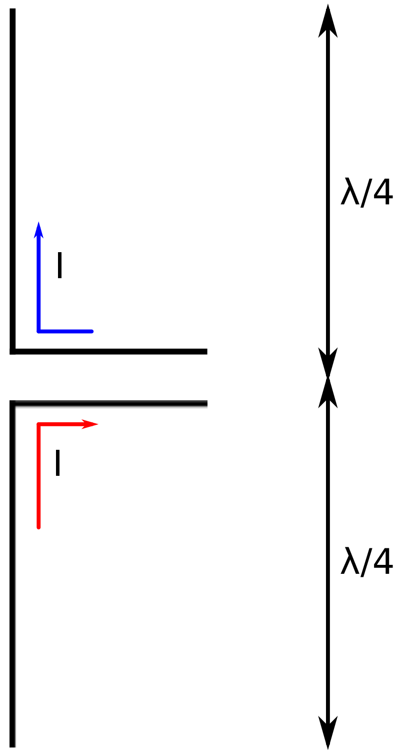

Figure 2.1: Half-wave electric dipole antenna. Each "arm" of the antenna is one quarter wavelength, and it is driven by a current source between the separate "arms," producing a distinct radiation pattern.

In the emitted electric fields of the half-wave dipole antenna, there are terms that decay as $\frac{1}{r}$, $\frac{1}{r^2}$, and $\frac{1}{r^3}$. For very small values of r, or the distance from the antenna, the $\frac{1}{r^3}$ term dominates, and for very large values of r, the $\frac{1}{r}$ term dominates. For values that lie in between these extremes, the $\frac{1}{r^2}$ term dominates. Thus, there are 3 distinct regions, or zones, based on distance from the antenna, where the emitted electric field decays with a different exponent, and behaves differently than in the other zones.

The characteristics of the emitted fields in each of these regions, as well as what it means quantitatively for the distance r to be "small enough" or "large enough" to fall in a specific zone, are explained in subsequent sections.

2.1.2 Fields Emitted By Magnetic Loop Dipole Antenna

The magnetic loop dipole antenna is the dual of the electric dipole antenna. Magnetic dipole antennas in their simplest form can be formed out of a loop of wire, as shown in Figure 2.2. Current is injected into the loop antenna, creating the emitted fields as it travels along the loop.

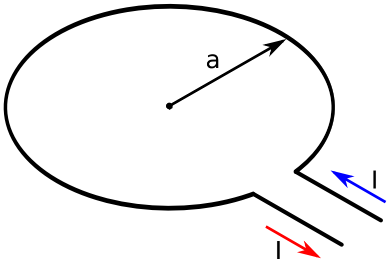

FIGURE 2.2: Magnetic dipole loop antenna of radius a.

The emitted fields from a magnetic loop dipole antenna can similarly be derived from Maxwell's equations, from which the following emitted electric and magnetic fields are obtained:

$$E_\phi = \eta \frac{k^3 a^2 I \sin\theta}{4} \left[\frac{1}{kr} + \frac{-j}{(kr)^2} \right] e^{-jkr} \tag{2.4}$$

$$H_r = j \frac{k^3 a^2 I \cos\theta}{2} \left[\frac{1}{(kr)^2} + \frac{-j}{(kr)^3} \right] e^{-jkr} \tag{2.5}$$

$$H_\theta = -\frac{k^3 a^2 I \sin\theta}{4} \left[\frac{1}{kr} + \frac{-j}{(kr)^2} + \frac{-1}{(kr)^3} \right] e^{-jkr} \tag{2.6}$$

Similar to the electric dipole, the emitted magnetic field of the magnetic dipole in the θ direction contains terms proportional to $\frac{1}{r}$, $\frac{1}{r^2}$, and $\frac{1}{r^3}$. Depending on the value of r, different terms in the emitted fields will dominate. This again demonstrates the existence of distinct regions surrounding an antenna based on distance, where the field components have different rates of decay.

In order to distinguish the characteristics of the emitted fields in each radiation zone, a model for the emitted radiation of an antenna is needed. The details of the radiation zone model are well documented in the literature, and are presented in Appendix A.

2.2 Coupling

The path gain of a signal emitted from an antenna provides insight into the boundaries of the radiation zones. For a co-polarized antenna sensitive to the fields emitted from a transmitter – electric dipole to electric dipole, or magnetic dipole to magnetic dipole – the power at the receive antenna is proportional to the time average value of the incident field squared. Thus, the received power can be computed from equation 2.1 or 2.6 as follows:

$$P_r \sim \left|\vec{E} \text{ or } \vec{H}\right|^2 \sim \frac{1}{(kr)^2} - \frac{1}{(kr)^4} + \frac{1}{(kr)^6} \tag{2.7}$$

The behavior of this path gain is summarized in Figure 2.3. This model is based on the derived field components from an infinitesimal electric dipole, which is considered electrically small. The channel model highlights the fact that there is more power available in the near field than would be predicted by conventional far field models, such as the Friis model. Consequently, there is a higher signal to noise ratio (SNR) in the near field. As the signal decay rate in the near field is rapid, range tends to be finite and quite limited.

Based on the rate of decay shown in the near field channel model, the dominant terms in the field equation can be determined, and consequently, the corresponding radiation zone. Decay rates of 60 dB/decade, corresponding to the reactive near field and the $1/(kr)^3$ terms, and 20 dB/decade, corresponding to the far field and the $1/kr$ terms, are labeled in Figure 2.3. The range where the $1/(kr)^2$ terms are dominant

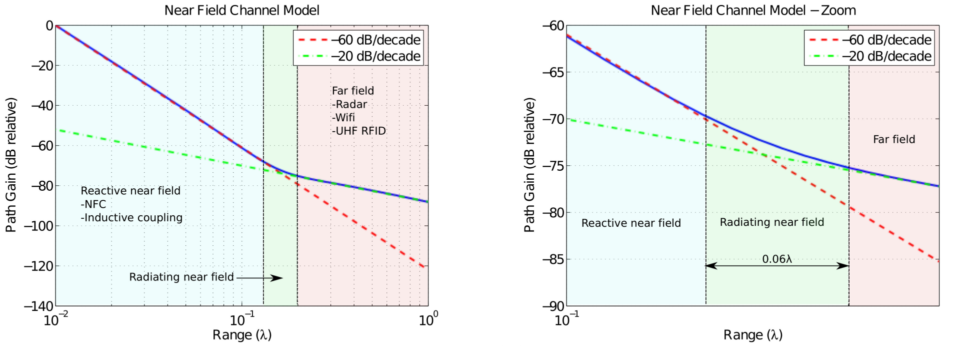

(a) Path gain of signal emitted from electrically small antenna

(b) Channel model zoomed in to show radiating near field

FIGURE 2.3: Near field channel model for an electrically small antenna (Units are dB relative to maximum value)

and the decay rate is 40 dB/decade, the radiating near field, exists as the radiation zone transitions from near field to far field. However, the radiating near field zone is small relative to the wavelength. As shown in Figure 2.3(b), the radiating near field is approximately 0.06λ, which, depending on the wavelength and antenna dimensions, is often negligible. This is in agreement with the two region model often applied to electrically small antennas. Additionally, the boundary of the reactive near field approximates the values given in Table A.1 for electrically small antennas.

For electrically small antennas, the current distribution on the antenna can be considered uniform. However, as the antenna becomes electrically larger, a uniform current distribution is no longer a valid assumption. For electrically large antennas, we use an electric dipole as an example. If the length of the antenna is defined as L and it is oriented along the z-axis and centered at $z = 0$, the current flows in the z direction with an amplitude that can be approximated as [29, 31, 32]:

$$I(z) = \begin{cases} I_0 \sin\left[k\left(\frac{L}{2} - z\right)\right] & 0 \leqslant z \leqslant \frac{L}{2} \\ I_0 \sin\left[k\left(\frac{L}{2} + z\right)\right] & -\frac{L}{2} \leqslant z \leqslant 0 \end{cases} \tag{2.8}$$

Using this current distribution, the field component in equation 2.1 can be modified as follows for a dipole antenna of length L:

$$E_\theta = j\eta \frac{k^2 I_0}{4\pi} \left[\frac{1}{kr} + \frac{-j}{(kr)^2} + \frac{-1}{(kr)^3} \right] \left[\frac{\cos\left(\frac{kL}{2}\cos\theta\right) - \cos\left(\frac{kL}{2}\right)}{\sin\theta} \right] e^{-jkr} \tag{2.9}$$

Based on the non-uniform current distribution in electrically large antennas, the near field channel model in equation 2.7 cannot be used, so the boundaries between the radiation zones take on a different form.

The radiation zone boundaries for electrically large antennas are shown in Table A.1 in Appendix A. The boundary between the reactive and radiating near field is approximately $0.62\sqrt{\frac{D^3}{\lambda}}$, and the boundary between the radiating near field and the far field occurs at approximately $2D^2/\lambda$. Generally, the radiating near field for electrically large antennas cannot be neglected, in contrast to electrically small antennas. For this reason, the three-region model is applied to electrically large antennas, as described in Appendix A. The existence of this zone permits electrically large antennas to communicate through scattered fields in the near field, provided the transponder is in the radiating near field.

In order to communicate through near field scattering, antennas used in this work are electrically large while remaining physically small. The dielectric properties of biological tissue, and of saline which is used as a tissue proxy, shrink the guided wavelength, allowing the antennas used in this work to be on the order to one (guided) wavelength in size.

The boundary of the reactive and radiating near field zones for an electrically large antenna of varying dimension is shown in Figure 2.4.

For an antenna approximately 3 cm in size, the radiating near field exists from 1 - 5 cm, which represents a typically range for the depth of implanted devices. Using this fact, we can take advantage of the radiating near field in implantable devices through appropriate antenna design, which allows the use of scattered fields for

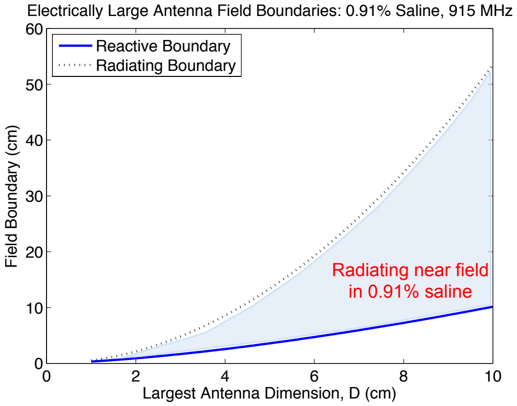

FIGURE 2.4: Radiation zone boundaries for an electrically large antenna at 915 MHz in close proximity to 0.91% saline

communication as opposed to the conventional use of load modulation and evanescent wave modes. By increasing the operating frequency in a biotelemetry system which permits wider communication bandwidths, the guided wavelength in tissue shrinks, which has the effect of causing the transmit antenna to appear electrically larger while also collapsing the radiation zones around the transmit antenna, bringing the radiating near field closer to the antenna and at a usable distance. Bringing the radiating near field closer to the antenna offsets the greater losses incurred in the tissue by increasing the frequency.

A balance can be struck between the transmit antenna size, increased operating frequency, collapsing of radiation zones, and increased signal loss within tissue, such that the antenna appears electrically large when in the proximity of biological tissue and the radiating near field occurs at a distance where enough power is available for operating an implantable device.

3

Near Field Communication in Lossy Dielectrics

The driving factors behind the range, robustness, and efficiency of wireless communication are the operation zone of the communication system, and the signal loss encountered in the communication channel between nodes. A receiver requires sufficient SNR in order to accurately demodulate wirelessly transmitted data, and both the operation zone of the communication system and the communication channel have a direct impact on the available power in the data spectrum. In the case of wirelessly powered systems, there is the additional constraint of requiring sufficient power at the transponder to activate the device for two-way communication.

The operation zone of the communication system, whether it employs near field or far field communication, governs the rate of decay of the communication signal due to spreading, as well as the polarization of the EM fields and their angular dependence. The communication channel, the medium that exists between communication nodes, is responsible for signal decay through absorption of the electromagnetic energy, a result of the reaction of charged particles within the material interacting with the electric and magnetic fields.

3.1 Path Loss

Path loss refers to the decay of an EM signal as it travels through a medium. Thus, the power of a communication signal at a given point in space depends on its path loss. This path loss occurs as a result of the natural spreading of the signal as it travels away from the source, as well as absorption of the electromagnetic energy by the surrounding medium[1]. The path loss can be modeled by the following equation:

$$PL = PL_s\left(D, r, \lambda, \omega, \mu, \epsilon\right) + PL_a\left(r, \omega, \mu, \epsilon\right) \tag{3.1}$$

where PL_s refers to the path loss due to spreading effects, and PL_a refers to the path loss due to absorption of EM energy by the medium.

Spreading of the signal as it travels away from a source is an inherent property of electromagnetic waves and occurs regardless of frequency, wavelength, or surrounding medium. This phenomenon is the basis of path loss models such as the Friis transmission equation [33]. The loss due to spreading effects is entirely dependent on the radiation zone, as explained in 2, and the boundaries between each radiation zone. Thus, this loss factor depends on the dimensions of the transmitting antenna, and the medium properties and frequency which will determine the wavelength. Spreading loss in the reactive near field is on the order of 60 dB/decade, in the radiating near field it is 40 dB/decade, and in the far field, it is 20 dB/decade. Mitigation of the spreading effect can be accomplished through directive antennas.

The other cause of signal loss over distance, absorption of signal energy by the surrounding medium, depends entirely on the material properties surrounding the antennas and communication devices. To understand signal propagation and decay in lossy dielectrics such as biological tissue, material properties and their relation to

---

[1] Constructive and destructive interference due to multipath also affects path loss, but multipath effects are negligible in the near field and thus will be ignored herein

electric and magnetic fields must be discussed.

3.1.1 Material Properties

As all materials are composed of charged particles, they will react to an externally applied EM field through the alignment of charged particles, a reaction to the electric field, and the orbiting and spinning of electrons of the constitutive atoms, a reaction to the magnetic field. These interactions between a material and an EM field can be fully described by the material's dielectric properties. The two quantities which encapsulate the behavior of materials when exposed to EM fields are the permittivity (ϵ), and magnetic permeability (μ). The permittivity describes a material's reaction to electric fields, while the permeability describes interactions with magnetic fields.

The permittivity of a material quantifies its resistance to forming electric fields within itself when exposed to an external electric field. The value of the permittivity describes the amount of electric field that is generated per unit charge in the material. In a material with a high permittivity, more electric field is generated per unit charge due to polarization effects.

The atoms in any given material consist of positive charges in the nucleus, and negative charges in the electrons orbiting the nucleus. When a material is exposed to a static electric field, the centroids of the positive and negative charges are displaced relative to one another, forming a linear electric dipole [30]. This macroscopically introduces an electric polarization to the entire material. When the externally applied fields are no longer static and begin to alternate polarity with a specific frequency, the polarization of the material, and in turn the permittivity, are affected and are functions of the frequency.

The electric flux density, $\vec{D}$, represents how an electric field, $\vec{\mathcal{E}}$, affects the configuration of charged particles in a given medium by the constitutive relation given in equation B.16. A material will not react instantaneously to an applied electric field, the reaction must be causal. This causality results in a phase difference between the electric flux density in the medium and the applied electric field. The phase difference is represented in the permittivity by treating it as a complex function of the angular frequency, ω, as follows[2]:

$$\epsilon\left(\omega\right) = \epsilon'\left(\omega\right) - j\epsilon''\left(\omega\right)^{3} \tag{3.2}$$

The frequency dependence of the permittivity indicates dispersion in the medium. Every material portrays some degree of dispersion (the reaction of internal particles depends on the frequency), though it may be considered negligible in some cases. Since a dependence on frequency can be assumed, for the remainder of this document, the frequency dependence will be omitted in equations containing the permittivity for readability.

Oftentimes, the relative permittivity is used, which is a ratio of the permittivity of a material to that of free space:

$$\epsilon_r = \frac{\epsilon}{\epsilon_0} = \frac{\epsilon' - j\epsilon''}{\epsilon_0} = \epsilon_r' - j\epsilon_r'' \tag{3.3}$$

The real part of the permittivity, ϵ', is related to stored energy within the medium due to the applied electric field. The imaginary part, ϵ'', is related to the electric field dissipation, or loss, within the medium[4].

The dissipation of the electric field within a medium is attributed to bound charge and dipole relaxation phenomenon, which is indistinguishable from the loss due to

---

[2] The permittivity, generally speaking, is a second rank tensor in anisotropic materials, where the permittivity is dependent on direction. In isotropic materials, the permittivity is simplified to a scalar value. All materials considered herein are treated as isotropic, as they display negligible dependence on direction.

[3] The sign convention used here is a result of the time dependence, $e^{j\omega t}$, common in engineering applications.

[4] For a full analysis and derivation of the complex permittivity, see [30], section 2.9.1

free charge conduction from medium's conductivity, σ. Consequently, the complex permittivity and conductivity are related. This relationship is most readily described by the Maxwell-Ampère equation, shown in equation B.2. For a time-harmonic field, the Maxwell-Ampère equation can be simplified as follows:

$$\nabla \times \vec{H} = \vec{J}_i + \vec{J}_c + j\omega\epsilon\vec{E} = \vec{J}_i + \sigma_s\vec{E} + j\omega\left(\epsilon' - j\epsilon''\right)\vec{E} \tag{3.4}$$

$$= \vec{J}_i + \left(\sigma_s + \omega\epsilon''\right)\vec{E} + j\omega\epsilon'\vec{E} = \vec{J}_i + \sigma_e\vec{E} + j\omega\epsilon'\vec{E} \tag{3.5}$$

where:

$$\sigma_e = \text{equivalent conductivity} = \sigma_s + \omega\epsilon'' = \sigma_s + \sigma_a \tag{3.6}$$

$$\sigma_a = \text{alternating field conductivity} = \omega\epsilon'' \tag{3.7}$$

$$\sigma_s = \text{static field conductivity} \tag{3.8}$$

The static conductivity, σ_s, is related to the electron and hole mobility, as well as the electron and hole charge density. The alternating field conductivity, σ_a, is caused by the rotation of the dipoles as they try to align with the applied field while it alternates polarity. The equivalent conductivity, σ_e, is comprised of the sum of the static and alternating conductivities.

Another variable that describes the dissipation of the electric field in a medium is the loss tangent. The loss tangent is related to the conductivity and permittivity through the simplified Maxwell-Ampère equation, shown above in equation 3.4 as follows:

$$\nabla \times \vec{H} = \vec{J}_i + \sigma_e\vec{E} + j\omega\epsilon'\vec{E} \tag{3.9}$$

$$= \vec{J}_i + j\omega\epsilon'\left(1 - j\frac{\sigma_e}{\omega\epsilon'}\right)\vec{E} \tag{3.10}$$

$$= \vec{J}_i + j\omega\epsilon'\left(1 - j\tan\delta_e\right)\vec{E} \tag{3.11}$$

where:

$$\tan\delta_e = \text{effective electric loss tangent} = \frac{\sigma_e}{\omega\epsilon'} = \frac{\sigma_s + \sigma_a}{\omega\epsilon'} = \frac{\sigma_s}{\omega\epsilon'} + \frac{\sigma_a}{\omega\epsilon'} \tag{3.12}$$

$$\tan\delta_e = \frac{\sigma_s}{\omega\epsilon'} + \frac{\epsilon''}{\epsilon'} = \tan\delta_s + \tan\delta_a = \frac{\epsilon''_e}{\epsilon'_e} \tag{3.13}$$

$$\tan\delta_s = \text{static electric loss tangent} = \frac{\sigma_s}{\omega\epsilon'} \tag{3.14}$$

$$\tan\delta_a = \text{alternating electric loss tangent} = \frac{\sigma_a}{\omega\epsilon'} = \frac{\epsilon''}{\epsilon'} \tag{3.15}$$

Similar to the conductivity, the equivalent electric loss tangent, $\tan\delta_e$, is comprised of the sum of the static electric loss tangent, $\tan\delta_s$, and the alternating electric loss tangent, $\tan\delta_a$. The equivalent electric loss tangent directly relates to the dissipation of electric field energy in a medium exposed to an externally applied electric field. As the value of the equivalent loss tangent increases, the amount of dissipated electric energy in the medium increases. The exact relationship between these material property values and the loss of a communication signal is explained in Section 3.1.2.

The quantity that describes a material's reaction to magnetic fields is its magnetic permeability. A material's magnetic permeability quantifies the ability of the material to support the formation of a magnetic field internally. The greater a material's magnetic permeability, the more "magnetized" it becomes in response to an externally applied magnetic field through the spin of the electrons of the material's atoms. This spin is accounted for by considering small electric current-carrying loops. Similar to the alignment of electric dipoles in a material exposed to an electric field, the alignment of magnetic dipoles in a material exposed to a magnetic field must be causal, again resulting in a phase difference between the magnetic flux density, $\vec{B}$, and the magnetic field intensity, $\vec{H}$, through the magnetic permeability as shown in equation B.17. This phase difference is represented by again treating the permeability as a complex function of angular frequency as follows[5]:

$$\mu(\omega) = \mu'(\omega) - j\mu''(\omega) \tag{3.16}$$

Permeability is measured in units of Henries per meter (H/m), and is often expressed in terms of relative permeability, which is the ratio of a material's permeability to that of free space (μ_0)[6]:

$$\mu_r = \frac{\mu}{\mu_0} = \frac{\mu' - j\mu''}{\mu_0} = \mu_r' - j\mu_r'' \tag{3.17}$$

The real part of the magnetic permeability, μ', is related to magnetic stored energy within the medium, while the imaginary part of the permeability, μ'', is related to the dissipation of the magnetic energy within the medium. The permeability of many dielectric materials is nearly identical to that of free space while displaying a negligible imaginary part, and thus negligible magnetic loss. However, ferromagnetic and ferrimagnetic materials – such as iron, cobalt, steel, aluminum, and zinc – exhibit a permeability significantly greater than free space, and are also magnetically lossy. These materials have a non-negligible imaginary part of their permeability, and will dissipate a significant amount of magnetic energy when exposed to an alternating magnetic field[7].

---

[5] In an isotropic medium, permeability is a scalar quantity, but for anisotropic media, it becomes a second rank tensor. All materials considered herein are assumed to be isotropic, thus the scalar form of permeability is used

[6] Similar to the dependence of permittivity on angular frequency (ω), it has been omitted in the subsequent equations containing the permeability for readability. The dependence on angular frequency can be assumed

[7] The materials considered in this document exhibit a negligible imaginary permeability and a real permeability that is nearly identical to that of free space. Thus, each material considered herein is assumed to have $\mu'' \approx 0$, $\mu' \approx \mu_0$, so that $\mu \approx \mu_0$ and $\mu_r \approx 1$

3.1.2 Signal Loss Due to Absorption

As an electromagnetic communication signal propagates in a lossy dielectric medium, a portion of the energy in the signal's electric and/or magnetic fields, depending on the material's properties, is absorbed by the medium and converted to heat, causing the amplitude of the signal to decay.

Based on the wave equation in Appendix C, the propagation constant γ, which encapsulates the phase and attenuation constants of an electromagnetic signal in a lossy dielectric is:

$$\gamma^2 = j\omega\mu\sigma_e - \omega^2\mu\epsilon' = [\alpha + j\beta]^2 \tag{3.18}$$

where α represents the attenuation constant in Np/m, and β is the phase constant in rad/m.

The attenuation of the signal is equivalent to:

$$\alpha = \text{Re}\left[\sqrt{j\omega\mu\sigma_e - \omega^2\mu\epsilon'}\right] = \text{Re}\left[\sqrt{j\omega^2\mu\epsilon'\tan\delta_e - \omega^2\mu\epsilon'}\right] \tag{3.19}$$

The attenuation of an electromagnetic signal in dielectric media of varying material properties is shown in Figure 3.1. As the frequency increases, the signal loss within a given material also increases as the charged particles begin to vibrate more rapidly, converting a portion of the electromagnetic energy into heat. Additionally, the signal loss increases as the relative permittivity and conductivity increase.

3.2 Dielectric Properties of Biological Tissue

The interaction between an EM signal and biological tissue is a critical component in designing a wireless biotelemetry system. For a wirelessly powered implantable device, one of the main requirements is that there must be sufficient power available to the device for operation. In a lossy environment such as biological tissue, this can

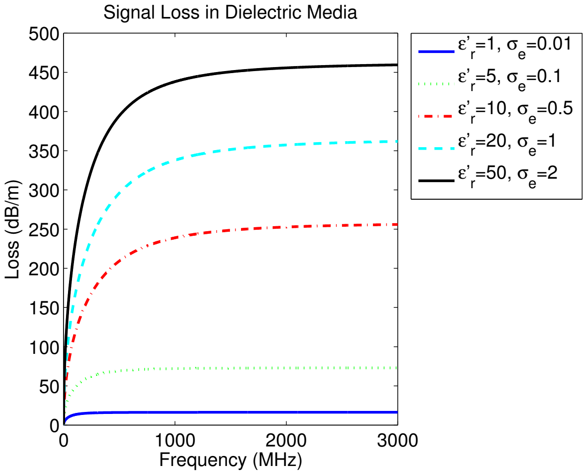

FIGURE 3.1: Loss of an electromagnetic signal in a dielectric medium, where the loss values are given in dB/m

prove difficult due to the increased levels of signal loss due to absorption by tissue, as well as increased loss due to operation in the near field.

3.2.1 Skin Depth

Skin depth is a measure of the penetration of EM signals into dielectrics, and is a useful metric in showing how much signal strength or power is available at a given distance in a lossy dielectric. It is related to the attenuation constant, α, as follows:

$$\delta = \frac{1}{\alpha} \approx \sqrt{\frac{2}{\omega \mu \sigma_e}} \tag{3.20}$$

The skin depth is equivalent to the distance at which the strength of the EM signal, both the electric and magnetic components, has fallen to e^{-1} of the strength at the surface, or approximately 37% of the surface value.

As typical dielectric parameters of biological tissue are $\epsilon'_r \approx 10 - 40$ and $\sigma_e \approx 0.5 - 1.2$ S/m , even for low frequency operation, the skin depth in biological tissue is limited [7]. Figure 3.2.1 shows the skin depth for various biological tissues (tissue data acquired from [34, 35]).

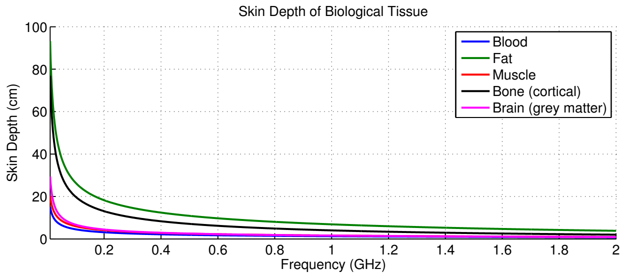

(a)

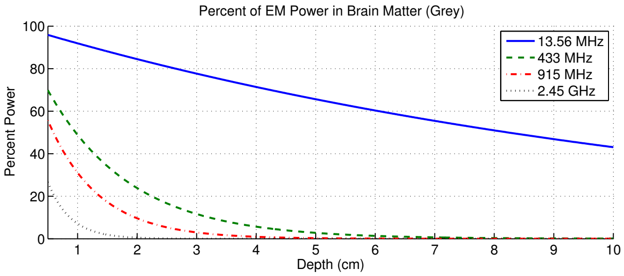

(b)

FIGURE 3.2: Skin depth of an EM wave in various biological tissues in (a). In (b), the percent of EM power remaining over distance in brain matter is shown for 13.56 MHz, center of an ISM worldwide band, 433 MHz, center of the ISM band for Region 1, 915 MHz, center of the ISM band for Region 2, and 2.45 GHz, center of a separate worldwide ISM band.

From Figure 3.2(a), it's clear that as frequency increases, skin depth decreases rapidly, making power transfer and communication with passive implantable devices difficult. Figure 3.2(b) shows the percent of power remaining over distance in brain tissue for various frequencies. Since there is greater signal penetration for lower frequencies, there will also be more power available at a given distance when compared to a signal of greater frequency.

Since frequencies in the HF range offer large signal penetration in tissue, and due to the approximate unity relative permeability of biological tissue, many biotelemetry systems operate using low-frequency magnetic induction. Despite the signal penetration at HF frequencies, due to conversion and mismatch efficiency, as well as inherent near field operation, these systems offer a limited range as well as a limited bandwidth as a consequence of the operating frequency and Q of the coils.

The operating principles of inductive coupling biotelemetry systems are presented here as a point of contrast to the proposed use of backscatter in the radiating near field.

3.3 Inductive Coupling

The use of inductive coupling as a means of powering and communicating with passive implantable devices is a common practice seen in biotelemetry systems. These systems operate on the same principles as transformers, using a primary coil to couple to a secondary coil through the magnetic field, as shown in Figure 3.3. By switching a load at the secondary coil, voltage fluctuations are induced in the primary, establishing a means for communication.

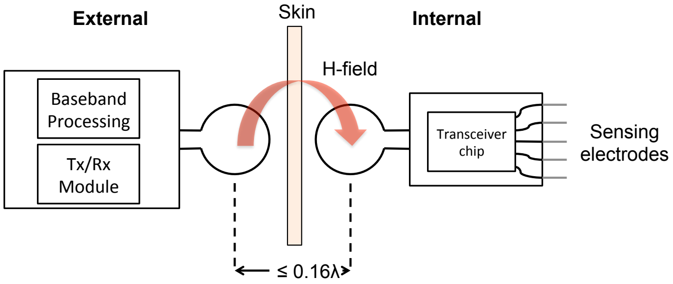

FIGURE 3.3: Diagram of a typical load modulation system used for wireless implantable systems. The antennas are coils that are coupled via the magnetic field, and must operate close together in the reactive near field.

3.3.1 Magnetic Field Strength in Conductor Loops

For inductive coupling, "short cylindrical coils" or conductor loops are used as magnetic antennas generate the alternating magnetic field necessary for powering and communicating with implantable devices. The transmit and receive coils often have multiple turns to enhance the strength of the magnetic field. A typical coil is shown in Figure 3.4.

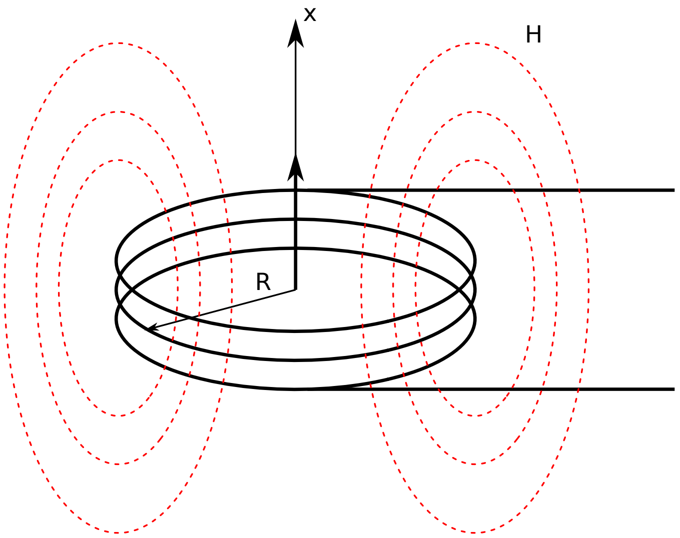

FIGURE 3.4: A typical coil used in inductive coupling systems showing multiple turns and lines of magnetic flux

If the magnetic field strength is measured along the x-axis, as the measurement point moves further away from the center of the antenna coil, the magnetic strength will decay. The rate of decay of the magnetic field strength is governed by the 60 dB/decade rolloff in the near, as well as any losses incurred by absorption of the field energy in the surrounding medium. The following equation can be used to determine the path of field strength along the x-axis of a coil antenna [16]:

$$H = \frac{INR^2}{2\sqrt{(R^2 + x^2)^3}} e^{-\alpha x} \tag{3.21}$$

where N is the number of turns in the coil, I is the current, R is the radius of the coil, x is the distance from the center of the coil (in the x direction), and the $e^{-\alpha x}$ represents loss by absorption in the medium where α is the attenuation constant.

Knowledge of the strength of the magnetic field helps define the range limits of an inductive coupling system.

3.3.2 Loop Inductance

Around conductors of any shape or size, a magnetic field, and consequently a magnetic flux Φ, will be generated. The magnetic flux will be enhanced if the conductor is in the shape of a loop, or coil, common antennas used in inductive coupling as they produce strong magnetic fields.

As stated previously, these coil antennas often employ multiple turns of area A through which the same current, I, flows. Each conductor loop will contribute to the total flux as follows:

$$\Psi = \sum_{N} \Phi_N = N\Phi = N\mu HA \tag{3.22}$$

The inductance, sometimes called self inductance, of a loop is defined as the ratio of the total flux as defined in equation 3.22 arising in an area enclosed by a current to the amount of that current enclosing the flux. The inductance, L, can be written as:

$$L = \frac{\Psi}{I} = \frac{N\Phi}{I} = \frac{N\mu HA}{I} \tag{3.23}$$

Mutual Inductance

If a second conductor coil (area A_2) is located in proximity to the first conductor coil (area A_1) that has a current flowing through it, the second conductor coil will intercept a portion of the total magentic flux generated by loop A_1. These two physically separate circuits are connected through this partial, or coupling, flux. The magnitude of the coupling flux Ψ_{21} is dependent on the geometry of the coils, their angular relationship and position relative to one another, and the magnetic properties of the surrounding medium.

In a similar vein to a coil's inductance, the so-called mutual inductance M_{21} of the second conductor in relation to the first is defined as:

$$M_{21} = \frac{\Psi_{21}(I_1)}{I_1} = \oint_{A_2} \frac{B_2(I_1)}{I_1}\, dA_2 \tag{3.24}$$

Similarly, there is a mutual inductance M_{12}. In this scenario, current I_2 flows through the second conductor coil which induces a coupling flux Ψ_{12} in the first conductor loop. This relationship is described by $M = M_{12} = M_{21}$.

Mutual inductance thus describes the coupling of two circuits through the magnetic field, as shown in Figure 3.5. Mutual inductance is always present between two circuits, though may be considered negligible in some cases.

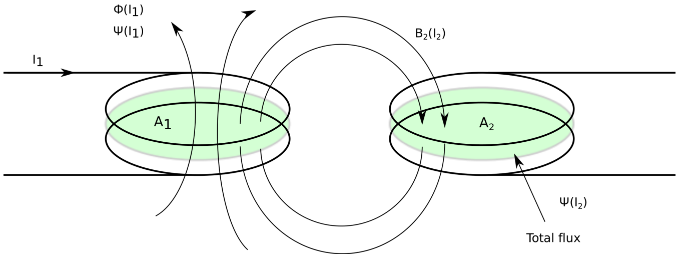

FIGURE 3.5: Mutual inductance as two conductor coils are coupled together through the magnetic field and magnetic flux

Coupling Coefficient

Mutual inductance describes quantitatively the flux coupling of two conductor coils. The coupling coefficient, k_c, on the other hand, is a qualitative description of the coupling of two conductor coils independent of their geometric dimensions. The coupling coefficient is defined as follows:

$$k_c = \frac{M}{\sqrt{L_1 L_2}} \tag{3.25}$$

The coupling coefficient varies between the two extreme cases $0 \leqslant k_c \leqslant 1$.

When $k_c = 0$, it is a representation of full decoupling due either to a large distance between the coils or magnetic shielding. At the opposite extreme, $k_c = 1$ refers to total coupling, where each coil is subjected to the same magnetic flux. A transformer, where both coils are tightly wound around a ferrite core, is an approximate application of total coupling.

A closed form expression for the coupling coefficient is only possible for simple coil geometries. For example, for two parallel conductor loops centered on a single x-axis, the coupling coefficient can be approximated as follows [16]:

$$k_c(x) \approx \frac{r_{\text{Transp}}^2 r_{\text{Reader}}^2}{\sqrt{r_{\text{Transp}} r_{\text{Reader}}}\left(\sqrt{x^2 + r_{\text{Reader}}^2}\right)^3} \tag{3.26}$$

where$x$ is the distance along the x-axis between the coils. This equation only applies when the radii of the coils meet the condition $r_{\text{Transp}} \leqslant r_{\text{Reader}}$. For a transponder coil that is larger than the transmit coil, the value r_{Reader}^2 under the square root in the denominator must be replaced by r_{Transp}^2.

Practical inductive coupling systems often operate with a coupling coefficient as low as 0.01, which is less than 1%.

3.3.3 Induced Voltage

Any change in the magnetic flux generates an electric field strength, a consequence of Faraday's law. In the case of an open conductor loop in the presence of an alternating magnetic field, a current – and consequently, a voltage – builds up in the loop to oppose the change in magnetic flux. The open circuit voltage is proportional to the line integral of the field strength that is generated along the path of the conductor loop.

Faraday's law is stated as:

$$u_i = \oint E_i \cdot ds = -\frac{d\Psi(t)}{dt} \tag{3.27}$$

where u_i is the open loop voltage between the terminals of a given loop. In the case of multiple windings in the loop, $u_i = N \cdot d\Psi/dt$, where N is the amount of turns.

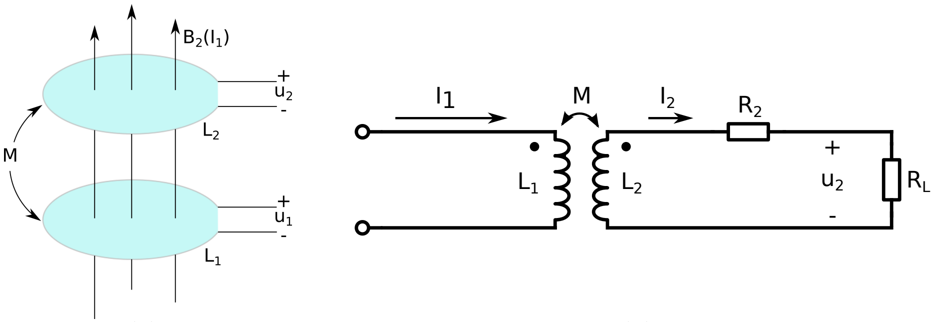

(a) (b)

FIGURE 3.6: Magnetically coupled conductor coils in (a), and equivalent circuit model in (b). R_2 represents the coil resistance, and R_L is a load attached to the coil.

Figure 3.3.3 shows the situation where two coils are magnetically coupled, along with the equivalent circuit model. A time varying current $i_1(t)$ in conductor loop L_1 creates a time varying magnetic flux, $\frac{d\Phi(i_1)}{dt}$, that passes through both L_1 and L_2. Based on Faraday's law, a voltage is induced in both coils, as some fraction of the changing flux passes through them.

The voltage u_2 that is induced in coil L_2 is due to the alternating flux through the mutual inductance, M. The flow of current in coil L_2 creates an additional voltage drop due to the coil's resistance. This current also flows through the load resistance, R_L, such that $i_2 = u_2/R_L$. Finally, the current i_2 in the second conductor coil also generates an additional flux that opposes the flux $\Psi_1(i_1)$ from L_1. This action of the circuit in Figure 3.3.3 can be summarized by the following equation:

$$u_2 = +\frac{d\Psi_2}{dt} = M\frac{di_1}{dt} - L_2\frac{di_2}{dt} - i_2R_2 \tag{3.28}$$

For sinusoidally varying currents, equation 3.28 can be rewritten as:

$$u_2 = j\omega M i_1 - j\omega L_2 i_2 - i_2 R_2 \tag{3.29}$$

Substituting $i_2 = u_2/R_L$ results in:

$$u_2 = \frac{j\omega M i_1}{1 + \frac{j\omega L_2 + R_2}{R_L}} \tag{3.30}$$

In equation 3.30, if $R_L \to \infty$, corresponding to an open loop, the induced voltage is only due to the mutual inductance, $u_2 = j\omega M i_1$. If the conductor coil is shorted, such that $R_L \to 0$, then $u_2 \to 0$.

3.3.4 Resonance

The induced voltage in the secondary conductor coil is used to provide power to the transponder circuitry for passive devices. In practical inductive coupling systems, the efficiency of the equivalent circuit in Figure 3.6(b) is improved by adding a tuning capacitor, C_2, in parallel with the transponder coil to create a resonant circuit whose resonant frequency corresponds with the operating frequency.

The resonant frequency of the conductor coil in parallel with an added capacitance is:

$$f = \frac{1}{2\pi\sqrt{L_2 C_2}} \tag{3.31}$$

Realistically, the capacitance C_2 is composed of a parallel capacitor C_2' and a parasitic capacitance C_p from the coil side, as shown in Figure 3.7. Thus, $C_2 = C_2' + C_p$. To determine the required capacitance to add for resonance, the relationship between C_2, C_2', and C_p is substituted into equation 3.31 to obtain:

$$C_2' = \frac{1}{(2\pi f)^2 L_2} - C_p \tag{3.32}$$

If a voltage $u_{Q2} = u_i$ is induced in the secondary coil, then the voltage u_2 at the load resistor R_L is determined by the following equation:

$$u_2 = \frac{u_{Q2}}{1 + (j\omega L_2 + R_2)\left(\frac{1}{R_L} + j\omega C_2\right)} \tag{3.33}$$

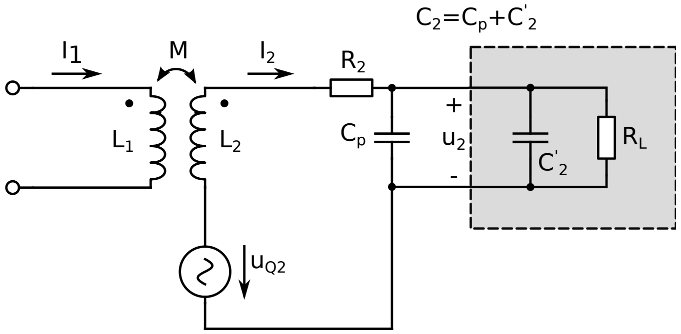

FIGURE 3.7: Circuit model of magnetically coupled coils with tuning capacitor C_2' placed in parallel with secondary loop and parasitic capacitance C_p accounting for stray capacitance due to the remainder of the circuit.

The induced voltage in the coil, $u_{Q2} = u_i$ can be replaced by the factors causing it with the expression $u_{Q2} = u_i = j\omega M i_1 = \omega k_c \sqrt{L_1 L_2} i_1$. Substituting this expression into equation 3.33 results in the following expression for u_2 in terms of the magnetic coupling between the transmitter and transponder coils:

$$u_2 = \frac{j\omega M i_1}{1 + (j\omega L_2 + R_2)\left(\frac{1}{R_L} + j\omega C_2\right)} = \frac{j\omega k_c \sqrt{L_1 L_2} i_1}{1 + (j\omega L_2 + R_2)\left(\frac{1}{R_L} + j\omega C_2\right)} \tag{3.34}$$

where $C_2 = C_p + C_2'$.

The importance of a resonant inductive coupling system is shown by Figure 3.8. At low frequencies, well below the resonant frequency, the induced voltage at the transponder is essentially identical for both resonant and non-resonant systems. However, around the resonant frequency, the induced voltage in the resonant system is about 10 times larger than that of a non-resonant system. Above the resonant frequency, the voltage in the resonant system falls rapidly, reaching values less than that of a non-resonant system. In order to achieve the greatest induced voltage in the transponder and the largest communication range, a resonant system is desired with operation as close to the resonant frequency as possible.

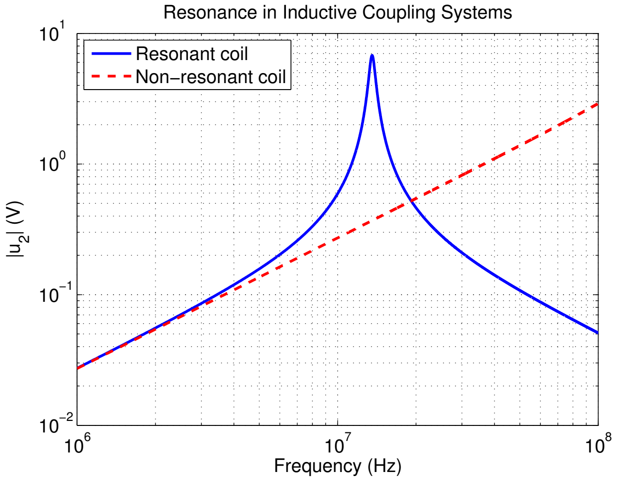

FIGURE 3.8: Induced voltage in a secondary coil for an inductive coupling system for a resonant coil and a non-resonant coil. For each scenario, the following circuit elements were used: $k = 0.05$, $L_1 = 3\,\mu$H, $L_2 = 1\,\mu$H, $R_2 = 1\,\Omega$, $R_L = 2\,\mathrm{k}\Omega$, $i_1 = 5$ mA, $C_p = 0.3$ pF, $f_{\mathrm{res}} = 13.56$ MHz. A clear voltage increase is seen in the resonant system at its resonant frequency.

The choice of circuit elements for the resonant system are critical to its operation, both in terms of component losses and influence on the quality of resonance. This behavior is described by the Q factor of the secondary coil.

Quality Factor in a Resonant Transponder

The Q factor is a measure of both the voltage and current step-up in the secondary coil at the chosen resonant frequency. The Q factor is also related to the damping factor in oscillatory systems. A large Q factor indicates a high-quality resonance, and the resonance will reach a sharp peak at a large value of induced voltage, but will fall off very rapidly above and below the resonant frequency. A small value of the Q indicates a low-quality resonance, with a gradual increase to a small peak value of induced voltage at the resonant frequency, and a slow decrease above this frequency.

For the equivalent circuit in Figure 3.7, the Q factor is defined as:

$$Q = \frac{1}{R_2\sqrt{\frac{C_2}{L_2}} + \frac{1}{R_L}\sqrt{\frac{L_2}{C_2}}} = \frac{1}{\frac{R_2}{\omega L_2} + \frac{\omega L_2}{R_L}} \tag{3.35}$$

The relationship between the circuit elements, Q factor, and induced voltage in the secondary coil is shown in Figure 3.9. When the inductance of the transponder coil, L_2, is changed, and the value of the parallel capacitor C_2 compensates to keep the resonant frequency constant, there is a clear peak in the induced voltage in the secondary coil. The Q factor of the transponder equivalent circuit peaks at the same inductance. Thus, the maximum voltage is dependent on the maximum Q factor.

Due to the relationship between the Q factor and the induced voltage, for every pair of parameters (R_2, R_L), there is an inductance value L_2 for which the induced voltage and Q factor reach a maximum. This relationship is often exploited in inductive coupling systems to maximize the operating range. However, high Q factors lead to increased attenuation of high frequency data subcarriers and can severely limit bandwidth, as shown in Section 3.3.7.

3.3.5 Minimum Interrogation Field Strength

The magnetic field strength, at maximum separation between transmitter and transponder, where the induced voltage u_2 in the transponder coil is just large enough to allow operation is defined as the minimum interrogation field strength, $H_{\min}$.

The induced voltage in the secondary coil as shown in Figure 3.7, L_2, can be determined for the general case using equation 3.27. For a sinusoidal magnetic field

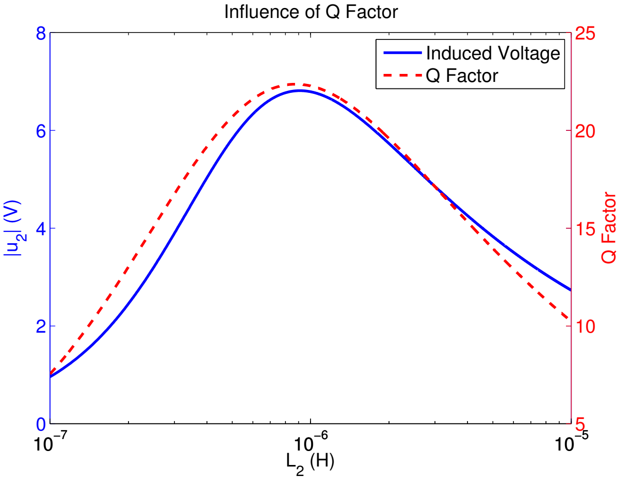

FIGURE 3.9: Relationship between Q factor and voltage for changing inductance of the secondary coil. The value of C_2 is altered to ensure a resonant frequency of 13.56 MHz.

in a homogenous medium of permeability μ, the induced voltage is:

$$u_i = \mu A N \omega H_{\text{eff}} \tag{3.36}$$

where A is the coil area, N is the number of windings, and H_{eft} is the effective field strength of the magnetic field.

Replacing $u_{Q2} = u_i = j\omega M i_1$ from equation 3.34 with equation 3.36 results in the following:

$$u_2 = \frac{j\omega\mu H_{\text{eff}} A N}{1 + (j\omega L_2 + R_2)\left(\frac{1}{R_L} + j\omega C_2\right)} \tag{3.37}$$

Expanding the denominator yields:

$$u_2 = \frac{j\omega\mu H_{\text{eff}} A N}{j\omega\left(\frac{L_2}{R_L} + R_2 C_2\right) + \left(1 - \omega^2 L_2 C_2 + \frac{R_2}{R_L}\right)} \tag{3.38}$$

Finally, equation 3.38 can be solved for H_{eft} to obtain the relationship for the minimum required magnetic field strength, H_{min}, at the transponder:

$$H_{\min} = \frac{u_2\sqrt{\left(\frac{\omega L_2}{R_L} + \omega R_2 C_2\right)^2 + \left(1 - \omega^2 L_2 C_2 + \frac{R_2}{R_L}\right)^2}}{\omega \mu A N} \tag{3.39}$$

Therefore, the minimum required magnetic field strength created by the transmitter and available at the transponder is dependent on the operating frequency, in addition to the permeability of the medium between the coils, μ, the antenna area, A, number of windings, N, the minimum required "turn-on" voltage, u_2, and the input resistance at the transponder, R_2.

When the operating frequency is matched to the resonant frequency of the secondary coil, the required field strength at the secondary coil is at a minimum, again stressing the importance of a resonant secondary coil. Additionally, the minimum required field is inversely proportional to the permeability of the medium, the area of the coil, and the number of windings. While a greater permeability decreases the minimum required magnetic field strength at the secondary coil for operation, the skin depth of the EM signal decreases, potentially forcing the coils to be in closer proximity.

3.3.6 Transformed Transponder Impedance

When the transponder enters the alternating magnetic field of the transmitter L_1, a change in the current i_1 can be detected. The current, i_2, that is generated in the secondary coil, L_2, has an effect on i_1 through the mutual inductance.

To simplify the effect of the mutual inductance on the current in the transmitter coil, an imaginary impedance, the complex transformed transponder impedance Z'_T, is introduced. In the presence of the mutual inductance, the series resonant circuit of the transmitter acts as if there is a discrete component present whose value is equivalent to Z'_T [16]. The transformed transponder impedance is a finite value, and $|Z'_T| > 0$. If the effect of the mutual inductance is removed, which can be accomplished by removing the transponder coil from the interrogation field of the transmitter, then the transformed transponder impedance is shorted, $|Z'_T| = 0$.

The transformed transponder impedance can be calculated by analyzing the transmitter equivalent circuit. Figure 3.10 shows the equivalent circuit of the transmitter, a series resonant circuit. The inclusion of Z'_T represents the influence of the transponder, which is in close proximity to the transmitter, on the current i_1 in the conductor coil.

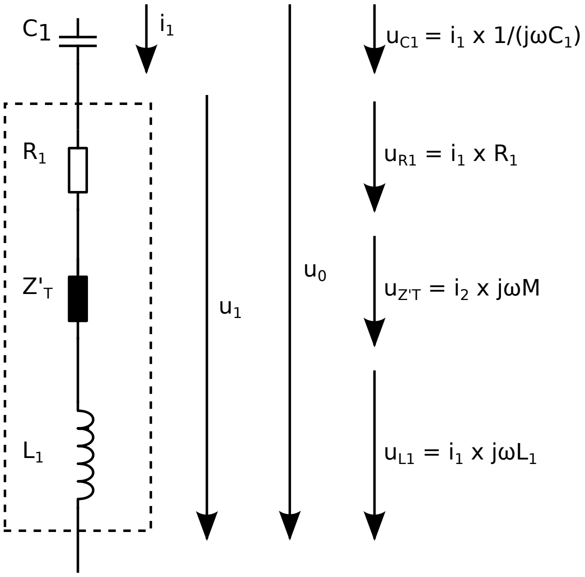

FIGURE 3.10: Equivalent circuit schematic of the transmitter series resonant circuit. The changes in current i_1 in the conductor coil due to the influence of a magnetically coupled transponder is accounted for by impedance Z'_T.

The source voltage of the transmitter, u_0, can be sub-divided into the voltages for each element – u_{C1}, u_{R1}, $u_{Z'T}$, and u_{L1}. As i_1 is present in each circuit element, the source voltage u_0 can be calculated as the sum of the product of each circuit element's impedance and the current i_1 as follows:

$$u_0 = \frac{1}{j\omega C_1} i_1 + j\omega L_1 i_1 + R_1 i_1 - j\omega M i_2 \qquad (3.40)$$

where the transformed impedance Z'_T is represented by $j\omega M i_2$. It is a negative quantity in the above expression due to Lenz's Law.

Since the circuit will be operated at its resonant frequency, the quantities $(j\omega C_1)^{-1}$ and $j\omega L_1$ will cancel out. Thus, equation 3.40 can be simplified to:

$$u_0 = R_1 i_1 - j\omega M i_2 \tag{3.41}$$

An expression for the current in the transponder, i_2, can be determined by using the equivalent circuit model in Figure 3.11. From this diagram, i_2 is computed by:

$$i_2 = \frac{u_{Q2}}{R_2 + j\omega L_2 + Z_2} \tag{3.42}$$

Substituting equation 3.42 into 3.41 results in:

$$u_0 = R_1 i_1 - j\omega M \frac{u_{Q2}}{R_2 + j\omega L_2 + Z_2} = R_1 i_1 - j\omega M \frac{j\omega M i_1}{R_2 + j\omega L_2 + Z_2} \tag{3.43}$$

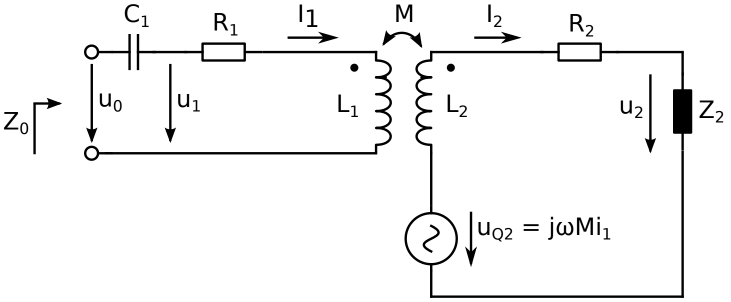

FIGURE 3.11: Equivalent circuit schematic of the transponder in close proximity to a transmitting coil. The impedance Z_2 is comprised of the load resistance R_L and the tuning capacitor, C_2.

Replacing the mutual inductance with the coupling coefficient yields:

$$u_0 = R_1 i_1 + \frac{\omega^2 k_c^2 L_1 L_2}{R_2 + j\omega L_2 + Z_2} i_1 \tag{3.44}$$

Dividing both sides of equation 3.44 by i_1 yields the total impedance in the transmitter, $Z_0 = u_0/i_1$, which is the sum of R_1 and the transformed transponder impedance, Z'_T. Therefore, Z'_T can be computed as:

$$Z'_T = \frac{\omega^2 k_c^2 L_1 L_2}{R_2 + j\omega L_2 + Z_2} \tag{3.45}$$

Expanding the impedance Z_2 to it's constituents R_L and C_2 to incorporate all the components of the transponder yields:

$$Z'_T = \frac{\omega^2 k_c^2 L_1 L_2}{R_2 + j\omega L_2 + \frac{R_L}{1+j\omega R_L C_2}} \tag{3.46}$$

3.3.7 Load Modulation and Communication Bandwidth

The transformed transponder impedance, and thus the current and voltage in the transmitter, depend on the circuit parameters in the transponder. Changes in the circuit elements on the transponder side influence the transformed transponder impedance, which can be detected via the current and voltage at the transmitter antenna terminals.

By varying the circuit parameters of the transponder circuit in time with a data stream, the magnitude and phase of the transformed transponder impedance can be modulated, allowing the data from the transponder to be reconstructed at the transmitter – through the appropriate demodulation technique – establishing a communication link. The two circuit elements that are accessible to change are the load resistance R_L, and the parallel capacitance C_2.

Ohmic Load Modulation

In ohmic load modulation, a parallel resistor, R_{mod}, is switched on and off in time with the data stream [16]. Figure 3.12 shows the equivalent circuit of a transponder equipped with a load modulator.

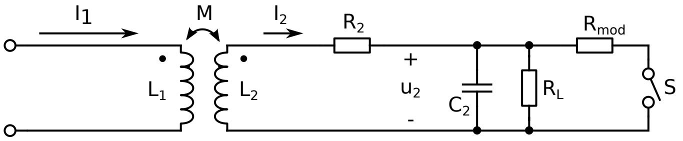

FIGURE 3.12: Equivalent circuit diagram for a transponder employing load modulation. The switch S is operated in time with the data to be downlinked, altering the load of the transponder.

By connecting a resistor, R_{mod}, in parallel with R_L, the total load resistance will decrease, thus reducing the Q factor of the transponder and the transformed transponder impedance. The voltage drop across the transformed transponder impedance will also decrease. This behavior is summarized by Table 3.1.

Table 3.1: Effect of ohmic load modulation on circuit characteristics (The following circuit parameters are used: $f = 13.56\text{MHz}$, $L_1 = 3\,\mu\text{H}$, $L_2 = 1\,\mu\text{H}$, $R_2 = 2\,\Omega$, $R_L = 2\,\text{k}\Omega$, $C_2 = 138$ pF, $R_{\text{mod}} = 1\,\text{k}\Omega$, $k_c = 0.05$, $R_1 = 2\,\Omega$, $i_1 = 20$ mA)

	Effective R_L ($R_L \| R_{\text{mod}}$)	Q	Z_T'	$\lvert u_0 \rvert$
R_{mod} disconnected	$2\,\text{k}\Omega$	15.1	$9.68 - j0.266\,\Omega$	0.234 V
R_{mod} connected	$667\,\text{k}\Omega$	6.61	$4.23 - j0.456\,\Omega$	0.125 V

The two voltage levels shown in the above table can be used to represent binary values in the incoming data stream, encoded in the amplitude of the back coupled signal.

Using the equation for the transformed transponder impedance, a locus of Z_T' can be plotted as shown in Figure 3.13. As R_{mod} increases and is added in parallel with R_L, the transformed transponder impedance decreases, as does the current and voltage at the transmitter side. The phase of Z_T' remains essentially constant during its evolution.

To reconstruct, or demodulate, the transmitted data through the transformed transponder impedance, it would be ideal to have access to the falling voltage across the transformed transponder impedance. However, the transformed transponder

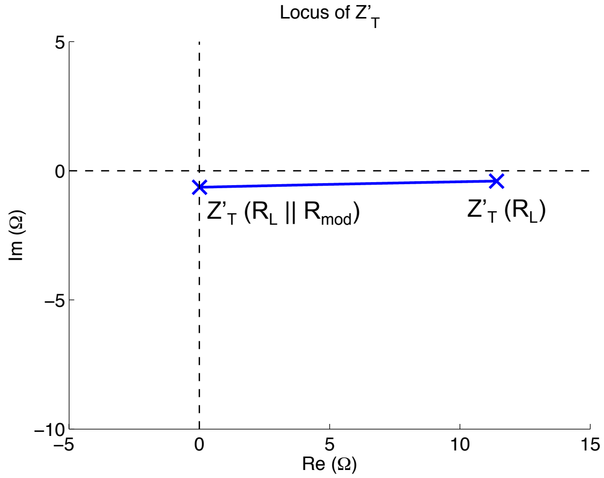

FIGURE 3.13: Locus of transformed transponder impedance for various values of R_{mod}. The resonant frequency is held constant at 13.56 MHz, and $L_1 = 3\,\mu\text{H}$, $L_2 = 1\,\mu\text{H}$, $R_2 = 2\,\Omega$, $R_L = 2\,\text{k}\Omega$, $C_2 = 138$ pF. The value for R_{mod} ranges from 0 - 50 kΩ.

impedance is not accessible to the transmitter circuitry, as the voltage u_{ZT} is induced in the antenna coil, L_1. But, the voltages u_{L1} and u_{R1} are accessible, and can be measured at the antenna's terminals. These voltage fluctuations based on the switching of the modulating resistance at the transponder can be used to determine the transmitted data.

Since the phase of Z'_T remains essentially constant but its magnitude changes, the voltage fluctuations seen at the transmitter will only occur in the amplitude. Thus, ohmic load modulation produces amplitude modulation (AM) at the primary coil, and must be processed accordingly by the receiver. The transmitted data is therefore not available at baseband, but will be seen in the modulation products – data sidebands – of the modulated voltage at the primary coil.

Capacitive Load Modulation

For capacitive load modulation, an additionally capacitor C_{mod} , instead of a resistor, is switched in time with the data stream and connected in parallel with the load resistance R_L. The equivalent circuit for capacitive modulation is shown in Figure

3.14

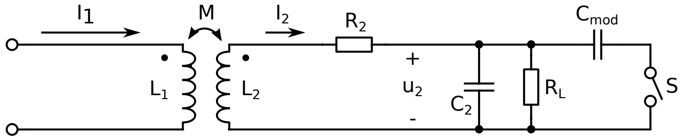

FIGURE 3.14: Equivalent circuit schematic for a transponder employing capacitive load modulation. Switch S is closed in time with the data stream to alter the load impedance by adding C_{mod} in parallel with R_L.

By switching in a capacitor in parallel with R_L, the resonant frequency will change when the switch is closed and the capacitor connected. Changing the resonant frequency, effectively detuning the system, causes the transformed transponder impedance to change in both magnitude and phase. This effect is shown in Figure 3.15.

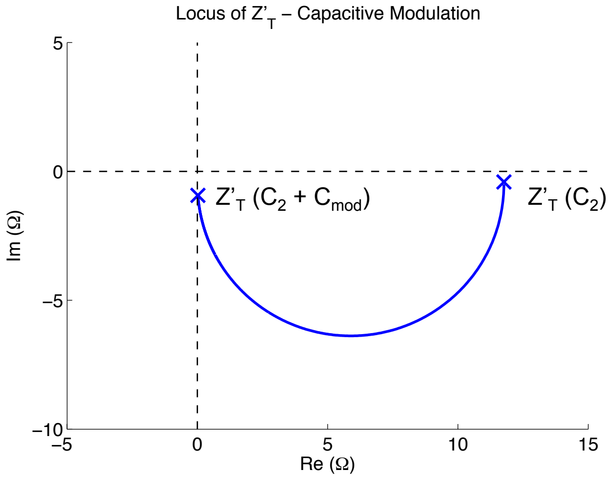

FIGURE 3.15: Locus of transformed transponder impedance Z'_T for capacitive load modulation. The addition of a parallel capacitor affects both the phase and magnitude of Z'_T. The value for C_{mod} ranges from 0.01 - 300 pF.

Since the phase and magnitude of Z'_T is affected by capacitive load modulation at the transponder, the voltage fluctuations received at the transmitting antenna contain both phase and magnitude components. Therefore, capacitive load modulation creates a combination of AM and phase modulation (PM), and should be processed accordingly.

Influence of Q Factor

It is beneficial to both the induced voltage, read range, and the retroactive transformed transponder impedance to maximize the Q factor [16]. In terms of the energy range and induced voltage in the secondary coil, a high Q factor is desired. In order to transmit data from the transponder (or conversely, to the transponder), a minimum bandwidth of the transmission path from the carrier in the transponder to the primary coil will be necessary. However, the available bandwidth of the resonant transponder circuit is inversely proportional to the Q factor.

$$BW = \frac{f_{\text{res}}}{Q} \tag{3.47}$$

With each load modulation operation occurring in the transponder, there is a corresponding amplitude modulation of the current in the transponder coil, i_2. The modulation sidebands of i_2 will be damped to some factor by the bandwidth of the resonant circuitry in the transponder. The bandwidth, BW, is a measure of the usable frequency range around the resonant (carrier) frequency. At the limits of the bandwidth, the modulation sidebands of the current i_2 are attenuated by 3 dB relative to the resonant frequency. This is demonstrated in Figures 3.16(a) and 3.16(b). If the value of the Q factor is too high, the modulation sidebands are damped significantly due to the low bandwidth, and a reduction in read range results.

At the resonant frequency, the value of Z_T' reaches a peak value, which is dependent on the Q factor. Larger Q factors result in a larger peak value of Z_T' at resonance. However, this larger value of Q results in greater attenuation of the modulation sidebands. Figure 3.16(b) demonstrates the significant damping of the modulation sidebands containing the data. Each trace for Z_T' and a given Q factor

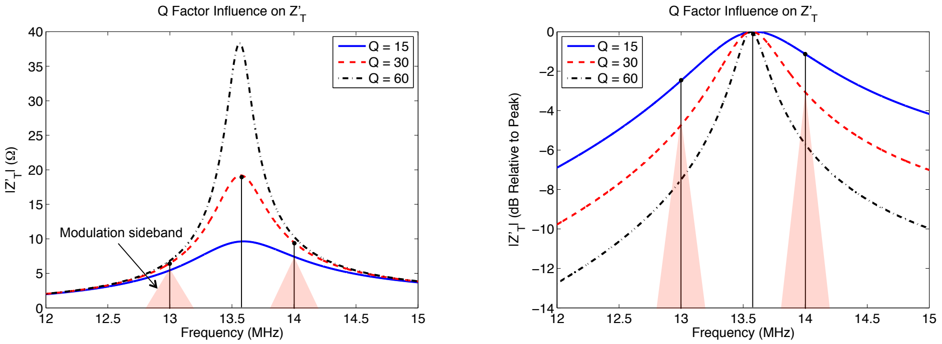

(a) (b)

FIGURE 3.16: The influence of the Q factor on the transformed transponder impedance. The linear magnitude of Z_T' is shown in (a), and the magnitude in dB is shown in (b), where each trace represents a different Q value, and is referenced to its maximum value.

is referenced to its maximum value achieved at resonance. This figure shows the loss, in terms of dB relative to the maximum, of the Z_T' value and as a function of frequency. Moving from a Q value of 15 to a Q value of 30 attenuates the modulation sidebands by an additional 2 dB. This effect would be even more pronounced at a Q value of 60.

The bandwidths for the simulated inductive coupling system for various Q factors can be determined using equation 3.47, resulting in: $BW(Q = 15) = 904$ kHz, $BW(Q = 30) = 452$ kHz, and $BW(Q = 60) = 226$ kHz.

The high Q band limited nature of inductively coupled systems also has a significant effect on the demodulation error rate. The often narrow bandwidth of inductively coupled transponders has the effect of windowing the transmitted data stream in the frequency domain, causing the loss of certain frequency components. This is equivalent to convolution in the time domain of the data stream with a wide signal. This in turn causes the symbols in each bit period to interfere with subsequent symbols, increasing the intersymbol interference (ISI). The amount of ISI increases with the Q factor, as a greater Q factor creates a more band limited circuit and a wider signal that is convolved with the data stream.

The Q factor of the transmitter, which is also often large for DC conversion efficiency, further adds to the ISI of the incoming data stream. The influence of the Q factor from the transmitter and the transponder can be considered part of the channel impulse response. The narrow bandwidth of the channel impulse response causes large amounts of ISI, significantly larger than wideband systems. The great degree of symbol interference in band limited inductively coupled systems with high Q transmitters and transponders increases the demodulation error rate.

The band-limited nature and close operating range of these low-frequency inductively coupled systems is observed in examples from the literature.

3.3.8 Conventional Wireless Implantable Devices

Most prior work in implantable biotelemetry devices employs either inductively coupled load modulation at HF frequencies or traditional on-chip oscillator based transmitters at VHF/UHF frequencies [24]. Implanted systems utilizing HF load modulation (similar to HF RFID) are generally more common than those with on-chip VHF/UHF oscillators.

In this work, we are challenging the conventional design of implantable wireless systems by utilizing modulated backscatter in the near field at UHF frequencies which allows for more compact antenna designs, greater communication bandwidth, and low power dissipation on the implantable device. A comparison of a prototype used for characterizing the near field link and conventional implantable systems in the literature is shown in Table 3.2.

Table 3.2: Performance of selected high data rate *in vivo* neural telemetry communication links

	Inductively Coupled Load Modulation			On-Chip RF Oscillator		This Work
	Mollazadeh 2008 [36]	Mandal 2008 [37]	Hu 2005 [38]	Harrison 2007 [27]	Harrison 2011 [28]	
Operating Frequency	4 MHz	25 MHz	10 MHz	433 MHz	905 MHz	915 MHz
Radio Power Consumption	1.8 mW (Rx)	100 μW (Tx)	0.61 mW (Rx)	1.81 mW	0.27 mW	0.493 mW
Data Rate	32 kbps	2.8-4.0 Mbps	1.12 Mbps	330 kbps	345.6 kbps	30 Mbps
Energy/bit	-	-	-	5.48 nJ/bit	0.781 nJ/bit	16.4 pJ/bit

3.3.9 Inductively Coupled Load Modulation

Inductively coupled load modulation systems are based on transformer coupling between the reader's primary coil and the secondary coil in the implant. This relationship between the two coils is valid if they are within approximately 0.16λ of one another, such that the implant is in the near field of the reader [16]. A typical load modulation system is shown in Figure 3.3, where the antennas are coils in close proximity across a tissue boundary. Most load modulation systems in the literature fall in the HF band.

In typical load modulation systems, the reader and transponder coils are designed to have a high coupling coefficient, and the reader coil is also designed to have a high quality factor (Q) to provide a high efficiency in transferring DC power [14]. Typical operating parameters for a load modulation system are $Q \approx 20$ and $f_0 \approx 13.6$ MHz, which leads to significant attenuation of high frequency data subcarriers. Table 3.2 summarizes the data rate and power consumption in systems designed for *in vivo* applications. Energy per bit is only displayed for systems where radio power consumption was separately reported.

As many load modulation systems are unable to keep up with the large data flow generated by the microelectrode arrays, they are forced to resort to data reduction or compression schemes, which aim to reduce the transmitted data rate while preserving critical information such as spike timing. These data reduction schemes have been extensively investigated in the literature. However, with the loss of neural data comes an inherent loss in signal fidelity.

3.3.10 On-Chip VHF/UHF Transmitters

On-chip RF oscillator-based telemetry systems are able to achieve greater data rates by utilizing carrier frequencies in the 10-500 MHz range, which permit wider signal bandwidths at the cost of much higher power consumption due to RF oscillator bias currents and the possible inclusion of a phase-locked loop to stabilize the RF frequency.

For example, Harrison [27] reports an IC designed to integrate with a microelectrode array that comprises an on-chip RF telemetry system using an on-chip oscillator. This system is able to receive power and commands at 6.5 kbps over a 2.64 MHz inductive link and transmits neural data at 330 kbps using a fully-integrated 433 MHz FSK transmitter. The complete system consumes approximately 13.5 mW of power, with the 433 MHz transmit system consuming 1.81 mW of the total.

Open loop VCO schemes are far more susceptible to process variation as well as changes in temperature and supply voltage. The use of a phase-locked loop, while often necessary for frequency stabilization, can also cause problems in an on-chip RF oscillator based telemetry system. However, this comes at a power consumption penalty since the phase-locked loop, dividers, and reference oscillator usually consume even more power than the RF oscillator. On the other hand, if a phase-locked loop is not included in order to decrease power consumption, the carrier frequency generated by the oscillator is usually very sensitive to temperature changes as well as supply voltage fluctuations. This variation in the carrier frequency will adversely affect the communication link. For example, the on-chip RF oscillator in the aforementioned telemetry system designed by Harrison was found to drift by 400 ppm/°C [27]. Given typical fluctuations in tissue temperature, the carrier frequency might drift by as much as 690 KHz, causing potential problems for the external transceiver as well as possible spectral overlap if multiple implants are present. This tradeoff between power consumption and oscillator robustness presents a significant design challenge when designing telemetry systems utilizing an on-chip RF oscillator.

On-chip VHF/UHF oscillator based systems have potential bandwidth advantages by utilizing higher carrier frequencies, but at the cost of higher power consumption as the oscillators require a DC bias current, which is not necessary in load modulation systems.

These shortcomings in commonly used inductively coupled biotelemetry systems can be addressed by utilizing a greater carrier frequency in the UHF range and employing modulated backscatter in the near field for a low-power, high-bandwidth communication scheme for implantable devices. This technique is addressed in the next chapter.

4

UHF Modulated Backscatter in the Radiating Near Field

This section describes an approach to the first 3 design challenges mentioned in the Introduction section by proposing a system that utilizes modulated backscatter in the near field at UHF frequencies. Conventional implantable systems are presented as a point of comparison, followed by experimental measurements and results of the near field link and a prototype device employing backscatter in the near field.

The critical distinction between the conventional approach using inductively coupled systems with load modulation and the presented approach of using near field UHF backscatter is that load modulation in high Q systems is inherently band limited, whereas near field backscatter is wideband and not band limited. The presented approach using near field backscatter does not suffer the disadvantages of band limited systems.

4.1 Near Field UHF Backscatter Biotelemetry

For implantable devices, near field modulated backscatter is a promising approach to high bandwidth communication. In contrast to far field electromagnetic communication (where $d >> \lambda$) in which energy is propagated by a combination of electric and magnetic field components, evanescent modes dominate in the near field where $d << \lambda$. Most implantable devices, particularly in small animals, have an implant depth of less than 10 cm. At typical implant depths, utilizing UHF carrier frequencies causes the system to operate where evanescent modes dominate. In the near field regime, signals can be coupled via the magnetic component of the evanescent mode. Because animal tissues have low magnetic permeability, the magnetic field is relatively unaffected by tissue proximity, and even at high carrier frequencies the losses in tissue are manageable.

Figure 4.1 shows the implementation of a UHF near field modulated backscatter implantable system. The external transceiver creates an interrogation field, a CW signal, which the implant, beneath skin (and possibly other tissue, fat, and bone), uses to derive its operating power. Using this harvested energy, the implant will receive sensor data and perform the necessary amplification and digitization. Using a backscatter modulator, such as the binary modulator shown in Figure 4.1, the implant will modulate its antenna impedance by switching a load in time with the data to be uplinked, in turn causing the power reflected back to external transceiver to be modulated with the sensor data. This will appear as data sidebands in the spectrum of the received signal.

The near field UHF modulated backscatter modality is distinct from near field inductive communication techniques at low carrier frequencies such as NFC. These systems, where $f < 30$ MHz, are load modulation schemes. Load modulation systems are based on transformer coupling between the reader's primary coil and the secondary coil in the implant. Thus, communication is not achieved through scattered fields but rather via a switched load at the transponder antenna, inducing a voltage change at the external system [16]. Given the low carrier frequencies of inductive load modulation systems, bandwidth is severely limited, as shown in Table 3.2.

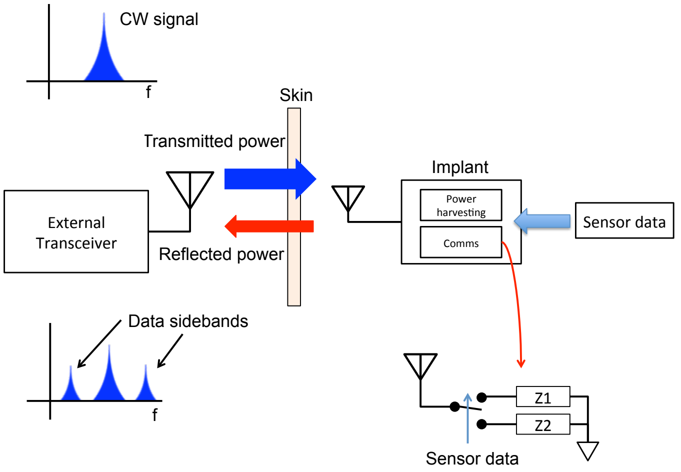

FIGURE 4.1: Implementation of a near field UHF modulated backscatter implant device. The device draws its power from the transmitted signal, and uses this power to switch a load connected to the internal antenna in time with data, modulating the reflected power with sensor data.

The higher UHF carrier frequencies permit correspondingly higher modulation rates, allowing the potential transmission of uncompressed, raw data. In both cases, an external reader system acts as a transceiver, creating the RF interrogation field and simultaneously demodulating the reflected power to receive data from the transponder. Additionally, tissue has a high dielectric constant, $\epsilon_r \approx 10 - 40$ [7], so high frequency signals propagating within tissue have short guided wavelengths (mm to cm) and the high tissue conductivity ($\sigma \approx 1.1$ S/m, [7]) results in increased loss over free space, and thus antenna design is more critical for UHF than HF.

Operating in the UHF near field is also beneficial as the incident field can also be focused on the specific area surrounding the implant, reducing extraneous absorption of electromagnetic radiation in adjacent tissue. UHF modulated backscatter naturally lends itself to low on-chip power consumption as the clock frequency required on the implant is proportional to the modulation rate as opposed to the RF carrier frequency.

4.2 External Antenna Design Considerations

The external antenna is critical to UHF near field telemetry performance. In contrast to dipole or patch antennas designed for their far-field gain and radiation pattern, different techniques must be used in the UHF near field. The segmented loop design generally exhibits better broadband characteristics in proximity to high ϵ_r materials compared to dipoles or patches [39]. We have designed a near field segmented loop antenna, as they generate strong uniform magnetic fields and can be better optimized for SAR performance, optimized for operation in the 902-928 MHz US Part 15 ISM band.

The segmented loop measures 17.5 cm x 18 cm, and is comprised of 19 distinct segments, each 2 mm wide. There is an inner "ring" and an outer "ring" of segments, separated by 1 mm. There are 10 inner segments measuring 64 mm each, except at the feed point. The outer "ring" consists of 9 segments, each measuring 62.5 mm.

This design was characterized both in free space and in close proximity to a saline proxy for tissue. The proxy system consists of a polyethylene tank containing 6l of 0.91% mass / volume saline. A model of the antenna and tank system shown in Figures 4.2(a) and 4.2(b) was constructed and simulated using the finite difference time domain (FDTD) solver in CST Microwave Studio 2010.

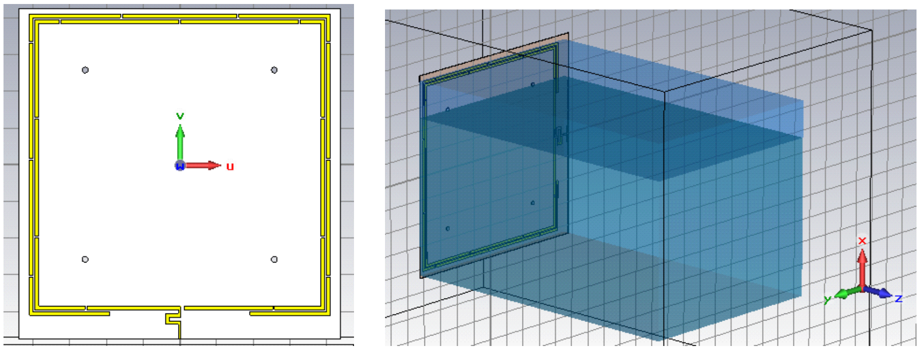

(a) Antenna in free space (b) Antenna with saline tissue proxy

FIGURE 4.2: Near field antenna model for simulation

Figure 4.3(a) shows the return loss of the segmented loop antenna in free space in measurement and in simulation. The antenna was characterized over a 200 MHz range, from 800 MHz to 1 GHz, and is shown to match well to free space over this range, displaying broadband performance as expected. Return loss is better than 12 dB across the 902-928 MHz band. The experimental data matches well with the simulation. The resonant frequency difference between measurement and simulation is explained by the uncontrolled dielectric constant of the FR-4 printed circuit board, as a slight difference in ϵ_r accounts for the observed 3% difference between simulation and measurement.

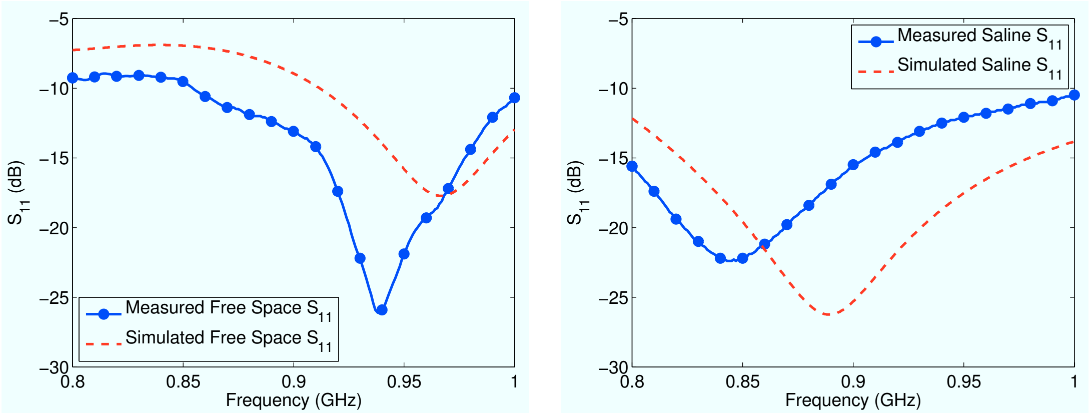

(a) Free space (b) Saline

FIGURE 4.3: Measured vs. simulated return loss of segmented loop in free space and saline

Figure 4.3(b) shows the measured and simulated return loss of the segmented loop antenna when placed directly in contact with the saline proxy system, which is a lossy dielectric fluid. The antenna's matching has shifted when compared to free space, so the antenna now resonates at a lower frequency, quite close to 850 MHz. The antenna exhibits a return loss of better than 13 dB across the 902-928 MHz band. As with the free space simulation, the discrepancies between the measured and simulated results in front of the saline tank can be explained by the uncontrolled dielectric constant of the antenna's substrate, as well as added discrepancies from the properties of the saline model in CST. The dielectric constant of the saline is uncontrolled, and its dielectric and thermal properties are temperature dependent [40].

4.3 Characterizing The Near Field Link

In order to prove that near field UHF modulated backscatter is a viable option for communication for wireless implantable devices, the channel must be characterized. The near field channel was characterized in terms of measured signal loss, to determine if there is enough signal strength available for powering of the implant and communication at typical implant depths. The aforementioned segmented loop antenna was used as the external transceiver antenna, and a small loop antenna, suitable for coupling to the magnetic near field, was used as the internal antenna.

4.3.1 One-Way Path Loss Measurements

Since a wireless neural recording device operates in the UHF near field with a segmented loop transmitting antenna, a small loop antenna has been selected for the transponder antenna. A loop of 9.67 mm diameter, constructed from 22 AWG wire (0.644 mm diameter), was used for the path loss test. This diameter is of reasonable size to fit inside the skull of a mouse we plan to use in future experiments. A test rig was constructed as shown in Figure 4.4, which keeps the loop antenna on boresight and at a consistent depth within the tank. Ferrite absorbers were used to suppress currents on the shield of the RF cables. The path loss between the segmented loop antenna and the small loop antenna was measured using a network analyzer both in the saline tank and in free space. Figures 4.5(b) and 4.5(a) show the results of this experiment.

Since the small loop antenna was not matched to 50Ω, there was inherent mismatch loss when connecting it directly to the network analyzer. Moreover, since the

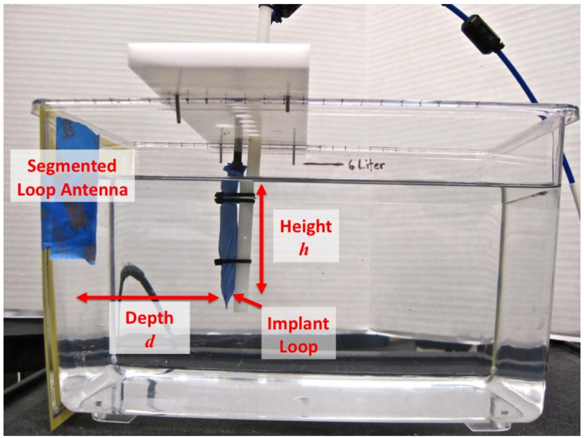

FIGURE 4.4: Near-field UHF backscatter apparatus showing saline proxy system

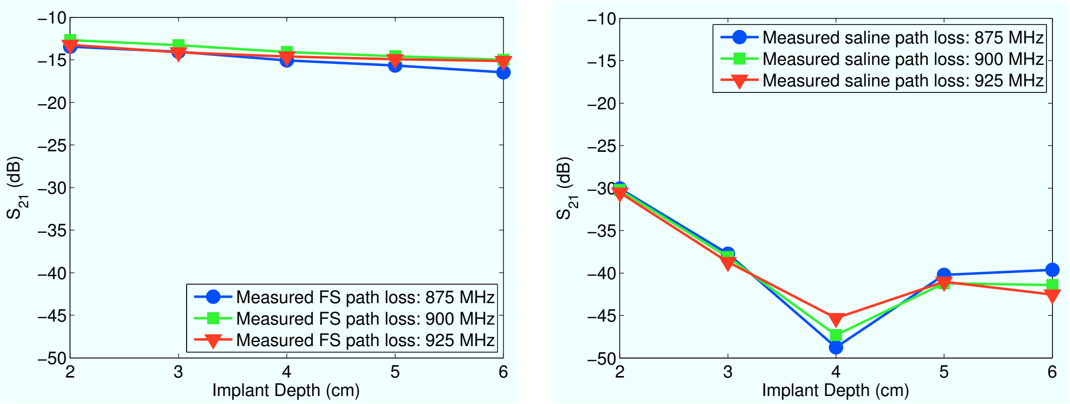

(a) Free space

(b) Saline

FIGURE 4.5: One-way measured path loss after mismatch correction

small loop has a different impedance in free space and in saline, there is a different mismatch loss associated with each medium. To obtain accurate path loss measurements, the mismatch loss in each case was corrected by measuring the impedance of the small loop in both free space and saline, and then determining the reflection coefficient and corresponding mismatch loss in each scenario. The impedance of the implant loop in free space and saline, as well as the mismatch loss in a 50Ω system, is shown in Table 4.1.

The implant loop is inductive in both media, but with significantly different reactance. In saline, the inductive reactance of the implant loop is approximately 2 nH, but in free space, it ranges from approximately 79 nH to 110 nH for the frequencies tested. The real part of the implant loop's impedance is also significantly different between the two media. There is very little mismatch loss for the implant loop in the saline, approximately 0.27 dB, compared to the significantly larger mismatch loss of approximately 17 dB in free space.

Table 4.1: Implant loop impedance and corresponding mismatch loss

(a) Free space

Frequency	Impedance (R+jX) (Ω)	Mismatch Loss
875 MHz	17.601 + j436.17	17.43 dB
900 MHz	21.674 + j500.82	17.71 dB
925 MHz	37.615 + j641.98	17.47 dB

(b) Saline

Frequency	Impedance (R+jX) (Ω)	Mismatch Loss
875 MHz	78.852 + j12.151	0.2618 dB
900 MHz	79.875 + j12.766	0.2779 dB
925 MHz	79.554 + j11.654	0.2671 dB

The results of the path loss test show that the small loop experiences less path loss in free space when compared to saline at all distances tested. This is not surprising as saline has a much higher relative permittivity, $\epsilon_r \approx 80$, than air, and also has a larger loss tangent at the tested frequencies, and is thus a more lossy dielectric fluid [40]. There is not a significant difference in path loss between the three frequencies tested, both in saline and in free space. The path loss within the saline seems to increase around a distance of 4 cm, possibly due to coupled modes in the size of the tank used.

Assuming a forward link-limited situation, as in most RFID systems, a receiver that is sensitive down to about -80 dBm could effectively communicate with an implantable device employing backscatter in the near field at UHF frequencies according to the path loss measurements shown here. Now that it has been established based on one-way path loss measurements that communication with a wireless implantable device is possible using near field UHF modulated backscatter, the communication aspects of the channel can be characterized.

4.4 Near Field UHF Modulated Backscatter Characterization

To characterize the MBS channel itself, a prototype external transceiver was constructed and connected to the segmented loop antenna. This system creates an RF interrogation field at a transmitter output power of +24.92 dBm, and is shown in Figure 4.6. The transmit path consists of a signal generator (Agilent N5181A), amplifier (Mini-Circuits ZRL-3500+), and a 15 dB coupler (Mini-Circuits ZFDC-15-10-S) to separate the transmit and receive paths. The signal generator drives the antenna at the appropriate frequency, and the amplifier is used to bolster the interrogation field. The received signal is separated from the transmit path via the 15 dB coupler, and a spectrum analyzer (Agilent E4404B) was used to view the frequency spectrum of the backscatter.

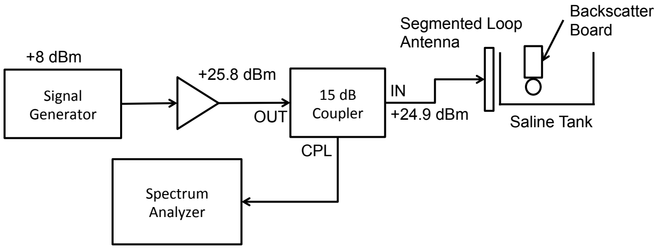

FIGURE 4.6: Experimental setup to measure backscatter

4.4.1 Prototype Backscatter Board

In order to examine backscatter communication between the neural transponder and the external transceiver, a prototype backscatter modulator was fabricated as shown in Figure 4.7. A schematic can be seen in Figure 4.8. The 9.67 mm diameter loop antenna was attached to the backscatter board using an SMA connector, and an Analog Devices ADG904 CMOS RF switch was set to switch the antenna's load between open and short, thus modulating the reflected power. The board was powered with a 3 V coin cell, and could be set to switch at a rate of 7.5 MHz, 15 MHz, or 30 MHz depending on which 0Ω resistor was connected to the RF switch. An RF power harvester is not included in this design but is a subject of future work.

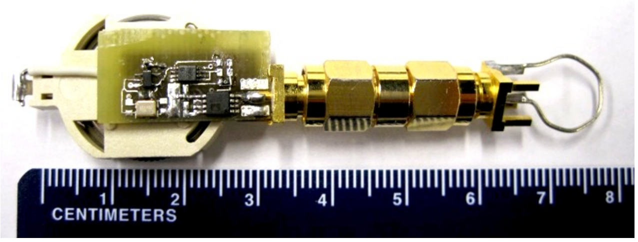

FIGURE 4.7: Modulated backscatter test board with 9.67 mm implant loop antenna attached

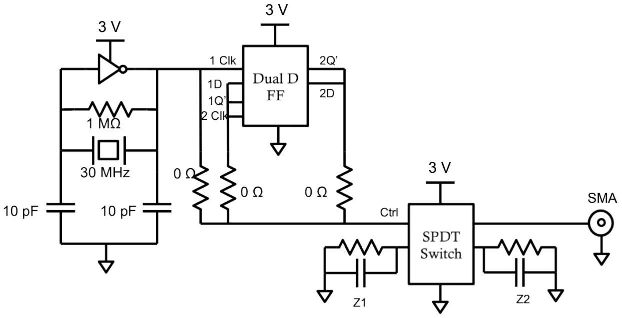

FIGURE 4.8: Schematic of the modulated backscatter test board

With the 9.67 mm diameter loop connected to the backscatter board, the power of the backscattered signal was obtained at 875 MHz, 900 MHz, and 925 MHz. The distance between the backscatter board and the segmented loop antenna was varied to observe the magnitude of the backscattered signal. This was performed for backscatter rates of 7.5 MHz, 15 MHz, and 30 MHz. The results of these measurements can be seen in Figures 4.9(a)-4.9(c).

As expected, generally the backscattered signal decreases in strength as the distance from the segmented loop is increased. At each backscatter rate, the backscatter signal was visible up to 6 cm, but beyond this distance, it became buried in the analyzer noise. It is expected that the backscattered signal will be weaker in the saline

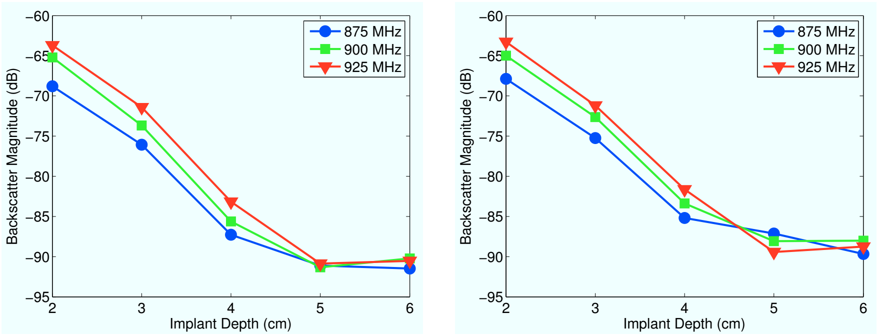

(a) Backscatter at 7.5 MHz (b) Backscatter at 15 MHz

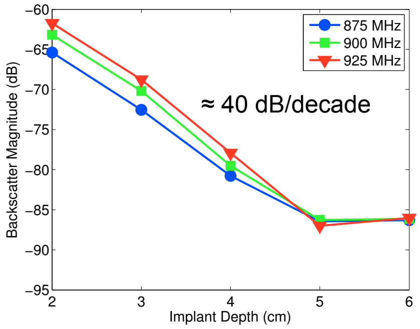

(c) Backscatter at 30 MHz

FIGURE 4.9: Backscatter magnitude (dB relative to Tx power) versus implant depth in the saline proxy for various carrier frequencies

and decay rapidly due to the large relative permittivity of the saline, $\epsilon_r \approx 80$ [40]. Additionally, the high relative permittivity of the saline causes the guided wavelength within the saline to be quite small, contributing to the rapid decay of the backscattered signal in the saline. Due to the small guided wavelengths within the saline, approximately 3.7 cm at 915 MHz, the entire system is operating in the near field. In the operating region from approximately 2 - 5 cm, the decay rate of the backscatter magnitude is approximately 40 dB/decade as labeled on Figure 4.9(c). This indicates that the transponder is operating in the radiating near field, the desired region for UHF backscatter, and verifies that communication is being performed through scattered fields and not through inductive coupling.

The carrier frequency utilized appears to have a slight effect on the backscattered signal. Generally, for the carrier frequencies tested, the greater the carrier frequency, the greater the received signal strength of the backscatter. The signal strength of the received backscatter also matches well with the one-way path loss measurements shown in Figure 4.5(b), although the increase seen in the path loss at 4 cm is not readily visible. The rate of decay of the signal strength over distance appears to be similar across each backscatter rate tested.

Variation in backscatter power with backscatter rate is likely due to the switching times of the RF switch. The on switching time for the Analog Devices ADG904 switch is approximately 10 ns, and the off switching time is about 16 ns [41]. This means that the maximum cycle time is approximately 38.5 MHz. Our 30 MHz backscatter rate is close to the switching time limits for this particular switch.

4.4.2 Power Consumption

Since the main communication element in this backscatter system is a CMOS RF switch, this was the only component considered in measuring the power consumption of the backscatter board.

The RF switch was isolated from the other components, and the current draw at different supply voltages was measured for each backscatter rate. The results can be seen in Table 4.2.

It's clear that as the backscatter rate is increased, the current draw of the RF switch also increases, so the power dissipated also increases with switching rate. However, the energy per bit for both the 7.5 MHz and 15 MHz switching rates are not significantly different. At a 30 MHz switching rate, the energy per bit decreases from 27.0 pJ/bit to 16.4 pJ/bit. The on switching time for the switch is about 10 ns, and the off switching time is about 16 ns [41]. At 30 MHz, or $\tau = 33$ ns, this is pushing the switch to its limits.

For the highest switching rate tested, 30 MHz, and for the supply voltage used on the backscatter board, about 3 V, the RF switch consumed about 164 μA, and

Table 4.2: Power consumption and energy performance

Backscatter Frequency	Supply Voltage (V)	Current (μA)	Power (mW)	Energy/bit (pJ/bit)
7.5 MHz	3.01	67.8	0.204	27.2
15 MHz	3.01	135	0.406	27.0
30 MHz	3.01	164	0.493	16.4

thus uses 16.4 pJ/bit. This power consumption and energy per bit is competitive with those systems shown in Table 3.2. This system thus lends itself well for a communication scheme for an implant that is in direct contact with biological tissue.

4.5 ASIC Implementation Of UHF Near Field Modulated Backscatter

The previous section characterized the one-way near field communication channel and showed that in a forward link-limited situation, communication is possible. The prototype board constructed derived its power not from the interrogation field generated by the external antenna, but from a battery in order to isolate the communication channel only. In this section, an existing ASIC [3] employing power harvesting and the ability to transmit 16 simultaneous channels of sensor data is used to characterize the near field backscatter link for a passive implanted device. In addition, the external antenna design has been reconsidered in favor of a more compact and efficient design.

4.5.1 Redesign Of External Antenna

The design and functionality of the external antenna is crucial to the performance of UHF near field telemetry. Unlike antennas designed for their far-field gain and radiation pattern, such as patch antennas and dipoles, different design approaches must be used in the near field at UHF frequencies, especially for a system that must perform well in the vicinity of highly lossy and conductive materials, as they tend to adversely affect antenna performance.

Segmented loop antennas are a promising avenue for use in near field biotelemetry.

These types of antennas generally consist of multiple capacitively coupled segments, occasionally using lumped capacitors between the segments. The capacitively coupled segments provide a small phase delay, and ensure that the current is in phase around the loop. The result is a uniform magnetic field distribution, ideal for inductive coupling in the near field. Additionally, the segmented loop design generally displays better broadband performance in the vicinity of media with a large ϵ_r when compared to patch antennas and dipoles [39].

When designing transmitting antennas that are to operate in close proximity to the human body, absorption of electromagnetic radiation becomes an area of concern. The figure of merit when describing bodily absorption of electromagnetic radiation is specific absorption rate, or SAR. SAR is a measure of the rate at which the human body absorbs electromagnetic radiation, and it is measured in the amount of power absorbed per mass of tissue, with units of W/kg. Reported specific absorption rates tend to be averaged over the entire body or a small sample volume. According to the FCC's Maximum Permissible Exposure guidelines [26], the maximum allowable SAR limit is 1.6 W/kg. Designing biotelemetry antennas to reduce the SAR in body tissue is an active area of research [42, 43].

The segmented loop antenna used in this work is based in part on [42], but has been adapted to operate in the UHF ISM band to allow for greater communication bandwidth than the original 400 MHz operating frequency. The shift in operating frequency has been achieved through the inclusion of more segmentation, and altering of the loop diameter and track width. The octagonal segmented loop antenna used in this work has a diameter of 15 mm from one inner edge midpoint to another, and the trace width is 2 mm. The antenna is printed on a 62 mil thick FR-4 substrate. An EagleCAD layout of the octagonal segmented loop antenna, and the fabricated antenna are shown in Figures 4.10(a) and 4.10(b), respectively.

The advantage of utilizing a segmented loop as opposed to a closed loop becomes

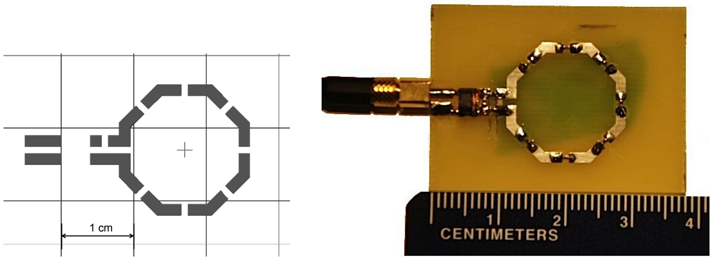

(a) EagleCAD layout model of octagonal segmented loop

(b) Fabricated octagonal segmented loop antenna, showing balun, balanced matching network, and gap capacitors

FIGURE 4.10: Near field octagonal segmented loop antenna

apparent in Figures 4.11(a) - 4.11(d). As the transmit loop antenna will be in close proximity to lossy, dielectric media, the guided wavelength inside this media causes the transmit antenna to appear electrically large. The current distribution around an electrically large loop is non-uniform, and thus produces an E-field with sharp peaks, as well as a weak H-field. By breaking the loop into segments and placing an appropriately sized capacitor within these gaps to compensate for current phase, the current distribution around the loop can be made uniform, causing the electrically large loop to appear electrically small. This allows for an E-field which is more uniform and has less sharp peaks, as seen in Figures 4.11(a) and 4.11(b), as well as a stronger H-field due to the in-phase current around the loop. Figure 4.11(c) shows the H-field from a closed loop, while Figure 4.11(d) shows the H-field from a segmented loop with 7 gaps, and 8 pF capacitors connecting the segments. These simulations were performed in CST Microwave Studio 2010.

Maximum power transfer in the biotelemetry system must be achieved through an antenna matching network. The use of a segmented loop antenna, while beneficial for biotelemetry, makes designing a matching network challenging, as the antenna is a balanced device and no ground plane is present. Moreover, as the antenna will be used in close proximity to highly conductive and lossy media, living human

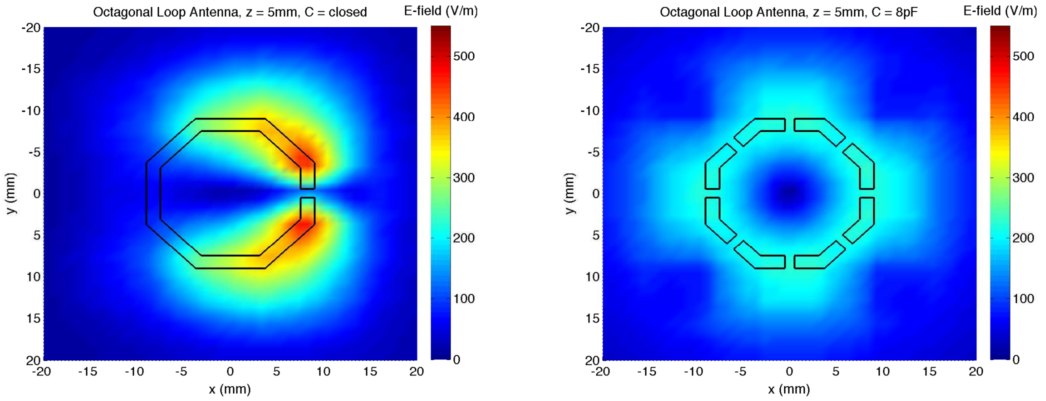

(a) Closed loop E-field

(b) Segmented loop E-field

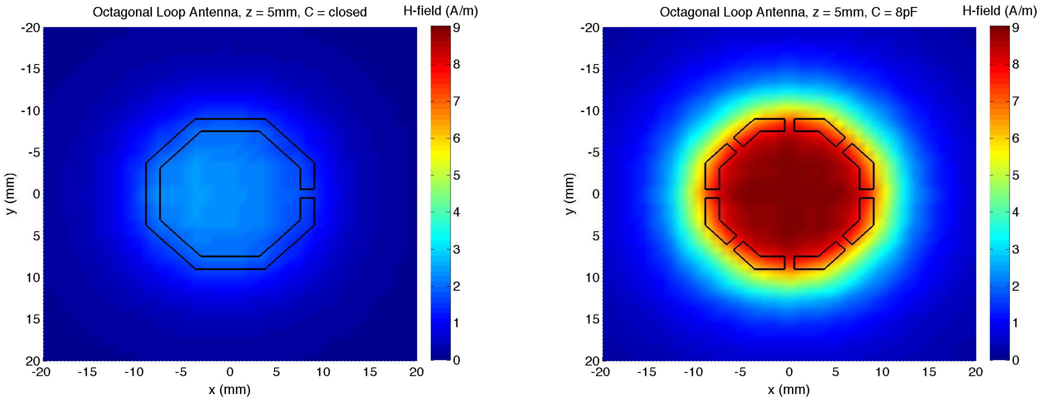

(c) Closed loop H-field

(d) Segmented loop H-field

FIGURE 4.11: Electric and magnetic fields created by octagonal segmented loop antenna

tissue ultimately, it must be matched in this scenario, as its impedance will change depending on the surrounding material and the antenna's distance from surrounding objects.

A balanced matching network as shown in Figure 4.12, including a balun, provided the best match in close proximity to a polyethylene tank of 0.91% saline, used as a tissue proxy. The matching network is balanced but not symmetric and comprises two series capacitors, and a shunt capacitor and inductor. Table 4.3 shows the impedance of the loop at 915 MHz, as well as the values of matching components.

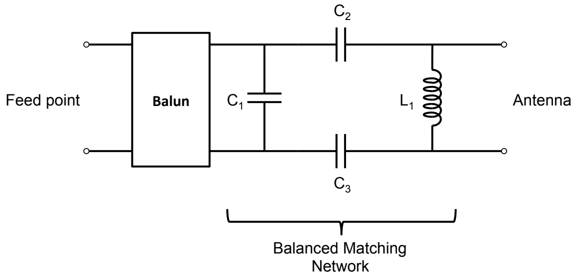

FIGURE 4.12: Matching network for small octagonal segmented loop

Table 4.3: Octagonal Segmented Loop Matching Network Components

Frequency	Impedance	Component	Value
915 MHz	$11.60 + j61.08\,\Omega$	C_1	6.8 pF
		C_2	8.2 pF
		C_3	8.2 pF
		L_1	39 nH

Figure 4.13 shows the measured S_{11} of the octagonal segmented loop and balanced matching network to be approximately -19 dB while the antenna is in close proximity to the tank of saline. Also shown in this plot are measured S_{11} values of the same antenna and matching network when in close proximity to a piece of chicken breast, a good proxy for muscle tissue. The measured return loss for the alternate surrounding medium is worse than that near the tank of saline, as S_{11} for the chicken is approximately -12 dB. This is due to the fact that the matching network was designed for the segmented loop antenna's impedance when near the tank of saline. However, even with this matching network, the return loss of the antenna is suitable for use near the other medium tested, raw chicken.

4.5.2 Digital Telemetry IC

A previously described digital telemetry integrated circuit (IC) [3] is highly integrated and compact with the die measuring 2.36 mm x 1.88 mm x 250 μm. A full block diagram of the chip is shown in Figure 4.14. For wireless operation, three off-chip components are required: a miniature-sized 20 MHz quartz crystal used for

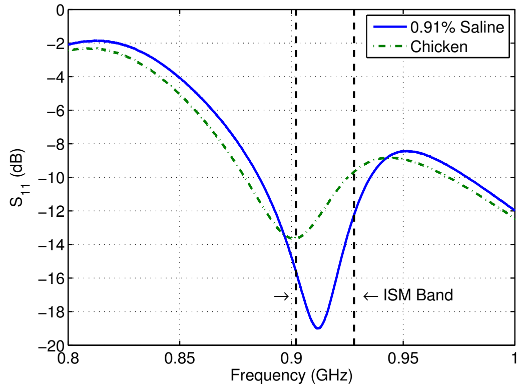

FIGURE 4.13: Measured S_{11} of the octagonal segmented loop antenna near different conducting media

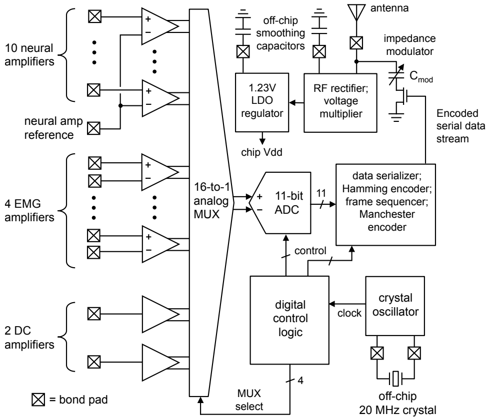

FIGURE 4.14: Block diagram of the digital telemetry IC (From [3])

clock generation and ADC timing and two 0402 SMD capacitors for the harvested, unregulated power supply and the regulated power supply. The implantable package used for the experiments described in this work, in addition to the three required components, includes an optional antenna impedance matching network consisting of two additional 0402 SMD components.

Full details of the digital telemetry IC are available in [3].

4.5.3 Backscatter Modulator

The IC is capable of continuous operation of the 5.0 Mbps data stream by greatly reducing the communication system power draw as compared to conventional wireless systems. This is achieved by implementing a near-field UHF backscatter circuit that reflects binary phase-shift keyed (BPSK) data when in the presence of a UHF carrier. This is realized using a shunt capacitance in the input RF path of the IC. In presenting a time-varying impedance to an antenna within a CW field, the reflected field from the antenna contains time-varying data with magnitude relative to the modulation depth. The reflected data can then be recovered by comparing the received, reflected field to a copy of the transmitted signal. Simulation indicates the entire communication subsystem consisting of the near-field backscatter modulation circuit draws only 19.65 μW.

The backscatter modulation depth of the telemetry IC is user-configurable by selecting a capacitance in a range between 62.5 nf – 500 nF. This allows for a user tradeoff between increasing power absorbed by the chip's energy harvesting circuit by choosing a smaller modulation depth or increasing power reflected for communication by choosing a deeper modulation depth. Demodulation and data recovery by the external base station are covered in Section 4.5.5.

4.5.4 RF Power Harvester and Voltage Regulator

The telemetry IC is designed for continuous operation without aid of a battery or external power supply affixed to the chip. Instead, all DC operating power is harvested from an external UHF field generated by the base station. The field absorbed by a loop antenna is passed into a voltage multiplying circuit that converts the low-voltage UHF signal into a high-voltage DC signal. This is accomplished by a 4-stage Schottky diode-based voltage multiplier. As the distance and phase relationship between the transmitter and telemetry chip is altered due to physical motion or a variable implantation depth, the harvested voltage will also vary. For this reason a DC voltage regulator is used to maintain a constant system voltage of 1.23 V.

4.5.5 Base Station Receiver

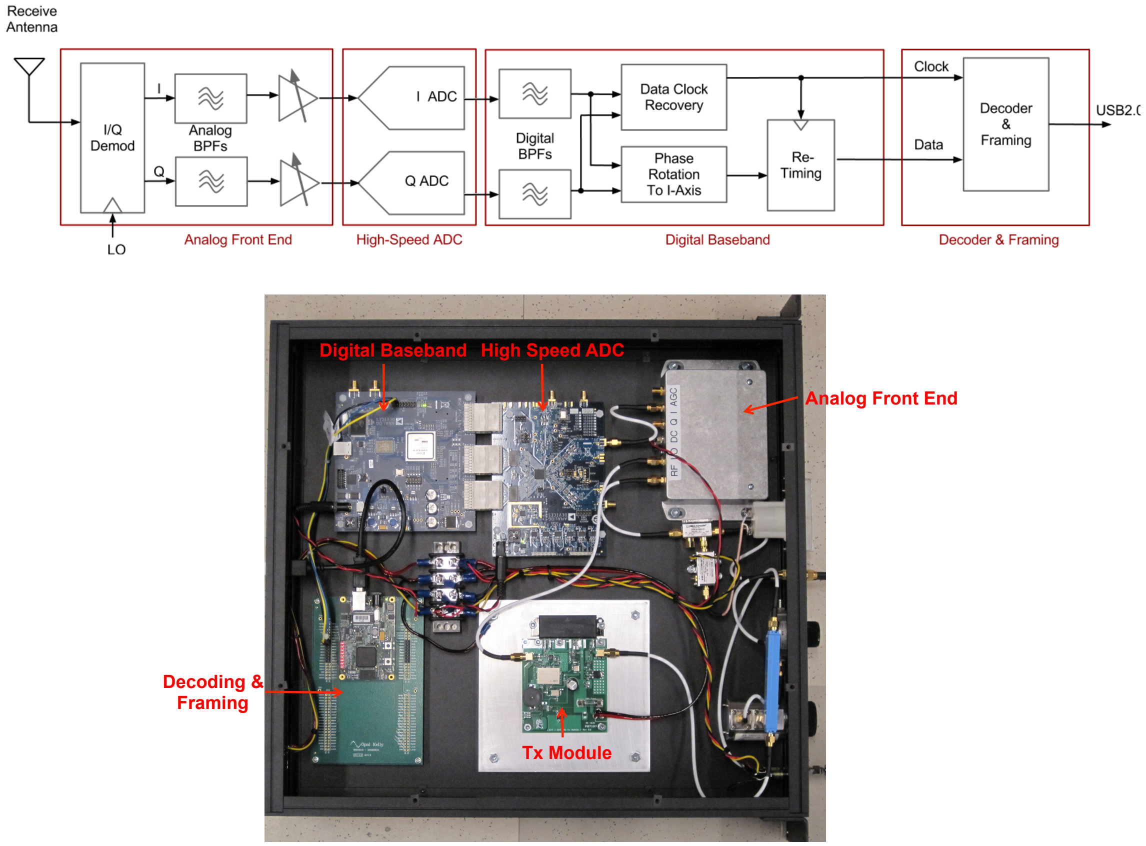

FIGURE 4.15: *Top:* A block diagram of the receiver architecture. *Bottom:* Photographs of the analog front end, high-speed analog-to-digital converter, digital baseband (FPGA), and decoder / framing FPGA.

A block diagram and photograph of the RF receiver is shown in Figure 4.15. This is a direct conversion design with a digital baseband section. By presumption, our system is forward-link limited, so the receiver's analog front end (AFE) is optimized for large-signal performance at the expense of noise figure. The AFE has sensitivity better than -70 dBm [3]. According to Figure 4.22 and 4.23, the receiver should be able to detect and decode the modulated-backscatter data for all experimental implantation depths up to approximately 2.5 cm. However, the current digital architecture (a filter-type CDR recovery circuit [44]) possesses a sensitivity of -45 dBm at a data rate of 5.0 Mbps and BER $< 10^{-5}$. Thus, our system currently operates at implantation depths up to 1.5 cm. Examples of demodulated data from the base station receiver can be seen in Section 4.5.6.

4.5.6 Measurement Results

The telemetry IC, shown with attached loop antenna and off-chip components in Figure 4.16, was characterized in two scenarios meant to mimic surrounding biological tissue. The first test setup used a polyethylene tank filled with 6 liters of 0.91% mass/volume of saline, which acted as the tissue proxy. The telemetry device was placed inside a latex glove to protect the circuitry, while a sliding plastic rig was used to keep measurements consistent. The test setup used for the saline experiment is shown in Figure 4.17. The second test setup used a piece of chicken breast as a tissue proxy, as shown in Figure 4.18, as this will more accurately mimic muscle tissue in the body.

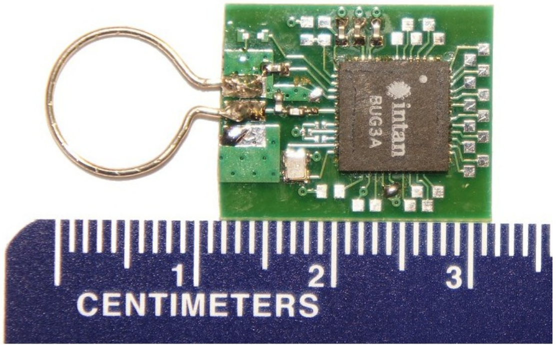

FIGURE 4.16: Telemetry chip with attached 1 cm diameter loop transponder antenna

For both tissue proxy scenarios, the experimental setup as shown in Figure 4.19 was used. A signal generator producing a 915 MHz, +10 dBm signal is used to excite the transmit antenna, with a power amplifier (Mini-Circuits ZHL-5W-2G-S) before the bi-directional coupler (Mini-Circuits ZGBDC10-362HP+) in this monostatic setup producing +30 dBm at the transmit antenna. The reflected signal from

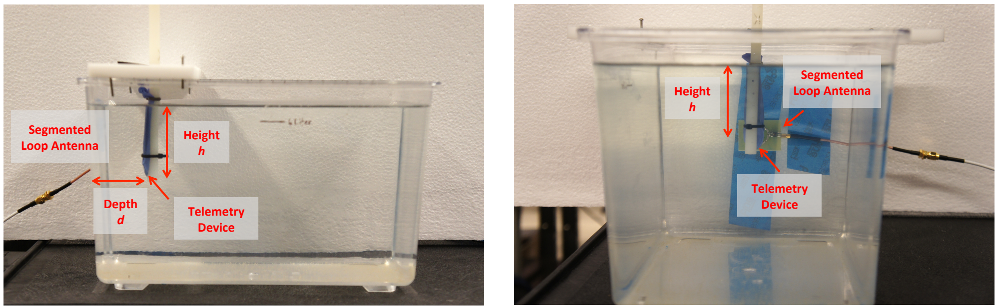

(a) Side view (b) Back view

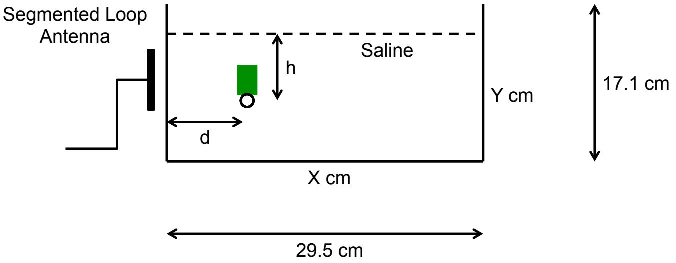

(c) Block Diagram

Figure 4.17: Backscatter test setup with saline proxy system

the telemetry IC is fed to the receive module through the reverse-coupled port along with the LO signal from the signal generator. Another integral component of the transceiver architecture is the self-jammer canceler, present on the forward-coupled port of the bi-directional coupler. The functionality of this component is explained in Section 4.5.7.

The transponder antenna used with the telemetry chip is a small loop, as shown in Figure 4.16. A small loop antenna was chosen as the wireless telemetry IC operates in the magnetic near field. The loop measures 9.55 mm in diameter and is constructed of 22 AWG wire (0.644 mm diameter). This diameter loop is of reasonable size to fit inside the skull of a mouse for future experiments. The loop itself is not matched to 50Ω, so a 2-element matching network was used to match the chip to the conjugate of the loop antenna's impedance, as shown in Figure 4.20.

The impedance of the chip remains essentially unchanged in the different media tested, and is approximately $5.96 - j12.17\,\Omega$ at an input power of +6 dBm in

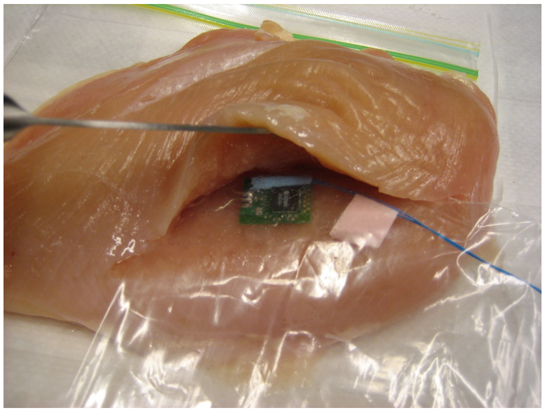

FIGURE 4.18: Experimental setup for measuring harvested voltage and backscatter from the telemetry IC. Biotelemetry device "implanted" inside chicken.

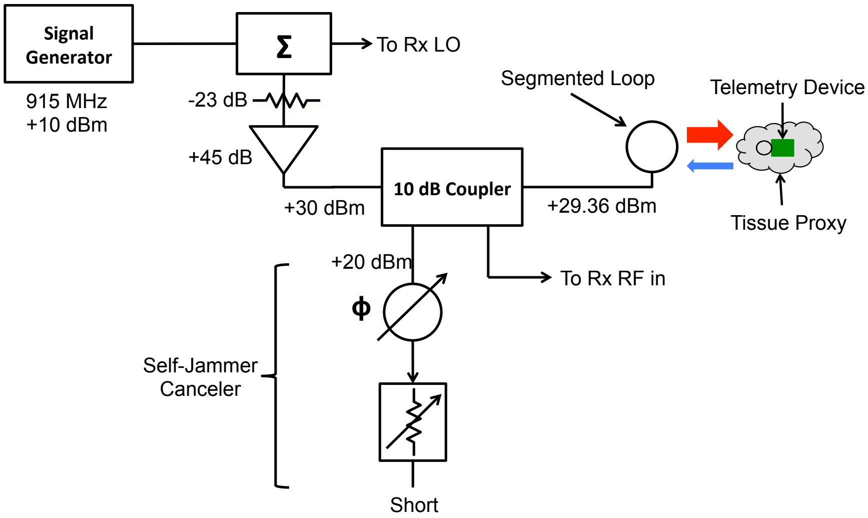

FIGURE 4.19: Block diagram of experimental setup for measuring backscattered data

free space, near the tank of saline, and near a piece of chicken breast. This input impedance was used to match the small loop antenna to the telemetry device. The impedance of the small loop antenna varies significantly with different media. Table 4.4 summarizes the impedance characteristics of the small loop antenna in the different media tested, as well as the values of the matching network elements.

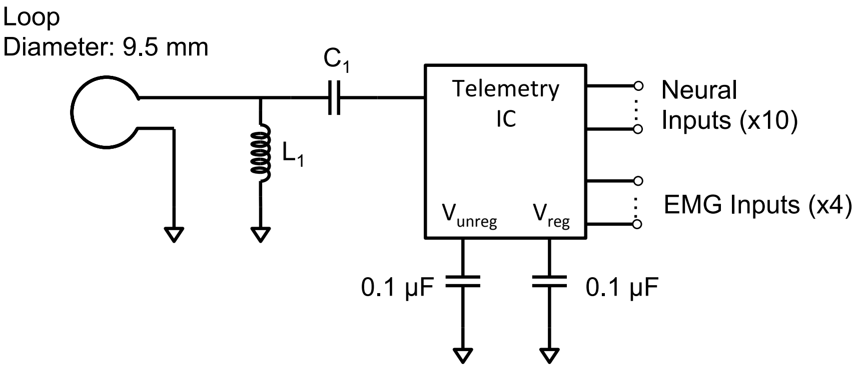

FIGURE 4.20: Measurement setup and matching the chip impedance to the small loop antenna in different media

Table 4.4: Impedance Characteristics of Small Loop Antenna

Media	Z_{loop} (Ω)	Matching Components	
		L_1	C_1
Free Space	$94.35 + j515.21$	30.46 nH	1.46 pF
Saline	$94 - j27$	4.7 nH	12 pF
Chicken	$125.08 - j145.15$	6.29 nH	5.96 pF

4.5.7 Self-Jammer Canceler

As with any RF communication system, a strong carrier signal aids in increasing communication distance, but on the receiver side, a strong self-jammer can cause problems within the receiver circuitry, making it difficult to extract the desired data. The self-jamming signal can be controlled and suppressed with a variable phase delay and step attenuator, which is able to step from 0 - 15 dB in 1 dB increments, at the forward coupled port of the bi-directional coupler.

A comparison of the backscatter envelope with and without the self-jammer canceler present is shown in Figure 4.21. The forward-coupled port was terminated when the self-jammer canceler was removed. With the self-jammer canceler present, the backscatter sidelobes are more prominent, and the self-jammer signal is significantly reduced. A summary of the performance of the self-jammer canceler is shown in Table 4.5. The figure of merit is the rejection ratio, computed as the difference, in

Table 4.5: Rejection Characteristics of Self-Jammer Canceler

	USB total power (dBm)	Self-jammer power (dBm)	USB rejection ratio (dB)
Without canceler	-28.64	11.87	-40.51
With canceler	-30.99	-20.20	-10.79

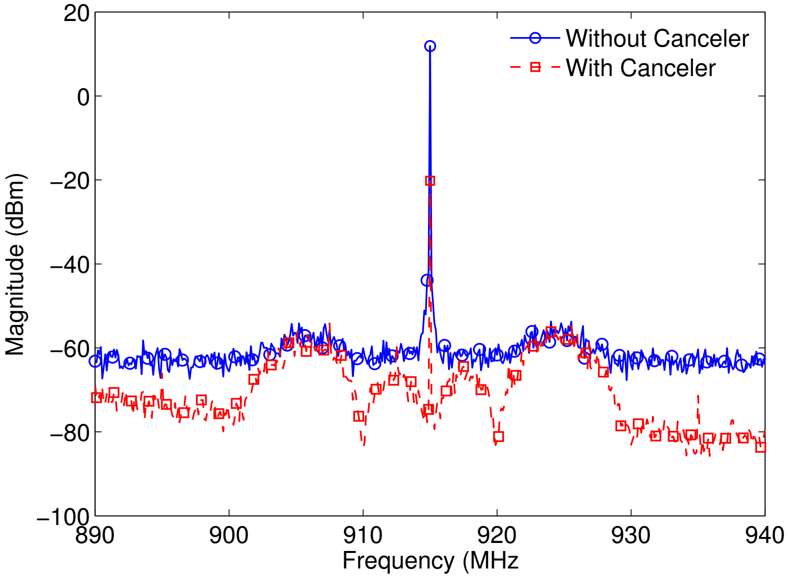

FIGURE 4.21: Backscatter envelope from telemetry device implanted at 0.5 cm with and without self-jammer canceler

dB, between the total power in the upper sideband and the power of the self-jammer. Including the self-jammer canceler decreases the total power in the upper sideband slightly, by about 2 dB, but suppresses the self-jamming signal by about 32 dB, such that the overall performance enhancement in terms of the rejection ratio is about 30 dB.

4.5.8 DC Power Breakdown

The power consumption of the telemetry IC has been investigated thoroughly in [3]. Its DC power consumption was measured by temporarily powering the chip's V_{unreg} from a bench supply. The total DC power consumption of the IC is 1.23

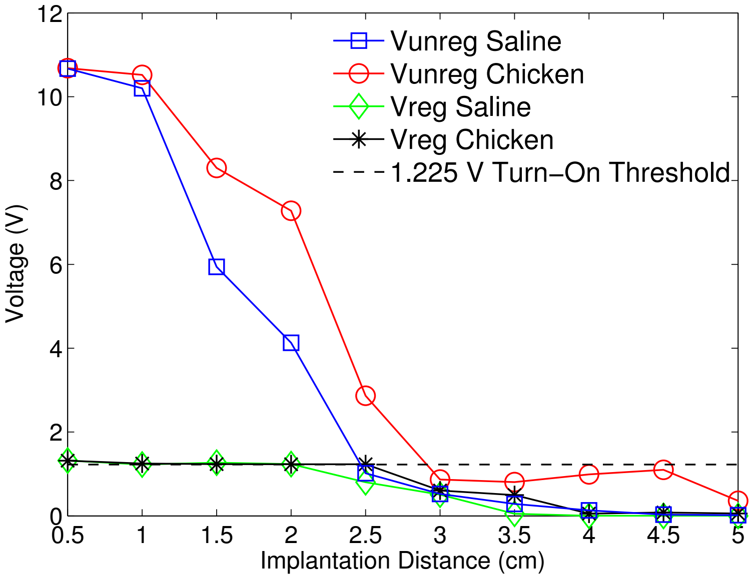

FIGURE 4.22: Measured regulated and unregulated harvested voltage at varying implantation depth in saline and chicken with a +30 dBm transmit power

mW. Of the total DC power consumption, the majority (84%) is dedicated to bio-signal acquisition (biopotential amps, ADC, and control logic), and the backscatter modulator used for communication consumes only 2% of the total system power.

4.5.9 Saline Tank Experiment

The unregulated, harvested voltage from the implantable IC was measured at varying depth in the saline solution. This data shown in Fig. 4.22 was obtained using a +30 dBm, 915 MHz signal applied to the near-field transmit antenna. The IC was positioned such that the loop antenna was parallel to the plane of the transmit antenna and moved radially outward.

The required turn-on voltage of the telemetry IC is 1.225 V. As expected, as the telemetry IC moves further away from the transmit antenna, the unregulated harvested voltage drops. The harvested voltage drops below the required threshold voltage at an implantation depth of about 2.5 cm. This data suggests that a 2 cm implantation depth is obtainable at these power-levels before being turn-on power limited. An implant depth of 2 cm is adequate for neural implants as well as cardiac and muscle telemetry devices.

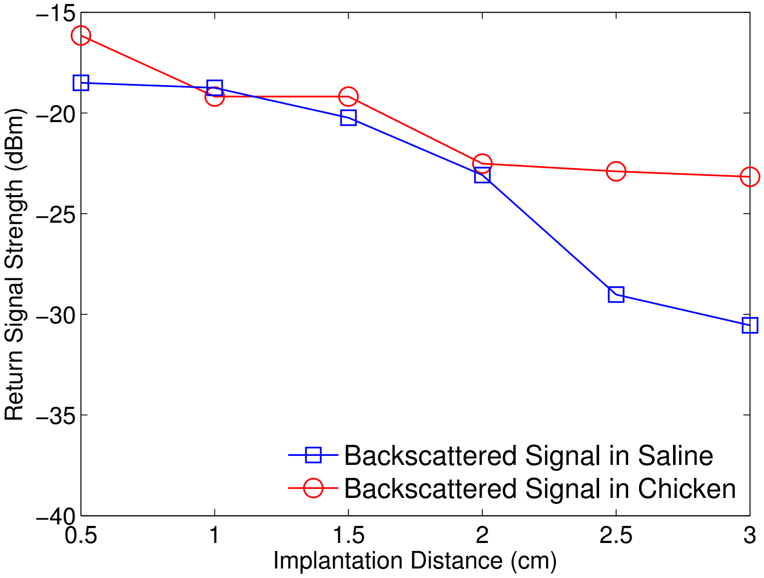

FIGURE 4.23: Measured backscatter signal strength at varying implantation depths. The value shown is the total power in the upper sideband (USB) of a double-sideband (DSB) signal, referenced to the receiving antenna.

The return signal strength was also characterized, and is shown in Figure 4.23. The backscatter signal strength is referenced to the receiving antenna. This value was determined by recording the backscattered frequency spectrum using an Agilent N9320B spectrum analyzer directly from the reverse-coupled port of the bi-directional coupler. An example backscatter spectrum is shown in Figure 4.25. While the spectrum reflected by the telemetry chip is a double-sideband (DSB) binary phase-shift keying (BPSK) modulation scheme, the reported values for return signal strength are only those of the upper sideband, from 920 - 930 MHz. In the saline tank, the backscattered signal strength falls between -18 and -30 dBm, referenced to the receiving antenna, from an implant depth of 0.5 - 3 cm. Beyond an implant depth of 3 cm, the telemetry IC did not harvest enough voltage to turn on and backscatter data.

However, when the chip is powered on via harvested voltage, the data sidebands are easily visible on the spectrum analyzer, and the ability to decode the backscattered data becomes a function of the receiver sensitivity, as explained in section 4.5.5. Figure 4.23 also shows that the backscattered signal strength of the telemetry IC inside the saline is weaker than that of the chip inside a piece of chicken breast at nearly each implantation depth tested. The reasoning behind this clear difference is explained in section 4.5.10.

An important aspect of one of the proposed applications for the biotelemetry device, the wireless recording of neural data, is the accuracy in reproducing the waveform present at the telemetry device, specifically the magnitude and timing of neural spikes, as this is where crucial information is stored. The telemetry device's demodulation performance was characterized by injecting various pre-recorded signals into the biopotential amplifiers and observing the output at an implantation depth of 1.5 cm. The results of this experiment are shown in Figure 4.24, where pre-recorded neural data was used. The pre-recorded neural data has been provided by the laboratory of Dario Ringach at UCLA and downloaded from the CRCNS web site. The neural data was collected from the primary visual cortex of Old-world monkeys. While the received data is slightly noisier than the original transmitted data, the magnitude and timing of each neural spike has been well preserved.

4.5.10 Chicken Experiment

A piece of raw chicken breast provided a second proxy for biological tissue, better approximating muscle tissue. The telemetry IC was inserted into a section of chicken breast as shown in Figure 4.18, and implanted further beneath the top of the chicken breast to record each data point.

Figure 4.22 shows the regulated and unregulated voltage the telemetry IC was able to harvest from the RF energy supplied by the segmented loop antenna at each implant depth. As in the case with the telemetry IC in saline, as the chip moves further away from the transmitting antenna, the harvested voltage drops. When the telemetry IC is 3 cm within the chicken, the harvested voltage drops just below the necessary turn-on threshold, and at this point and beyond the IC is no longer powered up and will not backscatter data. These results suggest that an implantation depth of 2.5 cm is achievable with the current antenna designs, similar to the case with the saline tissue proxy. With an implantation depth of about 2.5 cm, the chip was observed to be fully powered and backscattering data with a measured unregulated, harvested voltage of approximately 3 V.

As in the saline channel characterization, the return signal strength was also measured with the telemetry IC implanted inside the chicken breast and the results are shown in Figure 4.23. With the telemetry IC implanted in the chicken, the return signal strength ranges between approximately -16 dBm and -24 dBm over the range 0.5 - 3 cm. For implantation depths beyond 3 cm, the data sidebands are no longer visible as the chip is not harvesting enough power to backscatter data. Within the implant range where the telemetry IC is able to harvest enough voltage to turn on and begin backscattering data, the data sidebands become clearly visible in the frequency spectrum before the receiver, as shown in Figure 4.25. The received backscatter power levels for the telemetry IC in the chicken give an idea of how sensitive the receiver needs to be such that the backscattered data can be decoded. With the appropriate receiver architecture, the telemetry IC's data can be demodulated and decoded.

The return signal strength for the telemetry IC implanted in the chicken is greater than, or comparable to, the IC within the saline at each implant depth tested. The smallest difference between the return signal power in each case is about 0.5 dB at an implant depth of 1 cm. The reason that the telemetry IC is able to backscatter more power when implanted in the chicken, and harvest more voltage as well (Figure 4.22),

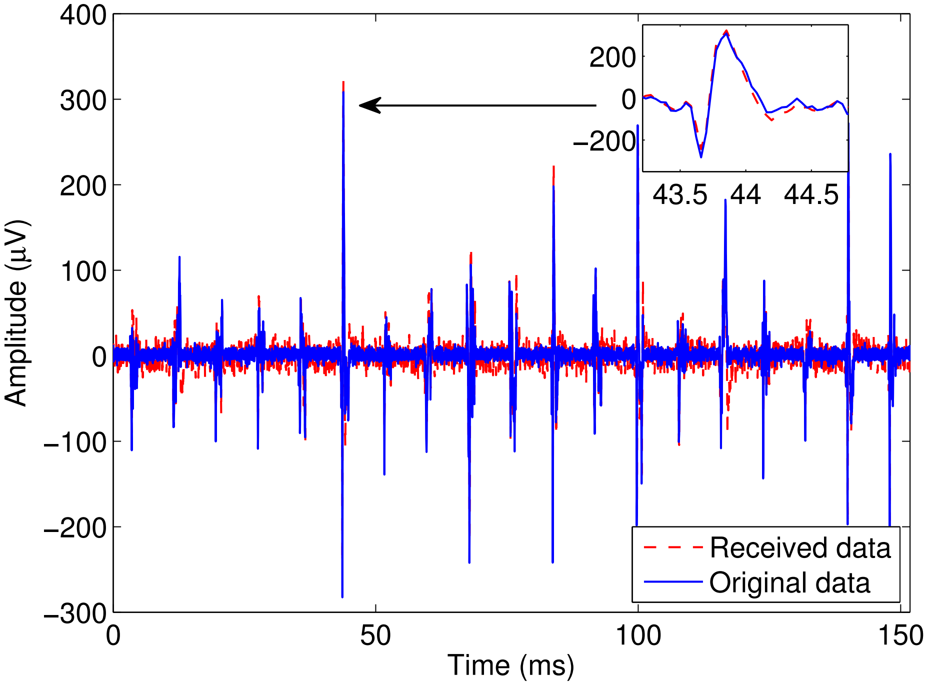

FIGURE 4.24: Result of injecting pre-recorded neural data into the telemetry device and demodulating the output. The device is "implanted" in saline at a depth of 1.5 cm. The data rate is 5.0 Mbps with BER $< 10^{-5}$.

can be explained by the concept of skin depth. Skin depth is the distance within a given material over which the electromagnetic fields decay by e^{-1}, or 36.8%. Skin depth is inversely proportional to the square root of the conductivity, or equivalently, proportional to the square root of the resistivity [45]. The resistivity of chicken breast is about 3 times that of 0.91% saline, according to [46] and [47]. Thus, the skin depth of chicken breast is about $\sqrt{3}$, or 1.73, times that of the skin depth of saline. Electromagnetic waves will thus penetrate chicken breast more easily than saline, and they will be attenuated less over the same distance. The electromagnetic field providing energy for the telemetry chip and the reflected field will face less attenuation in the chicken, so more harvested voltage and a stronger return signal would be expected. This is reflected in the data in Figures 4.22 and 4.23.

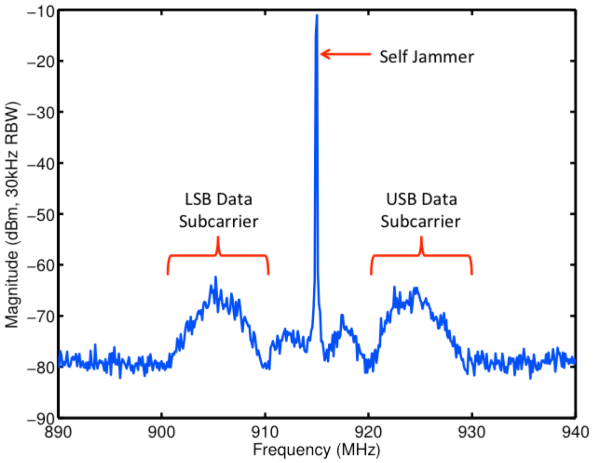

FIGURE 4.25: Measured return signal from wirelessly powered IC implanted in chicken at a depth of 1.5 cm

4.6 Conclusion

In this chapter, it has been shown that using near field UHF telemetry with modulated backscatter is a promising avenue for implanted biotelemetry. The segmented loop antenna, when used as the external transceiver antenna in the near field backscatter system, matches well to both free space and saline, and it performs well in the near field at UHF frequencies with a small loop of a size suitable for *in vivo* applications in rodents or other small animals. This combination has been validated using a prototype modulated backscatter board demonstrating signal transfer in a tissue proxy at 7.5 MHz, 15 MHz and 30 MHz, and penetration depths of up to 6 cm. Biological tissue is less lossy than normal saline, and it is expected that a greater communication distance could be achieved within living tissue [7, 40]. Given spectral efficiency on the order of 1 bps/Hz, communication rates up to 30 Mbps could be achieved using the system presented in this work. This bandwidth would be able to handle the raw data produced by a typical 10 x 10 microelectrode array without the need for data reduction. While operating at a bandwidth of 30 Mbps, the essential communication element of the backscatter board, an RF switch, consumes about 164 μA at approximately 3 V, for a power consumption of 0.49 mW, and 16.4 pJ/bit. The proposed biotelemetry system is competitive in terms of power consumption with the systems shown in Table 3.2, and its maximum data rate and energy per bit outperform the systems shown.

After the near field link was characterized and communication deemed possible in a forward link-limited situation, an existing wireless biotelemetry ASIC [3] was used to verify enough voltage could be harvested at typical implant depths, and that realistic biological data could be reliably transmitted and demodulated over the near field link. The communication system using the ASIC addresses design challenges facing biotelemetry systems such as power consumption and communication rate. The proposed system includes a base station receiver as well, which provides the necessary RF energy as well as demodulates and decodes the recorded data from the telemetry IC. The telemetry IC takes advantage of the greater carrier frequencies in the UHF band (902 - 928 MHz), and is able to communicate back to the receiver using modulated backscatter at a rate of 5 Mbps with a BER $< 10^{-5}$ while consuming 1.23 mW. The proposed system is able to power the telemetry IC at an implant depth of up to 2.5 cm, as well as demodulate and decode the uplinked data while preserving timing from the implant at a rate of 5 Mbps for implantation depths of up to 1.5 cm.

5

Radio Frequency (RF) Single-Wire Transmission Line (SWTL) For Implanted Devices

5.1 Introduction

Wireless biotelemetry devices often take advantage of the magnetic near field, as biological tissue has a low magnetic permeability, allowing the magnetic field to be relatively unaffected by tissue proximity. The proposed implantable system in the previous section utilizes the magnetic near field for communication and powering of the implantable device, tailoring the antenna designs to function in this modality. Magnetically coupled systems often have a modest implantation depth, on the order of centimeters, in part due to the tradeoff between antenna coil diameter and the depth at which good coupling efficiency can be achieved, given a particular operating frequency [48, 49]. The transmitter power, operating frequency, and available bandwidth are in turn constrained by FCC regulations [26].

The use of a single wire transmission line (SWTL) to permit an increased implant depth without incurring unacceptable signal transmission loss is proposed. A SWTL consists of a wire surrounded by a dielectric medium. Unlike a coaxial cable, there is

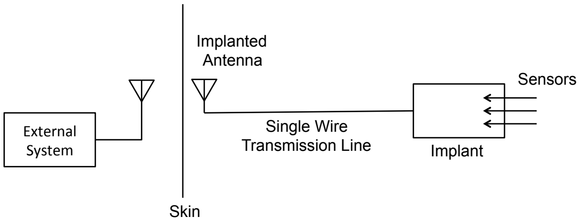

(a) An implanted device using a single-wire transmission line

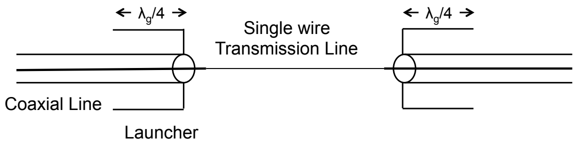

(b) Schematic of the proposed launcher design

FIGURE 5.1: Single-wire transmission line concept

no outer conductor surrounding the dielectric. We consider the case where the wire is surrounded by a composite medium consisting of a biocompatible insulator such as silicone or Teflon fluorinated ethylene propylene (FEP), surrounded by biological tissue.

SWTLs have the potential to be thinner, less expensive, and more flexible than coaxial cable, but have the disadvantages of higher loss and increased tissue absorption compared to coax. Compared to wireless approaches, signals guided by transmission lines such as SWTLs have the potential for spectral reuse among nearby devices, and less susceptibility to unwanted interference. We imagine that existing conductive leads used to carry near-DC biopotential signals (e.g. electrode wiring for recording or stimulation) could perform double-duty as SWTLs in some applications.

An example application scenario is shown in Figure 5.1(a). In this example, the skin is bridged by a conventional transcutaneous magnetic near field link. Using the proposed SWTL, the antenna can remain close to the skin for high wireless coupling efficiency, while the SWTL connects the antenna to the implanted device at some much greater implant depth. This is shown in more detail in Figures 5.2(a) and 5.2(b). Signals are coupled into the SWTL via a “launcher” at each end, as shown in Figure 5.1(b). A theoretical model of the SWTL in lossy dielectric media is presented, as well as initial proof-of-concept impedance and loss measurements using a 0.91% saline solution as a homogeneous tissue proxy, and raw chicken breast as a muscle tissue proxy.

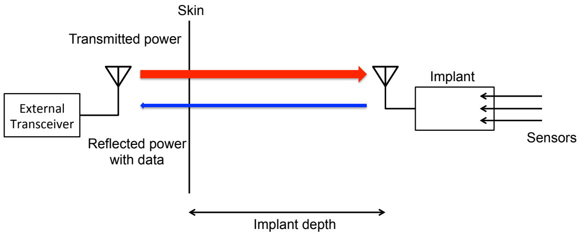

(a) Implantable device at increased depth using conventional magnetic near field coupling over increased implantation depth

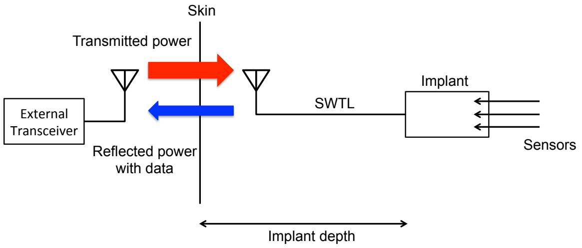

(b) Implantable device using SWTL to increase implantation depth. The SWTL is more efficient than near field coupling for certain distances within tissue.

FIGURE 5.2: Benefits of using a single-wire transmission line for routing RF signals within the body. Implant depth is decoupled from communication and harvesting depth. The implanted antenna can be kept close to the skin for coupling efficiency, while the implant resides at a greater depth using the SWTL.

5.2 Single-Wire Transmission Line In Free Space

The single-wire transmission line was characterized in 1950 by George Goubau [50], building on the prior work of Sommerfeld and Zenneck, who focused on single conductor transmission lines and ground (earth) return waves repsectively [51, 52]. Sommerfled and Zenneck showed that a single smooth cylindrical conductor of finite conductivity can support a surface wave. However, since the field extent outside the conductor extends to great distances, designing a launching device to couple to the surface wave modes would be impractical, and the wire surface had to be modified to reduce the field extent and excitation device. Goubau reconsidered this surface wave phenomena in the context of waves on a conductor with a modified surface, and their practical application as transmission lines.

The appeal of these surface wave transmission lines, or “G-lines” as they are also known, is that they are capable of lower loss than standard coaxial cables, albeit with the need for a specialized launching device.

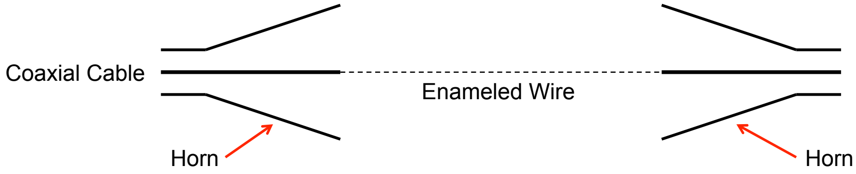

FIGURE 5.3: Single-wire transmission line as visualized in the work of Goubau [50]. The launching devices are shown as an extension of coaxial cables to couple into the surface wave mode of the single-wire line.

The single-wire transmission line operates on the phenomena of surface waves, an evanescent wave mode that often arises at the boundary between two dielectrics. For a surface wave to exist, the signal must decay exponentially away from the surface, indicating that it is an evanescent mode and that energy is not radiated into the surrounding dielectric like an antenna. This exponential decay of the wave away from the surface indicates that energy is “trapped,” or “bound” to the surface allowing it to travel close to the surface. Since energy is not lost to radiation due to the evanescent mode, surface waves can provide an efficient means for transmission depending on the dielectrics involved. Surface waves are being investigated for their use in many THz systems.

A diagram of the single-wire transmission line as conceptualized by Goubau is shown in Figure 5.2.

The ground shielding of a coaxial cable is used to feed a horn launching device, which is used to couple from the TEM coaxial mode to the surface wave mode on the single-wire transmission line. The center conductor of the coaxial line is fed to an enamel coated single-wire line, and then connected to the center conductor of the receiving coaxial cable. The launcher on the opposite end is used to couple from the surface wave mode back to the TEM mode in the coaxial cable.

Essentially, Goubau discovered that for a surface wave mode to exist on a single cylindrical conductor, the phase velocity of the signal must be smaller than the normal velocity in the surrounding dielectric, which in this case is free space. This condition can be met through any surface modification of the conductor, either threading the wire or covering it in a dielectric coating (insulation). Modifying the surface of the conductor using either method produces a transmission line capable of supporting surface waves.

Another factor Goubau considered is the launching, or excitation, device. This is a device on either end of the single-wire transmission line used to couple between the surface wave modes and those used outside of the single-wire line. These launchers must be efficient, otherwise they will add to the loss of the single-wire transmission line. Moreover, the size of the launchers is dependent on the field extent outside of the single-wire line. These launchers must capture the majority of the evanescent energy for an overall efficient system. The extent of the fields outside the single-wire line are dependent upon frequency and the thickness of the single-wire line. Thus, launcher sizes are most practical for signals above 100 MHz.

5.2.1 Analytic Model

Based on the electromagnetic boundary conditions, Goubau was able to derive a characteristic equation and model for the single-wire transmission line in free space. The surface wave condition was assumed in determining the relationship between the electric and magnetic fields surrounding the single-wire transmission line, for fields both in the dielectric coating and in the surrounding dielectric, free space. From this, the loss of the single-wire transmission line with a dielectric coating could be determined, as shown below:

$$L_{100\text{ ft.}} = \frac{P(\gamma' a')}{a\sqrt{\lambda}} + \frac{\epsilon}{\epsilon_i - \epsilon} \tan\delta \frac{\lambda}{a'^2} Q(\gamma' a') \text{ [dB]} \tag{5.1}$$

$$P(\gamma' a') = -1.33 \times 10^4 \sqrt{\frac{\epsilon}{\mu}} \sqrt{\frac{\pi \mu_c}{\sigma_c \mu}} \frac{1}{\ln \gamma' a' + 0.38} \tag{5.2}$$

$$Q(\gamma' a') = 2.11 \times 10^3 \left(1 - \frac{0.5}{\ln \gamma' a' + 0.38}\right) \tag{5.3}$$

Here, L is the loss per 100 feet of the single-wire transmission line, a is the radius of the conductor, a' is the radius of the outer surface of the dielectric coating, ϵ is the free space permittivity, ϵ_i is the dielectric coating permittivity, $\tan\delta$ is the loss tangent of the dielectric coating material, λ is the wavelength in free space, γ' is equal to $\sqrt{h^2 - k^2}$, h is the propagation constant, k is the free space wavenumber, μ is the permeability of free space, μ_c is the permeability of the conductor, and σ_c is the conductivity of the conductor.

The first term in equation 5.1 represents the loss in the conductor, and the second represents the loss in the dielectric coating.

To show the low loss nature of the single-wire transmission line in free space, if we consider $\lambda = 50$ cm, $\gamma' a' = 1.21 \times 10^{-1}$, $a = 0.94$ cm, $a' = 1.00$ cm, and $\epsilon_i/\epsilon = 4$, $\tan\delta = 10^{-3}$, and a copper inner conductor. Using equations 5.1 - 5.3, we find that the total loss of this transmission line over 100 feet is approximately 0.062 dB. A standard type of coaxial cable, RG-316DS, has a loss of approximately 20 dB over 100 ft at approximately the same frequency (600 MHz). The loss of the coaxial cable is much greater than that of the single-wire transmission line, although the single-wire transmission line requires the inclusion of large – on the order of 15 cm for this frequency – launching devices. The launching devices will add at most a couple dB to the overall single-wire loss, still placing it 10 times below the loss of the coaxial cable.

While the derived model from Goubau is applicable in free space, placing the single-wire line is a highly conductive dielectric will alter its properties and the modes it is able to support. To determine the feasibility of using the single-wire transmission line in living tissue to increase implantation depth and route RF signals among implantable devices, the single-wire line must be analyzed in these situations.

5.3 Single-Wire Transmission Line In High Permittivity Dielectrics

Single-wire transmission line theory has also been extended to lossy dielectric media by Rao [53]. Rao considers the propagation of an ultra-wideband, subnanosecond pulse along a SWTL that is completely immersed in oil, a lossy dielectric medium. However, the model derived here assumes surface wave propagation along the coated conductor, as the loss tangent and relative permittivity of the surrounding dielectric, crude oil, is less than that of the dielectric coating considered. Thus, this system meets the criteria for supporting a surface wave.

With the increased loss tangent and permittivity of living tissue, the modes supported by a single-wire transmission within living tissue must be investigated. It has been shown by John *et al* in [54] that for certain combinations of the loss tangent of the dielectric coating, the loss tangent of the surrounding dielectric media, and the permittivity of the dielectric coating, surface wave modes are not supported. The supported wave modes of propagation for a G-line in a highly conductive dielectric media is investigated below using full 3D EM simulation software.

5.3.1 *Wave Modes Supported By A SWTL Immersed In High Conductivity Dielectrics*

To investigate the wave modes supported by a SWTL in a high conductivity, lossy dielectric, full wave 3D EM simulations were performed in CST Microwave Studio. A SWTL with an inner conductor radius of 0.143 mm and an outer dielectric radius of 0.2413 mm was constructed. The SWTL was fed with a standard RG-316 coaxial cable on each end, using a quarter-wavelength sleeve balun as the launching device [55]. Two simulations were performed, one with the SWTL in free space, and the other with the SWTL in 0.91% saline, as this was used as a tissue proxy in previous experiments. The simulation results are shown in Figure 5.4(a) and 5.4(b), a single frame from sweeping the phase.

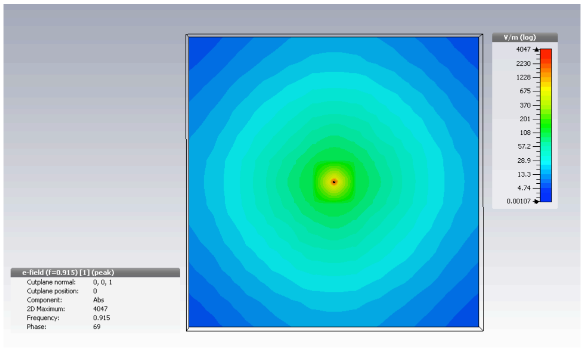

e-field (f=0.915) [1] (peak)
Cutplane normal: 0, 0, 1
Cutplane position: 0
Component: Abs
2D Maximum: 4047
Frequency: 0.915
Phase: 69

(a) E-field distribution around a SWTL in free space

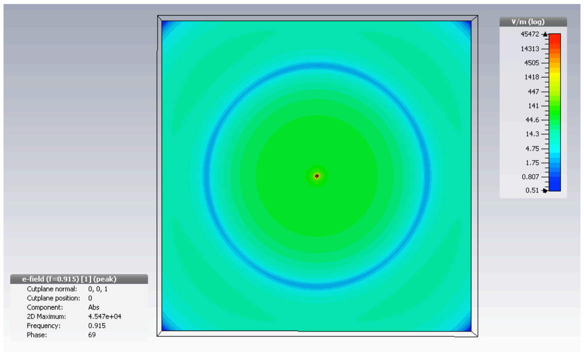

e-field (f=0.915) [1] (peak)
Cutplane normal: 0, 0, 1
Cutplane position: 0
Component: Abs
2D Maximum: 4.547e+04
Frequency: 0.915
Phase: 69

(b) E-field distribution around a SWTL immersed in 0.91% saline

FIGURE 5.4: E-field distribution around a SWTL in various media. The SWTL is going into the plane of the page.

The dielectric properties for the 0.91% saline were derived from [40]. At a temperature of 20 degrees Celsius and a frequency of 915 MHz, the relative permittivity of the 0.91% saline is $\epsilon_r = 76.8 - j31.7$. For the SWTL in free space in Figure 5.4(a), it is clear that the E-field is not radiating from the single-wire and decays exponentially in the radial direction into free space, indicating an evanescent mode as predicted and described by Goubau [50]. For the SWTL in saline in Figure 5.4(b), the E-field does not experience a simple exponential decay radially from the single-wire line, as evidenced by the clear minimum in the E-field surrounding the wire followed by a field increase and then decrease again toward the edges of the tested area. This indicates that the single-wire transmission line does not support an evanescent wave mode in the surrounding dielectric, saline, and that it radiates energy in the radial direction, acting in a sense similar to an antenna. This is unlike the single-wire transmission line in free space, where energy is stored in the radial field but does not radiate.

Since the single-wire transmission line in a highly conductive dielectric does not support an evanescent wave mode in the surrounding dielectric, the surface wave mode that exists due to the boundary between the dielectric wire insulation and the surrounding dielectric medium (tissue) does not propagate along the axial direction of the single-wire line efficiently, and will incur proportionately greater loss than the surface wave mode supported by the G-line in free space. This is mainly due to the loss of energy in the form of radiation in the radial direction. The field extent in the radial direction in the surrounding dielectric moving away from the wire will be greater, and causes the surface wave to be loosely bound to the surface and more inefficient than the G-line in free space. Moreover, the surface wave mode that travels along the single-wire transmission line exists in a highly conductive and lossy dielectric, also owing to the greater loss of the SWTL in saline when compared to a G-line in free space.

The analytical model for the SWTL in a highly conductive dielectric, such as normal saline, must include the existence of hybrid modes supported by the SWTL. An accurate model of the SWTL in highly conductive media will allow for optimization in the design choices when employing this type of waveguide. These design choices include conductor radius, dielectric insulation radius, frequency, length, expected axial and radial loss, and will inform the design of the launcher. The next section focuses on the derivation of an model for the SWTL in highly conductive dielectrics.

5.3.2 Analytical Model

For the SWTL in a highly conductive dielectric, the fundamental wave mode is the TM_0 mode, as in the G-line in free space. This implies a radially symmetric field distribution, where there is no ϕ dependence. Simulations also confirmed this wave mode to be the fundamental. Using this fundamental wave mode, we can write the electric and magnetic fields in both the dielectric coating and the surrounding dielectric. A cross section of the SWTL in a highly conductive dielectric is shown in Figure 5.5. The naming convention of field components, as well as the radii of the inner conductor and dielectric coating as shown in Figure 5.5 will be used as the convention in the following derivation.

Since the TM_0 mode is the fundamental mode, this implies that $H_z^d = 0$. So, a solution for E_z^d is assumed, and the other field components are derived from it. The field components in the dielectric coating of the wire, for $r_i \leqslant \rho \leqslant r_0$ can be written as follows, where the superscript d indicates the wire dielectric coating, the A_i's and B_i's are constants, J_n is a bessel function of the first kind, and Y_n is a bessel function of the second kind:

$$E_z^d = \left[A_1 J_0\left(\gamma_\rho^d \rho\right) + B_1 Y_0\left(\gamma_\rho^d \rho\right)\right] A_3 e^{-j\gamma_z z} \tag{5.4}$$

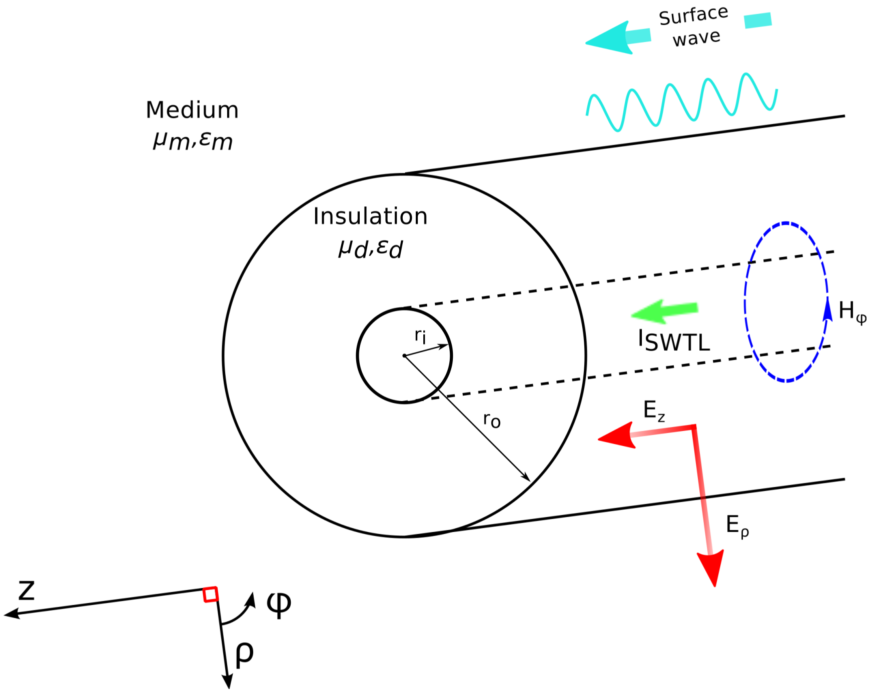

FIGURE 5.5: Cross section of the SWTL in a highly conductive dielectric, showing fundamental field modes. The inner conductor radius is r_i, the outer conductor radius is r_o.

$$E_\rho^d = -\frac{\gamma_z}{\gamma_\rho^d}\left[A_1 J_1\left(\gamma_\rho^d \rho\right) + B_1 Y_1\left(\gamma_\rho^d \rho\right)\right] A_3 e^{-j\gamma_z z} \tag{5.5}$$

$$E_\phi^d = 0 \tag{5.6}$$

$$H_z^d = 0 \tag{5.7}$$

$$H_\rho^d = 0 \tag{5.8}$$

$$H_\phi^d = -\frac{k_d^2}{\gamma_\rho^d}\frac{1}{j\omega\mu_d}\left[A_1 J_1\left(\gamma_\rho^d \rho\right) + B_1 Y_1\left(\gamma_\rho^d \rho\right)\right] A_3 e^{-j\gamma_z z} \tag{5.9}$$

Here, ${k_d}^2 = \left(\gamma_\rho^d\right)^2 + {\gamma_z}^2$, where k_d is the complex wavenumber in the dielectric coating, and $k_d^2 = k_0^2 \epsilon_r^d \left(1 - j \tan\delta_d\right)$, for ${k_0}^2 = \omega^2 \mu_0 \epsilon_0$. Each γ is the propagation constant in the given direction, such that $\gamma_\rho^d = \alpha_\rho^d + j\beta_\rho^d$, and $\gamma_z = \alpha_z + j\beta_z$, where α is the attenuation constant in Np/m, and β is the phase constant in radians/m. Finally, μ_d is the permeability of the dielectric coating around the wire.

As with the dielectric insulation, we can assume a solution for E_z^m in the surrounding dielectric medium (tissue) and solve for the field components in this region. Here, the superscript m refers to the surrounding media, A_m is a constant, and $H_n^{(2)}$ is a hankel function of the second kind. For $r_o \leqslant \rho < \infty$, we have:

$$E_z^m = A_m H_0^{(2)} \left(\gamma_\rho^m \rho\right) e^{-j\gamma_z z} \tag{5.10}$$

$$E_\rho^m = -\frac{\gamma_z}{\gamma_\rho^m} A_m H_1^{(2)} \left(\gamma_\rho^m \rho\right) e^{-j\gamma_z z} \tag{5.11}$$

$$E_\phi^m = 0 \tag{5.12}$$

$$H_z^m = 0 \tag{5.13}$$

$$H_\rho^m = 0 \tag{5.14}$$

$$H_\phi^m = -\frac{k_m^2}{\gamma_\rho^m} \frac{1}{j\omega\mu_m} H_1^{(2)} \left(\gamma_\rho^m \rho\right) e^{-j\gamma_z z} \tag{5.15}$$

Here, $\gamma_\rho^m = \alpha_\rho^m + j\beta_\rho^m$ is the propagation constant in the radial direction in the surrounding dielectric. Also, ${k_m}^2 = k_0^2 \epsilon_r^m \left(1 - j \tan\delta_m\right) = \left(\gamma_\rho^m\right)^2 + \gamma_z^2$. Finally, μ_m is the permeability of the surrounding dielectric.

Boundary Conditions

Applying the appropriate boundary conditions allows a derivation of the characteristic, or eigenvalue, equation for the SWTL immersed in a highly conductive dielectric. The boundary conditions to apply here are as follows:

$$E_z^d\left(\rho = r_i, \phi, z\right) = 0 \tag{5.16}$$

$$E_z^d\left(\rho = r_o, \phi, z\right) = E_z^m\left(\rho = r_o, \phi, z\right) \tag{5.17}$$

$$H_\phi^d\left(\rho = r_o, \phi, z\right) = H_\phi^m\left(\rho = r_o, \phi, z\right) \tag{5.18}$$

Applying 5.16, we find that:

$$A_1 = -B_1 \frac{Y_0\left(\gamma_\rho^d r_i\right)}{J_0\left(\gamma_\rho^d r_i\right)} \tag{5.19}$$

which leads to:

$$E_z^d = A_3 B_1 \left[\frac{J_0\left(\gamma_\rho^d r_i\right) Y_0\left(\gamma_\rho^d \rho\right) - J_0\left(\gamma_\rho^d \rho\right) Y_0\left(\gamma_\rho^d r_i\right)}{J_0\left(\gamma_\rho^d r_i\right)}\right] e^{-j\gamma_z z} \tag{5.20}$$

Applying the second boundary condition, equation 5.17, we have:

$$A_3 B_1 \left[\frac{J_0\left(\gamma_\rho^d r_i\right) Y_0\left(\gamma_\rho^d r_o\right) - J_0\left(\gamma_\rho^d r_o\right) Y_0\left(\gamma_\rho^d r_i\right)}{J_0\left(\gamma_\rho^d r_i\right)}\right] = A_m H_0^{(2)}\left(\gamma_\rho^m r_o\right) \tag{5.21}$$

Applying the final boundary condition, equation 5.18, we have:

$$\frac{k_d^2}{\gamma_\rho^d}\frac{1}{\mu_d}A_3B_1\left[\frac{J_0\left(\gamma_\rho^d r_i\right)Y_1\left(\gamma_\rho^d r_o\right)-J_1\left(\gamma_\rho^d r_o\right)Y_0\left(\gamma_\rho^d r_i\right)}{J_0\left(\gamma_\rho^d r_i\right)}\right]=\frac{k_m^2}{\gamma_\rho^m}\frac{1}{\mu_m}A_mH_1^{(2)}\left(\gamma_\rho^m r_o\right) \tag{5.22}$$

Dividing equation 5.22 by 5.21, we arrive at the eigenvalue equation for the SWTL in a highly conductive dielectric medium:

$$\frac{k_m^2}{\gamma_\rho^m}\frac{1}{\mu_m}\frac{H_1^{(2)}\left(\gamma_\rho^m r_o\right)}{H_0^{(2)}\left(\gamma_\rho^m r_o\right)}=\frac{k_d^2}{\gamma_\rho^d}\frac{1}{\mu_d}\left[\frac{J_0\left(\gamma_\rho^d r_i\right)Y_1\left(\gamma_\rho^d r_o\right)-J_1\left(\gamma_\rho^d r_o\right)Y_0\left(\gamma_\rho^d r_i\right)}{J_0\left(\gamma_\rho^d r_i\right)Y_0\left(\gamma_\rho^d r_o\right)-J_0\left(\gamma_\rho^d r_o\right)Y_0\left(\gamma_\rho^d r_i\right)}\right] \tag{5.23}$$

Combining the eigenvalue equation with the following:

$$k_m^2=k_d^2-\left(\gamma_\rho^d\right)^2+\left(\gamma_\rho^m\right)^2 \tag{5.24}$$

and separating into real and imaginary components results in 4 simultaneous nonlinear equations that can be used to solve for the 4 unknowns: α_ρ^d, β_ρ^d, α_ρ^m, and β_ρ^m. This gives us the attenuation and phase constants in the radial direction in both the dielectric coating on the single-wire line and the surrounding highly conductive dielectric. These quantities can then be used to determine the axial propagation constant, γ_z, which is the same for each dielectric to conserve field quantities and continuity at the boundaries.

Using the analytical model for the single-wire transmission line, we can determine the properties of the SWTL, as well as the type that will be suitable for use to guide RF signals within living tissue. This is discussed in the next section.

5.3.3 Properties Of A SWTL In High Permittivity Dielectrics

To gain insight into the properties of the SWTL in highly conductive dielectrics and to better inform design choices in integrating the SWTL into a wireless implantable system, the analytical model can be used to investigate various design factors. The factors considered here are the conductor radius (wire gauge), insulation thickness, and frequency.

To understand the effect the conductor radius and insulation thickness have on the propagating wave modes, both the conductor radius and insulation thickness are swept, and at each point, the analytic model is solved for all attenuation and phase constants using a nonlinear optimizer. The frequency was held constant at 915 MHz, as this is the center frequency of the UHF ISM (Industrial, Scientific, and Medical) radio band, and the frequency considered for the proposed fully implantable wireless communication system. Figures 5.6(a) and 5.6(b) show the results of the simulation.

Figure 5.6(a) describes the field extent of the energy radiated in the radial direction in the surrounding dielectrc. This is lost energy, as it will not reach the desired destination at the opposite end of the SWTL. Thus, a greater loss here indicates energy that is bound closer to the SWTL, and a smaller loss indicates energy that extends further out into the surrounding dielectric and is bound more loosely to the SWTL. It is desired that the field extent of the wasted, radiated energy be as small as possible, thus a high loss is desired in this region. This allows the energy to be bound more tightly to the WTL, increasing the efficiency of the surface wave carrying the desired energy. It is clear that for a given insulation thickness, a thicker center conductor of the SWTL causes the radiated energy to extend further, creating a loosely bound mode. Moreover, for a given conductor radius, a thicker insulation bounds the energy closer to the SWTL.

This is reflected in Figure 5.6(b), as the thicker insulation provides less loss in the axial direction. The 180 μm thick insulation incurs the greatest radial decay, indicating the energy is more tightly bound to the SWTL, and this same insulation thickness also provides the lowest axial loss. Moreover, as the conductor thickness increases, so too does the axial loss, as the radial field becomes more loosely bound

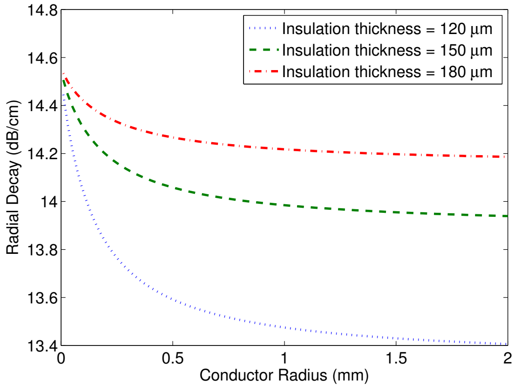

(a) Radial loss of a 915 MHz signal transmitted using a SWTL in 0.91% saline. This shows the loss of the signal traveling perpendicularly away from the single-wire line.

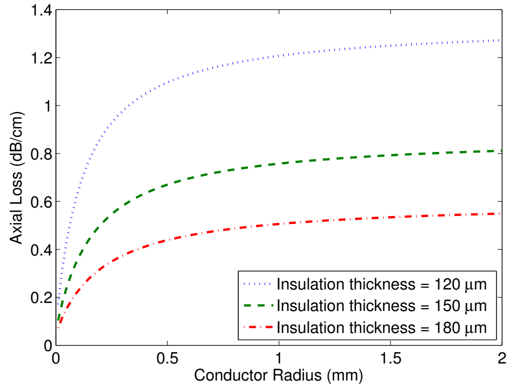

(b) Axial loss of a 915 MHz signal transmitted using a SWTL in 0.91% saline. This is the loss of the signal traveling parallel to the wire, and the energy that is "guided" by the SWTL and reaches the desired location.

FIGURE 5.6: Radial and axial loss of a 915 MHz transmitted signal using a SWTL in 0.91% saline.

to the SWTL. From this simulation, it appears that the best choice of SWTL is that with a thin inner conductor but thick dielectric insulation. The insulation thickness will have to be optimized with tissue displacement specifications as well.

Another factor to consider is the frequency of operation. For a given inner conductor radius and insulation thickness, the frequency will affect the propagating wave modes of the SWTL. To investigate this, the frequency was swept from 100 MHz - 3 GHz for 3 specific wire gauges and insulation thicknesses. We consider American

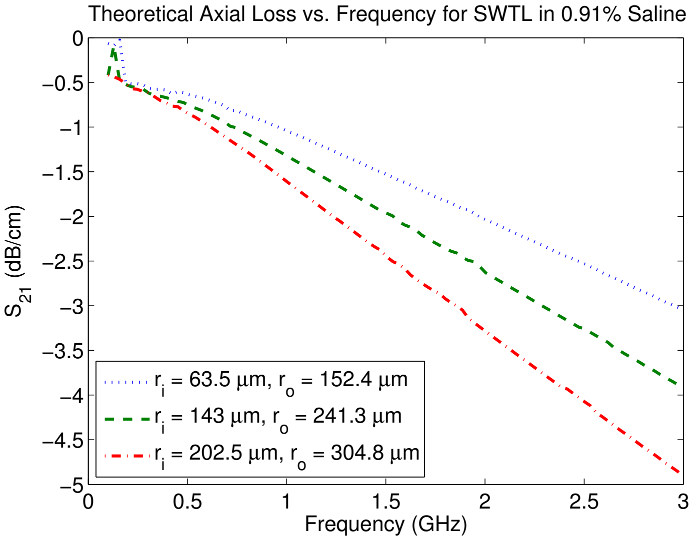

Figure 5.7: Theoretical loss of the SWTL line for various wire gauges over a frequency range of 100 MHz - 3 GHz

wire gauges of 36 (0.127 mm), 29 (0.286 mm), and 26 (0.405 mm), which are commonly available with Teflon FEP (fluorinated ethylene propylene) insulation with insulation radii of 0.1524 mm, 0.2143 mm, and 0.3048 mm respectively. Using these wire specifications, which are commercially available, the derived SWTL model was used to determine the axial loss over frequency. These results are shown in Figure 5.3.3.

In agreement with the previous simulation, the thinner wires perform better at each frequency, in that the axial loss is decreased. Additionally, as the frequency increases, the loss also increases for each wire gauge simulated. However, the loss increases with frequency at different rates among the wire gauges and insulation thicknesses simulated. This nonlinear loss increase with frequency must be considered in optimizing the efficiency of an SWTL in a practical system. This analytical model will aid in guiding practical designs using an SWTL for routing RF signals in living tissues, a highly conductive dielectric environment, and will aid in integrating an SWTL in a fully implantable, passive wireless device utilizing near field modulated backscatter.

To verify the practicality of using an SWTL as a method of routing RF signals in living tissue, experimental measurements were performed, as shown in the next section.

5.4 Experimental Measurements

The derived analytical model of the SWTL in highly conductive dielectric media is verified with experimental results.

Thinner SWTLs are more flexible and cause less disruption when implanted, so we consider American wire gauges of 36 (0.127 mm), 29 (0.286 mm), and 26 (0.405 mm), which are commonly available with Teflon FEP (fluorinated ethylene propylene) insulation with insulation radii of 0.1524 mm, 0.2143 mm, and 0.3048 mm respectively. We consider biological media of muscle tissue, brain tissue, and 0.91% (g/mL) saline. The saline is used as a tissue proxy for experimental results and verification, and its properties were calculated using the Debye relaxation method [40]. Table 5.1 shows the dielectric properties of all media considered, calculated at a frequency of 915 MHz which is the center of the commonly used 902 - 928 MHz Industrial, Scientific, and Medical (ISM) band.

Table 5.1: Properties of Selected Dielectric Media at 915 MHz

Dielectric	ϵ_r'	ϵ_r''	$\tan\delta$	σ (S/m)
Saline (0.91%)	76.8	31.7	0.4128	1.4128
Muscle tissue	54.997	18.626	0.33866	0.94809
Brain tissue (grey)	52.654	18.637	0.35394	0.94866
Teflon FEP	2.05	0.002255	0.0011	10^{-15}

Table 5.2 shows the theoretical loss in dB/cm of a SWTL in each medium, based on the derived analytical model, given the dielectric properties of Table 5.1. We observe that the thinnest wire gauge, AWG 36, is the least lossy in each medium

considered, while the AWG 29 and AWG 26 wires perform similarly. More importantly, the loss incurred per unit length of a SWTL in these media are significantly less than that due to near field coupling over an equivalent distance at implant depths of 1-10 cm or longer [49], as shown in Figure 5.11. The predicted loss in saline is significantly greater than in the other media, primarily due to the higher conductivity of the saline. Because the saline medium is expected to be the worst-case, and given the convenience of working with saline, a saline proxy system was selected for initial proof-of-concept experiments. These experiments are described in Sections 5.4.1 and 5.4.2 below.

Table 5.2: Theoretical SWTL Loss at 915 MHz

Wire Gauge (AWG)	Loss (dB/cm) Saline (0.91%)	Muscle Tissue	Brain Tissue
36	0.97	0.91	0.93
29	1.2	1.05	1.1
26	1.5	1.3	1.4

5.4.1 Experimental Setup

Initial validation was performed using 0.91% saline as a homogeneous tissue proxy. Three 10 cm SWTL test sections were fabricated using AWG 26, 29, and 36 conductors. The guided wavelength λ_g was calculated given the saline properties of Table 5.1, and a sleeve balun [55] of length $\lambda_g/4$ was used as a launcher at each end of the SWTL. The sleeve balun and the connection to the SWTL were coated in a thin layer ($\approx$ 1 mm) of RTV silicone to form a watertight insulating layer over all exposed metal. Each SWTL section was immersed, one at a time, in a 5 L tank of 0.91% saline, and submerged at the center of the tank. The RG-316DS coaxial feed lines were supported by a plastic mounting rig as shown in Fig. 7.1.

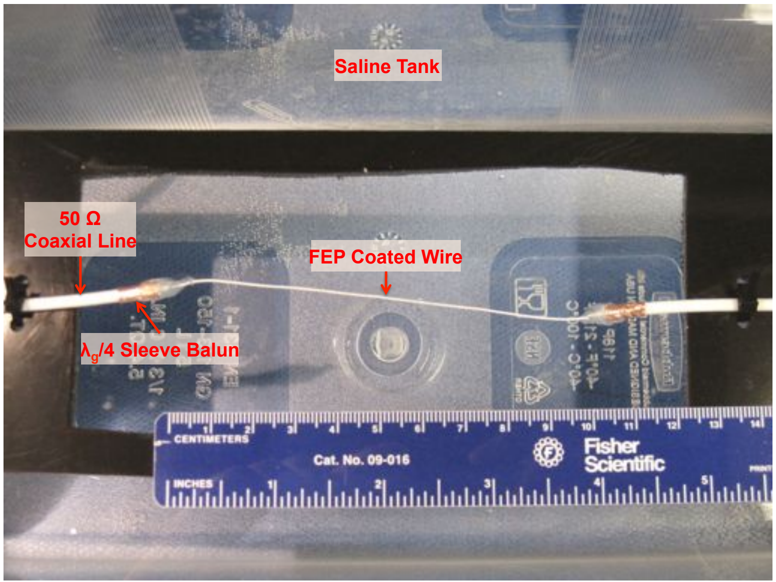

FIGURE 5.8: Saline tank shown with AWG 29 SWTL section

5.4.2 Results

A full 2 port calibration was performed on an Agilent E5062A network analyzer, and the losses of the RG-316DS coaxial feed lines were measured for de-embedding. Figure 5.9 shows the return loss $|S_{11}|$ of each 10 cm SWTL section, measured with the SWTL terminated in 50 Ω.

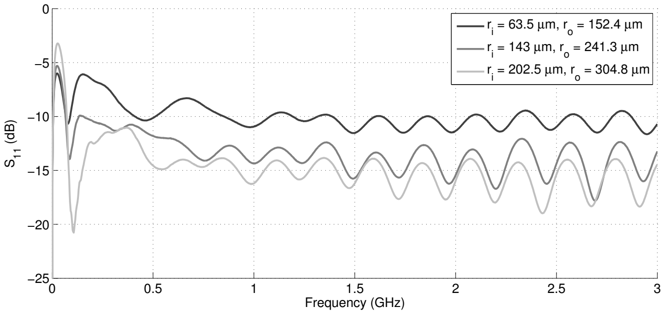

FIGURE 5.9: Measured return loss vs. frequency for the 10 cm SWTLs immersed in 0.91% saline

For the AWG 26 and 29 SWTLs, the measured $|S_{11}|$ is less than -10 dB for all frequencies in the 100 MHz - 3 GHz range. The AWG 36 SWTL is not as well matched as the AWG 26 and 29 SWTLs, but still has a median S_{11} of less than -10 dB.

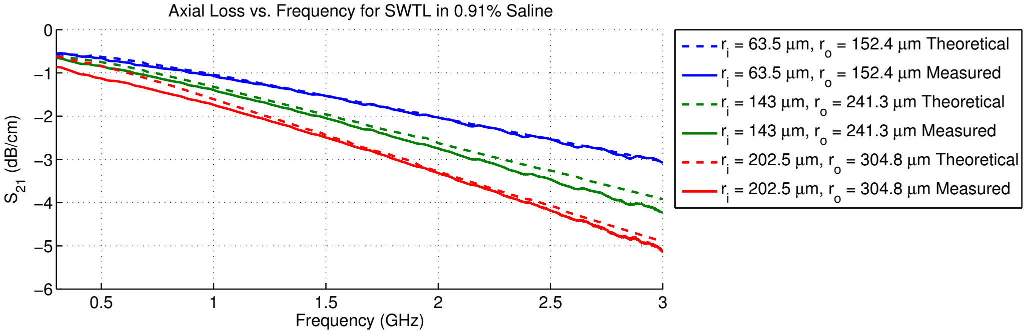

FIGURE 5.10: Measured insertion loss vs. frequency for the SWTLs in dB/cm when immersed in 0.91% saline compared to theoretical results

Figure 5.10 shows the measured insertion loss $|S_{21}|$ of each SWTL in dB/cm versus frequency. The thinnest wire tested, AWG 36, has the lowest loss over all frequencies tested. The AWG 26 SWTL exhibited the highest loss over the frequency range of 100 MHz - 3 GHz. The theoretical results are included, to verify the derived model for the single wire transmission line (SWTL). There is good agreement between measured and theoretical results in the 300 MHz - 3 GHz range. Table 5.3 shows the measured insertion loss of each SWTL at 915 MHz with a comparison to the theoretical values calculated earlier. We attribute the discrepancy mainly to the relatively uncontrolled dielectric properties of the 0.91% saline, as its dielectric properties vary greatly with temperature and the presence of impurities. The measured results also agree with the theory that the AWG 36 wire was expected to have the lowest loss.

Table 5.3: Measured vs. Predicted Insertion Loss of SWTLs in 0.91% Saline at 915 MHz

Wire Gauge (AWG)	Measured $|S_{21}|$ (dB/cm)	Theory $|S_{21}|$ (dB/cm)	Δ (Theory - Measured)
36	-1.00	-0.97	0.03
29	-1.30	-1.2	0.1
26	-1.63	-1.5	0.13

One factor which may explain the discrepancy between measured and theoretical results is that the analytical model assumes an infinite surrounding dielectric, and that the radiated fields reach 0 at infinity (represented by Hankel functions). In reality, there are boundaries where the test rig, tank walls, and water level reside. Each of these points will reflect some energy back to the wire, resulting in areas of constructive and destructive interference, owing to a lower loss than that predicted by the theoretical model.

The benefit of using a SWTL over near field coupling to route RF signals within tissue is illustrated in Figure 5.11. In the radiating near field, the strength of the emitted field components decays as $1/r^2$, while the loss incurred over a SWTL of inner radius $63.5\,\mu$m and outer radius $152.4\,\mu$m is approximately 1 dB/cm at 915 MHz (measured). Considering the loss of these signal routing methods over distance, the SWTL achieves significantly less loss than near field coupling for distances up to 60 cm. This range where the SWTL is a more efficient RF signal routing method covers all practical implant depths.

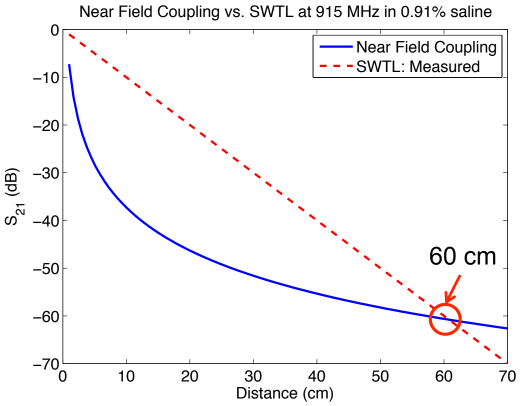

FIGURE 5.11: Near field coupling vs. SWTL loss at 915 MHz

As shown by the previous CST simulations as well as the theoretical model, the SWTL radiates energy into the surrounding dielectric. In a realistic situation, this energy would be absorbed by living tissue surrounding the SWTL. To verify that a

SWTL is practical to use in a realistic wireless implantable sensing system, it must not exceed the FCC limits [26] for exposure to radiation. SAR measurements are difficult to carry out accurately, especially because any radiators in the presence of an antenna's near field will affect the field distribution and power draw. To verify that the SWTL's meet the FCC limits, simulations were carried out in CST Microwave Studio for each wire gauge immersed in 0.91% saline. These results are shown in Figures 5.12(a) - 5.12(f).

For further verification, the same wire gauges were tested as SWTL's inside raw chicken breast, a better proxy for muscle tissue. The setup for testing the SWTL's in chicken is shown in Figures 5.13(a) and 5.13(b).

The same launcher design used for the saline experiment with the SWTL's is applied for this measurement. Parafilm wax is used to seal each end of the SWTL to prevent corrosion and shorting of the coaxial cable and SWTL. The return loss and insertion loss of the SWTL in the raw chicken is shown in Figures 5.14(a) - 5.14(f)

The SWTL in raw chicken does not have the same resonating effect in the return loss when compared to being immersed in saline. It is not as well matched to a $50\,\Omega$ system for each wire gauge tested as the SWTL in saline, but still sufficient for use in a practical system as the return loss for each wire gauge tested is approximately -10 dB in the UHF ISM band. The insertion loss follows the same linear decreasing trend in the range of 500 MHz - 3 GHz, but appears to have a resonating effect in the range 300 kHz - 500 MHz. This effect is present at frequencies not considered for use in the proposed UHF system, and can be attributed to the Parafilm wax seal being used, as well as the size of raw chicken breast used, as less of the SWTL is covered when compared to the SWTL tested in saline.

The measured S_{21} of the SWTL "implanted" in chicken is -1.7 dB/cm for the AWG 26 wire, -1.5 dB/cm for the AWG 29 wire, and -1.2 dB/cm for the AWG 36 wire. These loss values further verify the validity of using the SWTL as a method

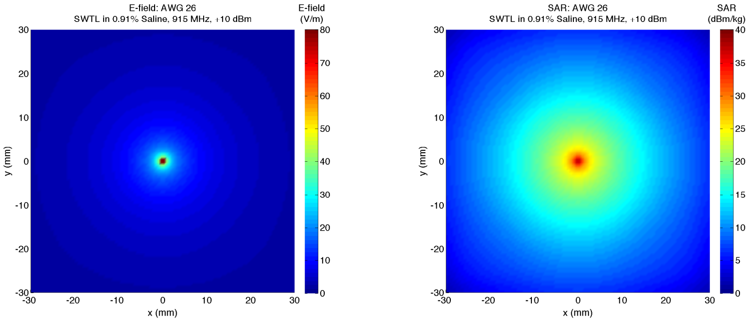

(a) E-field around AWG 26 wire in saline, +10 dBm input

(b) SAR around AWG 26 wire in saline. SAR averaged over 1 g = 0.72 W/kg

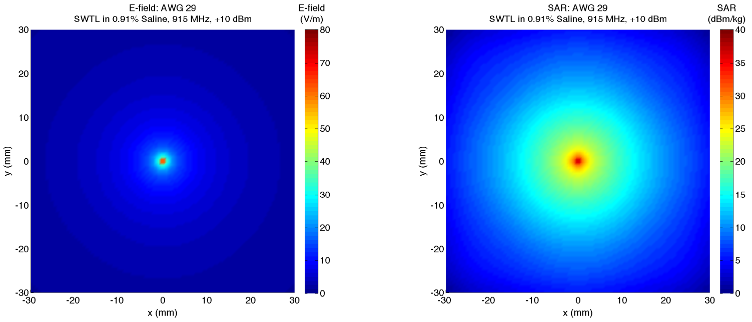

(c) E-field around AWG 29 wire in saline, +10 dBm input

(d) SAR around AWG 29 wire in saline. SAR averaged over 1 g = 0.45 W/kg

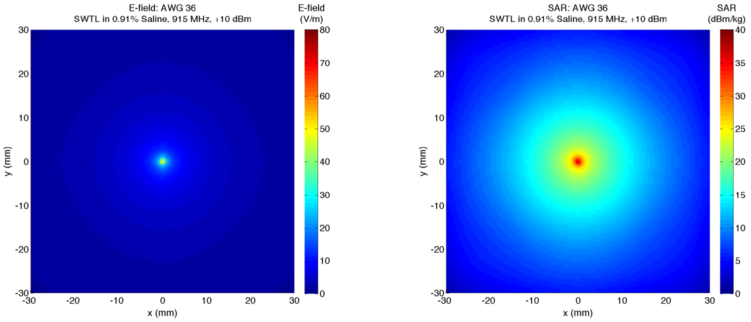

(e) E-field around AWG 36 wire in saline, +10 dBm input

(f) SAR around AWG 36 wire in saline. SAR averaged over 1 g = 0.33 W/kg

FIGURE 5.12: Simulated E-field and SAR around SWTL's immersed in 0.91% saline

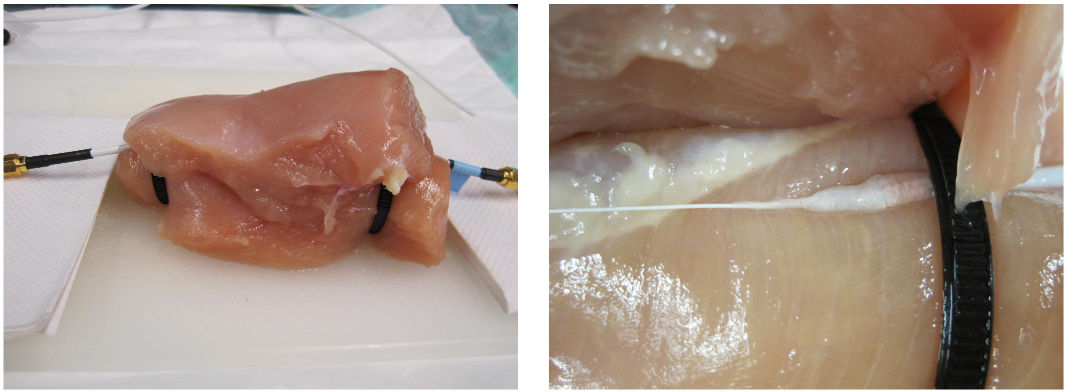

(a) AWG 36 SWTL embedded in raw chicken breast and characterized

(b) Closeup of AWG 36 SWTL “implanted” in raw chicken breast, showing launcher and parafilm wax seal

Figure 5.13: Experimental setup for testing SWTL’s in raw chicken breast, which functions as a tissue proxy for muscle

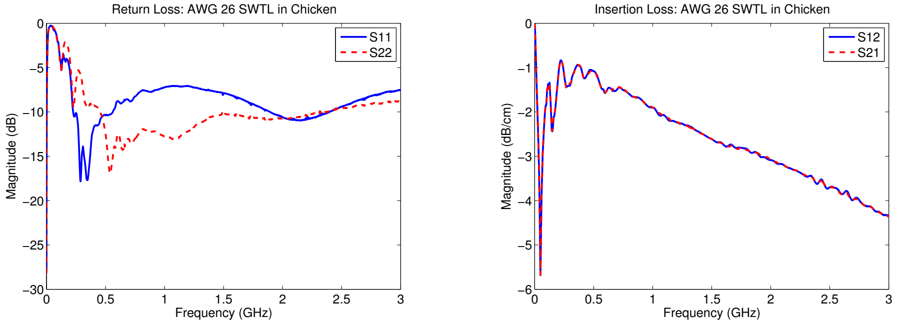

(a) Return Loss AWG 26 (b) Insertion Loss AWG 26

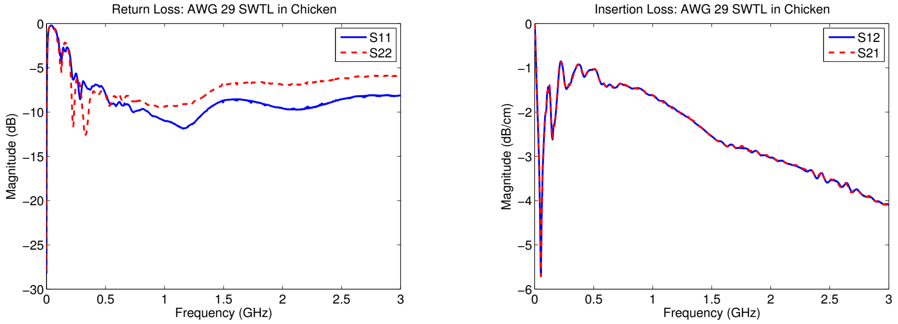

(c) Return Loss AWG 29 (d) Insertion Loss AWG 29

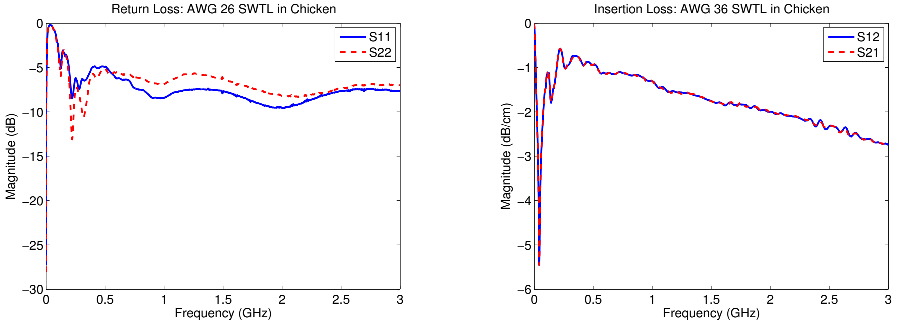

(e) Return Loss AWG 36 (f) Insertion Loss AWG 36

FIGURE 5.14: Single-wire transmission lines (SWTL's) tested inside raw chicken breast

for routing RF signals within living tissue, as well as increasing implantation depth, as near field coupling losses are greater in the same environment.

5.4.3 Bend Angle Measurements

The derived model for the SWTL in lossy dielectrics, as well as the measurements carried out for verification, assumed a perfectly straight transmission line with no bends or aberrations. Use of the SWTL in practical scenarios may force it to incur some degree of bend along its length. The robustness of the SWTL to bending is an important design consideration.

To explore the reaction of the SWTL to bend angle, the experiment shown in Figure 5.15. A rig holds the SWTL in place, while a swinging arm is used to achieve various bend angles for measurement. The bend angle was measured in increments from 0 (no bend) to 90 degrees.

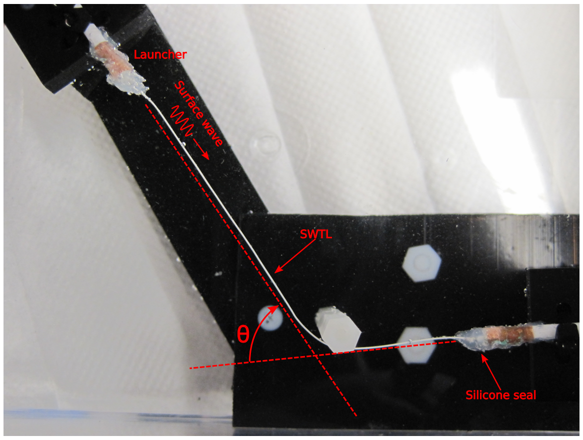

FIGURE 5.15: Experimental setup for investigating the effect of bend angle on the insertion loss of the SWTL

The return loss and insertion loss were measured for each wire tested (AWG 36, 29, and 26), providing insight into issues with matching and possible reflections. A full 2-port calibration was used on a vector network analyzer (VNA) to obtain these results.

For the thinnest wire, AWG 36, the bend angle was increased from 0 degrees to 90 degrees in increments of 15 degrees. The wire was again fully immersed in 0.91% saline. The return loss and insertion loss are shown in Figure 5.16.

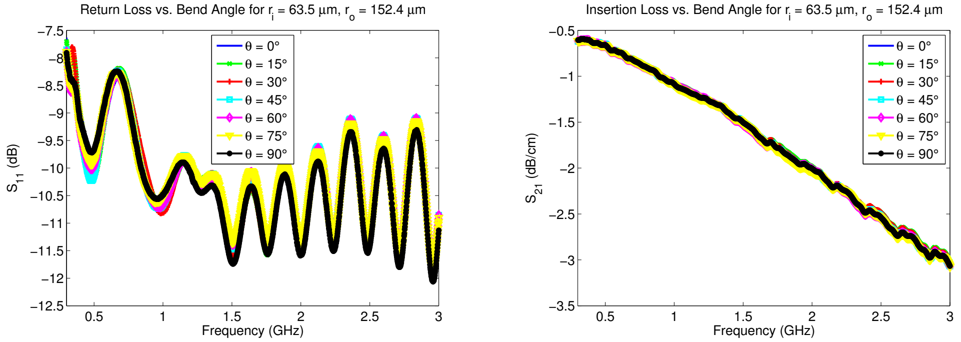

(a) (b)

FIGURE 5.16: Measured return loss in (a) and insertion loss in (b) of AWG 36 SWTL for various bend angles.

From a wide view of all frequencies tested, 300 MHz - 3 GHz, the bend angle has no discernible effect on matching and insertion loss. However, zooming in on the desired frequency operating range (902 - 928 MHz) reveals a slight adverse effect on the insertion loss, as shown in Figure 5.17.

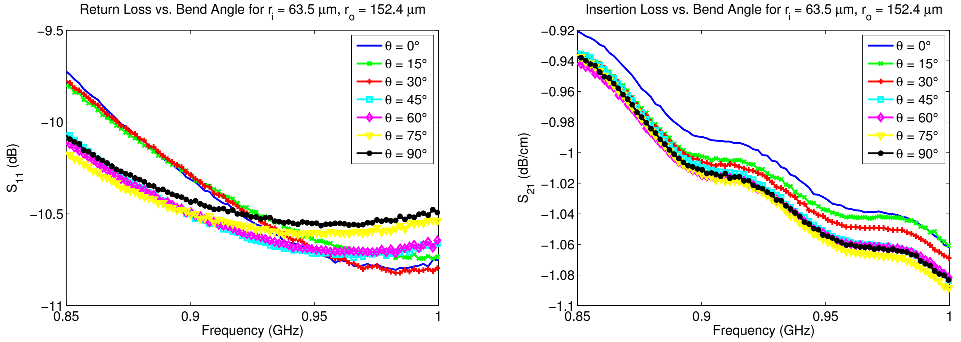

(a) (b)

FIGURE 5.17: Zoomed in return loss in (a) and insertion loss in (b) of AWG 36 SWTL for various bend angles.

When the bend angle is increased, the insertion loss of the AWG 36 SWTL increases slightly. However, while there is a clear trend in that an increased bend angle leads to an elevated insertion loss, the degree of the effect is minimal. In the worst case scenario, the insertion loss increases by about 0.05 dB/cm. For the return loss, the effect of the bend angle does match an apparent trend, but in the UHF ISM band, bend angle has no significant effect on return loss, and the matching remains practical.

For the AWG 29 SWTL, a similar adverse effect is seen on the insertion loss, as seen in Figure 5.18(a). The insertion loss appears directly proportional to the bend angle. Again, the degree to which the bend angle affects the insertion loss is minimal, and at 915 MHz, a worst case scenario bend of 90 degrees increases the insertion loss by approximately 0.06 dB/cm. Bend angle appears to have no significant effect on the return loss for the AWG 29 SWTL.

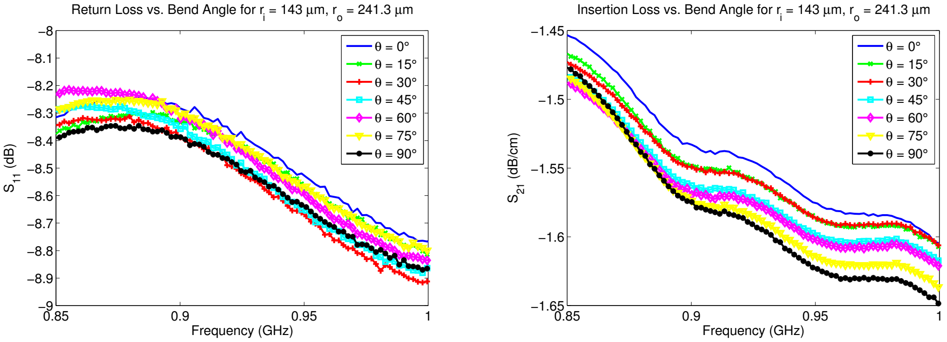

(a) (b)

FIGURE 5.18: Zoomed in return loss in (a) and insertion loss in (b) of AWG 29 SWTL for various bend angles.

For the thickest wire tested, AWG 26, the effect of bend angle on return loss and insertion loss is shown in Figure 5.19. Similarly to the two thinner wires tested, the bend angle adversely affects the insertion loss, and the loss increases as the bend angle approaches 90 degrees. The trend of insertion loss increasing with bend angle appears more direct as the bend angle approaches 90 degrees. At 915 MHz, the insertion loss increases by about 0.1 dB/cm, and around 1 GHz, the insertion loss increases by approximately 0.13 dB/cm, a more significant reaction to bend angle than the other wires tested.

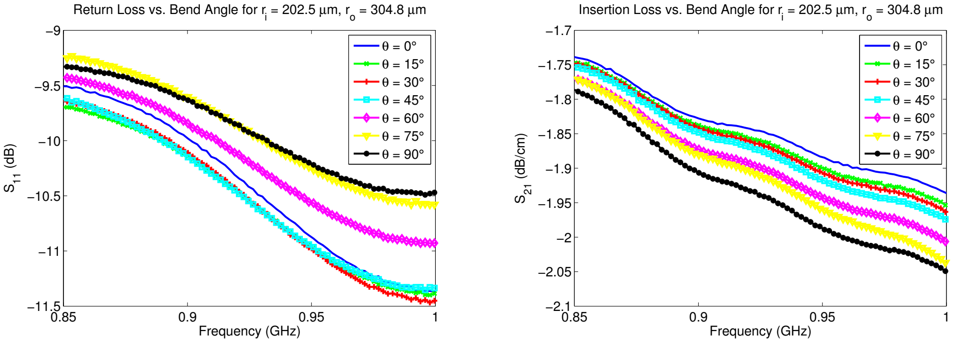

(a) (b)

FIGURE 5.19: Zoomed in return loss in (a) and insertion loss in (b) of AWG 29 SWTL for various bend angles.

The bend angle also has a more significant effect on the return loss of the AWG 26 SWTL. Around 1 GHz the largest deviation is seen, as the return loss drops from 11.2 dB to approximately 10.5 dB. However, in the UHF ISM band, the return loss deviation is no greater than approximately 0.8 dB. Even with the effect on the return loss, the AWG 26 SWTL is still matched well in the 0.91% saline in the desired operating band.

A comparison among the effect of the bend angle for all 3 wires tested is shown in Figure 5.20. The insertion loss of each wire versus bend angle is shown in 915 MHz, the desired operating frequency. The results are summarized in Table 5.4

The bend angle has a more adverse effect on the insertion loss for the thicker wires tested. As the thickness of the wire tested increased, the increase in insertion loss seen at each angle also increased. That is, the slope of the insertion loss versus angle increased with wire thickness.

The insertion loss, and the return loss to a degree, of an SWTL immersed in a lossy dielectric medium is robust to bend angle. The reason for this behavior stems from the large rate of radial decay of the emitted fields from the SWTL. As shown in Table 5.4, the theoretical radial decay for each of the wires tested is large,

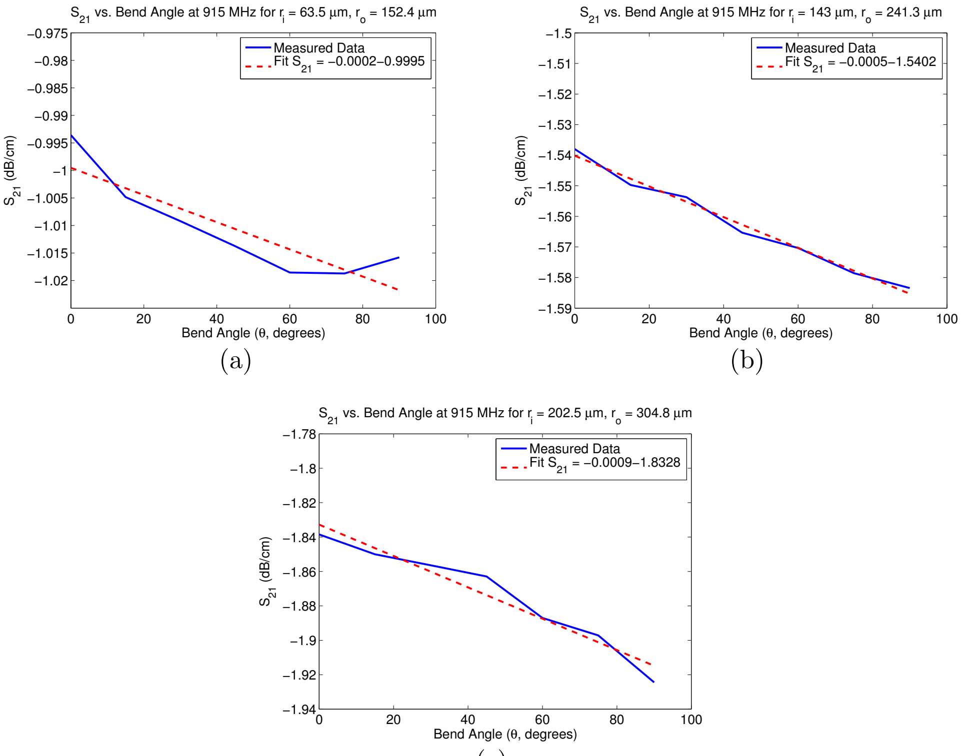

(a) (b)

(c)

FIGURE 5.20: Comparison of the effect of bend angle on insertion loss of all 3 wires tested (AWG 36, 29, 26). AWG 36 shown in (a), AWG 29 in (b), and AWG 26 in (c). A linear fit is shown for each wire.

indicating that the field extent outside the SWTL is minimal, and the surface wave is bound tightly to the surface of the transmission line. Approximately 95% of the power, in terms of both radiated losses and the surface wave, falls within 1 cm of the transmission line. Thus, upon bending of the SWTL, there will be less interaction of these fields until an extreme bend angle is reached.

Table 5.4: Measured Effect of Bend Angle from 0 to 90 Degrees on Insertion Loss of SWTL at 915 MHz

Wire Characteristics	Fitted Slope (dB/m·degree)
AWG 36	0.02
AWG 29	0.05
AWG 26	0.09

This can be compared to a SWTL in free space. The field extent for G-lines in free space is 10's of centimeters (depending on frequency of operation and wire parameters) [50]. The analysis of the effect of the bend radius on G-lines in free space was carried out in [56]. It was discovered that a bend angle of 90 degrees can produce an extra 25 dB of loss at 700 MHz. The G-line in free space is not as robust to bending as the SWTL in a lossy dielectric due to the difference in field extent, which is related to how tightly the surface wave is bound to the transmission line.

The SWTL presented here, for use in lossy dielectric media, is robust to bend angle, which would prove useful in a practical situation.

5.5 Comparison to Coaxial Cable

While the SWTL operates as an effective method of routing signals in lossy dielectrics when compared to near field coupling, a comparison to common transmission lines will reveal its utility.

Coaxial cables are an effective method of routing RF signals, and offer losses on the order of 0.1 dB/ft (0.003 dB/cm) at thicknesses of approximately 1 cm. Since coaxial cables are composed of a dielectric sandwiched between 2 conductors (and shielding) and the field is contained essentially entirely within the cable, the composition of the medium outside the cable has no discernible effect on the loss of the cable. This is a desirable behavior for a transmission line in a lossy dielectric, but would however displace large amounts of tissue if used in a practical scenario.

The derived SWTL model allows for transmission lines of very small thickness, and would displace little tissue. The matching and loss of a coaxial cable are dependent on its thickness, and very thin coaxial cables tend to exhibit high amounts of loss.

A thin coaxial cable available from Micro-Coax (www.micro-coax.com) exhibits the following parameters: diameter = 1.778 mm, and the loss at 900 MHz is 1.09

Table 5.5: Loss Comparison Between SWTL in 0.91% and Micro-coaxial Cable

	Radius (mm)	Loss (dB/cm)	Cross-sectional Area (mm^2)	Loss × Area (dB · cm)	Normalized
μ-coax	0.889	0.036	2.483	8.94×10^{-4}	1.22 dB/cm
SWTL	0.1524	1	0.0730	7.3×10^{-4}	1 dB/cm

dB/ft or 0.036 dB/cm. The thinnest SWTL tested in saline is 0.3048 mm in diameter, and exhibits a loss of approximately 1 dB/cm at 900 MHz. The SWTL in saline is far lossier than the thin coaxial cable, however, it is 5 times thinner. A comparison between the loss of the SWTL and the coaxial cable is shown in Table 5.5.

The cross-sectional area of the micro-coax is significantly larger than that of the SWTL. Using the metric of the transmission line loss multiplied by the cross-sectional area, resulting in units of dB x cm, takes the thickness of the transmission line into account along with the loss. Using this metric, the SWTL performs better than the micro-coax. The small cross-sectional area of the SWTL makes up for the increases loss over distance. Since the SWTL will be utilized over a short distance due to the nature of implantable devices operating in the near field, the larger loss values can be tolerated as the SWTL will displace very little tissue.

5.6 Conclusion

A theoretical model for a single-wire transmission line, or SWTL, immersed in a highly conductive dielectric material has been derived and verified through measurements. A SWTL will permit greater implantation depths, as well as a method for routing RF signals within living tissue, as using the SWTL as a type of lossy waveguide experiences less loss than near field coupling in a highly conductive dielectric material.

To further verify the use of the SWTL in a wireless implantable system employing UHF near field backscatter, the SWTL was integrated with a passive biotelemetry chip (described in Chapter 4) and characterized.

6

Integrating A SWTL And Passive Biotelemetry Device

6.1 Introduction

This chapter focuses on the integration of a SWTL with an existing passive biotelemetry chip [3] (chip described in chapter 4), and showing that it is possible to power up a passive biotelemetry device and reliably communicate with a SWTL immersed in a proxy for living tissue, acting as the intermediary between the implanted antenna and the biotelemetry device itself.

The integration of the SWTL and the biotelemetry chip is considered first in a cabled test setup to isolate the effects of the integration from that of the near field link. A signal is injected into the SWTL immersed in a tissue proxy (0.91% saline), sent to the biotelemetry device, and the return signal is then received through the SWTL. The near field link is then considered along with the integration of the SWTL and biotelemetry chip by integrating the internal loop antenna with the SWTL and telemetry device and including the octagonal segmented loop transmitting antenna to complete the link.

6.2 Experimental Results

To characterize the wireless biotelemetry device and SWTL integration, a transceiver was setup as shown in Figure 6.1.

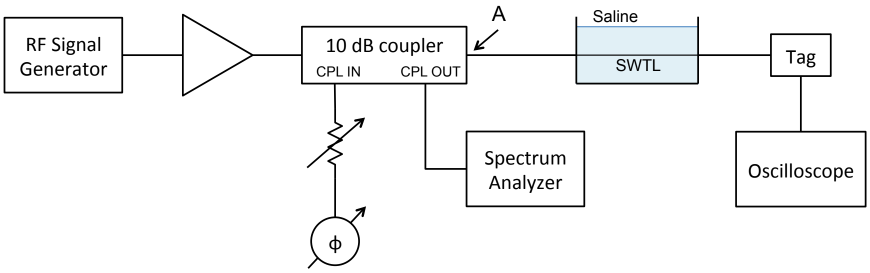

FIGURE 6.1: Experimental setup for characterizing the integration of the SWTL and wireless biotelemetry device

The RF signal generator creates the interrogation field for the biotelemetry device to use for power and communication, which is sent through the SWTL immersed in saline. The reflected signal from the tag is received through a 10 dB coupler, and sent to a spectrum analyzer to observe the backscatter envelope. An oscilloscope is connected directly to the tag's regulated and unregulated voltage pads to observe the harvested energy. All measurements were performed at a frequency of 915 MHz. Point "A" is where power levels are referred to, at the beginning of the SWTL cable assembly, which is 10 cm in all measurements conducted.

6.2.1 Harvested Energy

When powering the tag using the integrated SWTL, the harvested energy was observed on the oscilloscope. The harvested energy versus input power to the front end of the SWTL is shown in Figures 6.2(a) and 6.2(b).

In agreement with previous simulations and measurements, the thinnest wire tested, AWG 36, outperforms the both the AWG 26 and 29 wires in terms of harvested voltage. At every power tested, the digital telemetry IC is able to harvest the most

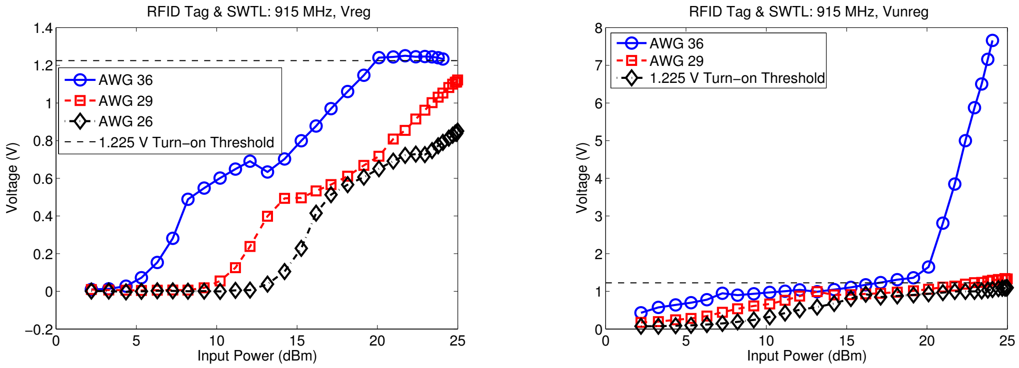

(a) Regulated harvested voltage on the telemetry IC

(b) Unregulated harvested voltage on the telemetry IC

Figure 6.2: Harvested voltage on digital telemetry IC integrated with 10 cm SWTL

voltage when integrated with the AWG 36 wire. Regulation is reached for an input power to the 10 cm SWTL at approximately +20 dBm, which corresponds to the necessary threshold for the IC of approximately +7 dBm at the input terminals to the chip after loss through the SWTL is accounted for. Using the AWG 26 and 29 wires, the digital telemetry IC never reaches regulation, but the unregulated harvested voltage appears to reach the threshold for communication around an input power of +23 dBm to the front end of the 10 cm SWTL. For the appropriate input power levels to the SWTL, the digital telemetry IC is able to harvest enough voltage for operation.

The ability of the digital telemetry IC to reliably communicate when integrated with a SWTL is another important factor that has been investigated. The backscatter envelope of the digital telemetry IC was characterized, and is shown below in Figure 6.3.

The data sidebands become visible for the AWG 36 wire at an input power to the 10 cm SWTL of approximately +15 dBm, 5 dB before the AWG 29 wire allows the chip to backscatter, and 8 dB before the sidebands become visible with the AWG 26 wire used as an SWTL. An example of the backscatter envelope, showing the data sidebands, for the turn-on point using the AWG 36 wire is shown in Figure 6.4. The

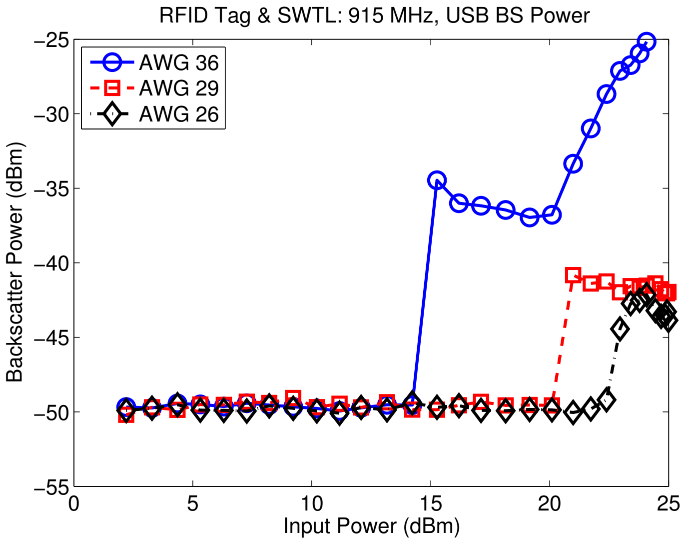

FIGURE 6.3: Backscatter power in the upper sideband (USB) of the digital telemetry IC integrated with a 10 cm SWTL. The input power is referred to the beginning of the 10 cm SWTL cable assembly.

power in the upper data sideband for the AWG 36 wire increases linearly from -36 dBm to -25 dBm, for an input power range of +20 dBm to +24 dBm. Not only do the AWG 29 and 26 SWTL's require a greater input power to reach the telemetry IC's turn-on threshold, but when this threshold is reached and the chip backscatters data to the receiver, the backscatter power is greatly reduced when compared to the telemetry IC integrated with the thinner AWG 36 SWTL.

For an input power at the terminals of the implanted (internal) antenna of +15 dBm, the implant depth of the telemetry IC can be increased from 1.5 cm, as shown in the previous section, to 10 cm, the length of the SWTL used here. The internal antenna can be placed close to the external antenna for high near field coupling efficiency without compromising implant depth, since implant depth is now decoupled from communication (antenna) distance by using the SWTL to connect the internal antenna to the telemetry device.

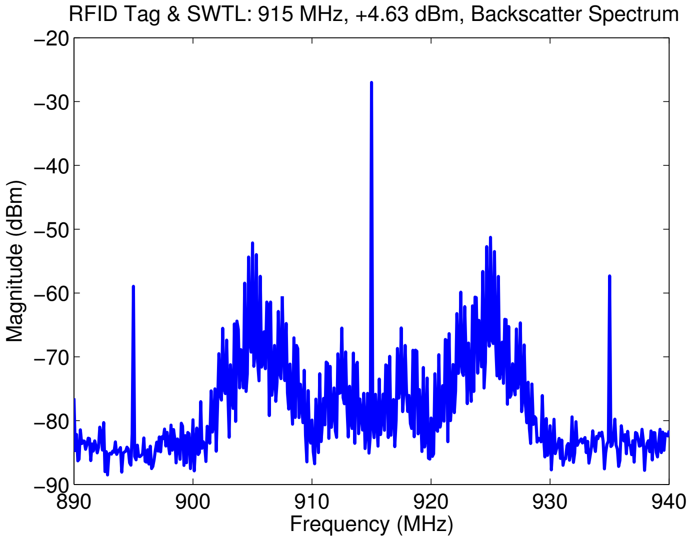

FIGURE 6.4: Backscatter spectrum for an input power of +15 dBm at the front end of the 10 cm SWTL immersed in 0.91% saline. The power at the terminals of the telemetry IC is +4.63 dBm.

6.2.2 Demodulated Data

In order for the integration of the SWTL and biotelemetry chip to function properly in the context of the system, the inclusion of the SWTL must not affect the demodulation of transmitted data. In order to verify the functionality of the SWTL in the system, the base station described in Chapter 4 was used to generate the interrogation signal for the small octagonal segmented loop antenna, as well as receive and demodulate the transmitted data.

The chip and integrated SWTL are shown in Figure 6.5. The entire assembly was immersed in 0.91% saline for testing, with the small loop antenna a distance of approximately 2 cm from the transmit antenna, placing it in the radiating near field for backscatter operation. The length of SWTL is 6 cm, extending the implant depth to potentially permit access to deeper tissue.

The same procedure outlined in Chapter 4 that was used to verify the preservation of spike timing for a near field backscatter system is employed here. The

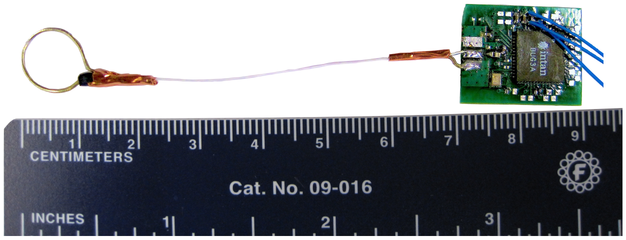

FIGURE 6.5: Biotelemetry chip, integrated SWTL with launchers, and small loop antenna used to verify functionality for integrating all system components.

chip extracted the necessary operating power from the interrogation field, incurring losses over the SWTL. Pre-recorded neural data was played back using an Agilent 33220A arbitrary waveform generator and injected into the biotelemetry chip, amplified, sampled, and communicated to the base station across the near field backscatter link. The demodulated data is shown in Figure 6.6.

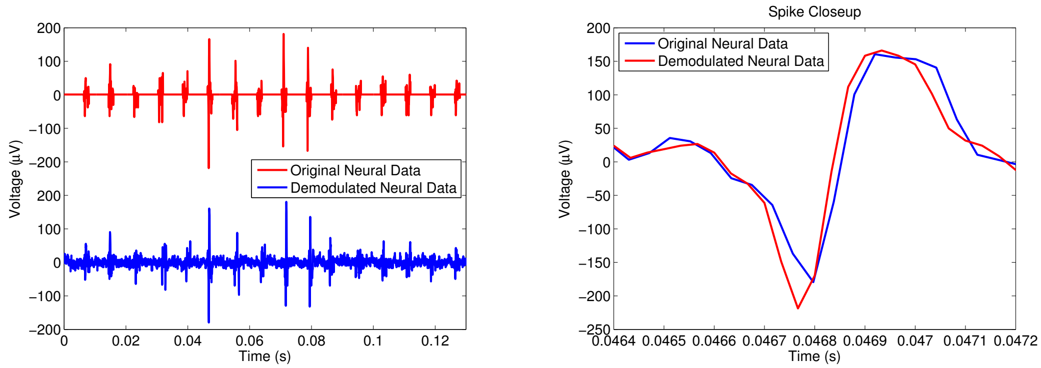

(a) (b)

FIGURE 6.6: Demodulated data over near field backscatter link using biotelemetry chip integrated with SWTL in 0.91% saline. In (a), a piece of the original and demodulated waveform. In (b), a closeup of a single neural spike. (Note: the data was aligned in post-processing).

A snippet of the demodulated data in Figure 6.6(a) shows that the neural spikes in the demodulated data line up with the original data. The amplitude of each neural spike is preserved in the communication system, although the demodulated data exhibits more noise. The demodulated data with the integrated SWTL exhibits more noise than that system without the SWTL, as the SWTL forces signals to travel greater distances in the saline, albeit tightly bound to the surface. The SWTL also has the ability to pick up any stray noise, as it acts in part like an inefficient antenna.

A closeup of one of the neural spikes in Figure 6.6(b), shows that the spike timing is essentially preserved, which is where the pertinent information lies when dealing with neural data. There is a slight discrepancy between the original and demodulated data, which is in part due to errors in the recovered clock by the base station. This can be fixed in post-processing, or by improved error-checking in the base station itself.

Integrating the SWTL with the biotelemetry chip allows for accurate telemetry of high-bandwidth neural data

6.3 Conlcusion

By utilizing the SWTL, we are able to decouple the implantation depth from the communication distance, the distance between the transmitting and receiving antennas. Instead of keeping the internal antenna close to the implant and relying on near field coupling over conductive and lossy tissue which will lead to a reduced implantation depth, the internal antenna can be kept in close proximity to the external antenna for high coupling efficiency while placing the telemetry IC and accompanying sensors deeper in tissue using a SWTL. The SWTL will provide for more efficient signal propagation in comparison to near field coupling, albeit at the expense of tissue displacement. However, it has been shown in theoretical and measured results that SWTL can be made thin without compromising loss characteristics to a great extent.

Additionally, the integration of a SWTL with a wireless implantable system provides a method for routing RF signals efficiently in living tissue, which can aid in handling multiple implant sites. Using conventional load modulation, multiple implant sites would each require their own external antenna for power and communication since the communication range is limited. By integrating a SWTL, RF signals can be routed within living tissue, connecting multiple implants, forming a network within living tissue and reducing the amount of external antennas required.

Integrating a SWTL with a wireless implantable communication system is a step towards a system with high data-rate, low-power communication and controllable implant depth, as well as the option to handle multiple implant sites without the need for multiple external antennas.

7

Conclusion

In this thesis, we propose two methods for improving communication with wireless implantable devices. This work addresses the shortcomings of conventional HF near field load modulation systems which do not support high data-rates, as well as those of systems employing on-chip radios which require large DC bias currents and consume large amounts of power. Utilizing a greater carrier frequency in the UHF ISM band of 915 MHz permits correspondingly greater signal bandwidths, which can be used for sensors that generate data in the 10's of Mbps, such as neural recording. While a carrier frequency of 915 MHz experiences greater loss over tissue than frequencies in the HF range, utilizing a UHF carrier permits smaller antenna designs and the ability to focus the incident field on the implant site, preventing extraneous absorption into adjacent tissue. To drive down the power consumption on the implant while still allowing for a large communication bandwidth, modulated backscatter in the near field allows for extremely low power dissipation at the implant. As demonstrated by the near field link characterization in terms of loss and backscatter shown in this work [57], in a forward link-limited situation, high data rate modulated backscatter in the near field is achievable for the appropriate receiver sensitivity. Moreover, this work has shown that high data rate communication in the near field in lossy tissue is possible with a fully passive telemetry IC, and that increased implantation depth can be achieved by routing RF signals in living tissue with a single-wire transmission line (SWTL). This work will aid in developing a chronic, high-data rate wireless biosignal acquisition system.

The original contributions of this work are summarized below.

7.1 Original Contributions

The accomplished original contributions are as follows:

- Demonstration of utilizing scattered fields in the radiating near field for active and passive wireless high-bandwidth communication with an implantable device in the UHF ISM band
- Analytic model and supporting measurements for a single-wire transmission line (SWTL) in highly conductive dielectric media
- Characterization of a wirelessly powered biotelemetry device integrated with a SWTL
- Measurement and characterization of an implantable device integrating a SWTL, antenna, and sensor; an end-to-end implantable biotelemetry system

7.1.1 Characterization Of An End-To-End Wirelessly Powered Biotelemetry System

This work has determined a solution towards a system implementation of a high data rate, low-power, implantable passive wireless biotelemetry system with controlled implant depth. Figure 7.1 shows a diagram of the proposed system. The complete end-to-end system has been demonstrated, characterized, and analyzed in a non-living system, using raw chicken and saline as tissue proxies.

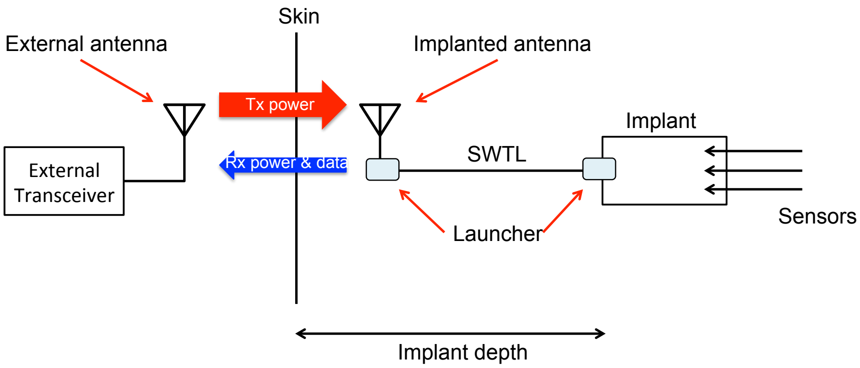

FIGURE 7.1: Diagram of the full, end-to-end wireless implantable system showing external antenna and receiver, internal antenna, SWTL with launchers, and implantable IC.

The system proposed in this work that is able to achieve high data rates at mW power budgets as well as controlled implant depth for a wirelessly implantable telemetry device would be beneficial in the field of animal behavioral studies, in the study of brain machine interfaces (BMI's), and in the investigation of improving limb function after spinal cord injuries [58].

7.2 Future Work

7.2.1 Antenna Design

It has been made clear in this thesis that antenna design, in the both the transmitter and transponder, is critical when designing wireless biotelemetry systems. A design for an external antenna that generates a strong magnetic field while keeping the electric field to a minimum to prevent reaching SAR limits has been presented in this work.

The internal antenna used in this work is a small loop antenna. Small loop antennas have been shown to be poor radiators in free space, but since SNR is a more important factor in receiving applications, small loops serve well as receivers [29]. Improving the design of the internal antenna as both a radiator and a receiver would greatly benefit the overall efficiency of the demonstrated system.

Much work has been done on various types of implantable antennas ([59, 60, 61]), and it continues to be an active area of research. Investigation into internal antenna improvements such as increasing the number of turns and the effect that would have on the resonance of the internal system, the efficiency, and the matching with the integrated SWTL, would lead towards designing a better internal antenna.

7.2.2 Launcher Design

While it has been shown that the designed quarter-wave sleeve balun acts as a launcher and is able to transform signals to and from surface wave modes on the SWTL, the design has not been optimized. A more efficient launcher design would aid in matching to the antenna and biotelemetry chip, and would result in less power loss in surrounding tissue (which can potentially cause tissue heating problems), as well as a more efficient link.

A simulation of the surface currents that exist on the launcher, as well as the emitted and static fields, would grant insight into potential design improvements. One obvious issue with the current launcher design is its size, it is a bulky design for an implantable device. The size of the launchers used for single-wire transmission lines are proportional to the field extent around the transmission line, so that they are able to capture the most energy for maximum efficiency. Due to the tightly bound surface waves demonstrated for a SWTL in a lossy dielectric and the small field extent, the size of the launcher can be made similarly small without compromising a great deal of efficiency. It has been shown in [62] that planar excitation of a single-wire transmission line is possible at THz frequencies, and can be used in BioMEMs technology. A printed launcher and SWTL will allow for a more compact implantable device. Moreover, the planar transmission line and launcher can be made to be resistant to movement through rigidity, preventing increased losses due to bending.

The design of a launcher in this manner is similar to co-planar waveguide, and can be easily incorporated into the current design. Placing co-planar waveguide on a biocompatible flexible substrate will vastly shrink the size and complexity of the implantable device. Additionally, many integrated circuits use co-planar waveguide as a means for routing signals, and some of this existing infrastructure in a potential biotelemetry chip (such as the chip presented in this work) can be taken advantage of.

7.2.3 Sensing Electrodes as Transmission Lines

Many currently existing biotelemetry systems utilize microelectrodes as sensing devices for capturing biological signals, such as neurological data. These electrodes are often composed of very thin "microwires," and are often in close proximity to the implantable system they are providing sensing capabilities for.

Using the theory developed in this work for utilizing a SWTL in a lossy dielectric media, these sensing electrodes can potentially be used as transmission lines, aiding to improve the efficiency of the existing wireless link. Providing a secondary function in terms of communication for the sensing electrodes has not yet been explored in the literature, and offers a promising avenue for improving currently existing biotelemetry systems by taking advantage of their existing infrastructure. It would need to be investigated as to whether or not the commonly used sensing electrodes would support a surface wave mode, and if it is possible to utilize them as transmission lines while sensing data, in a multiplexed fashion.

Conversely, while it is possible that sensing electrodes can be used as transmission lines, there is the potential for transmission lines to act as sensing devices. Since the surface wave is so tightly bound to the SWTL and the radiated field extent does not extend far, a SWTL will only be able to detect activity that occurs nearby. The single-wire transmission lines act as inefficient antennas, and have the potential to detect electric or magnetic fields along their length. This would provide an extra means for sensing in biotelemetry devices, and opens the door for potential implantable body networks that are able to sense and communicate simultaneously using a simple topology.

Appendix A

Radiation Zone Model

A.1 Radiation Zone Models

The inclusion of $\frac{1}{r^3}$, $\frac{1}{r^2}$, and $\frac{1}{r}$ terms in the emitted fields of the electric and magnetic dipole antennas suggests the existence of three distinct radiation zones surrounding the antennas, where a singular term, and thus decay rate of the emitted fields, is dominant in each region. However, depending on the frequency and corresponding electrical size of the antenna, the size of the radiation zone where the $\frac{1}{r^2}$ term is alone dominant can shrink to a nearly negligible size [63]. In this scenario, the radiation zones closest to the antenna, where the $\frac{1}{r^3}$ and $\frac{1}{r^2}$ terms are dominant, are grouped together, resulting in a two-region model – the near field and far field.

Figure A.1 shows the common terminology used in describing the radiation zones surrounding an antenna for both the two and three-region models. There are many interchangeable terms that are used to describe each radiation zone. The existence of two separate models as well as a large number of radiation zone descriptors portrays the complexity in differentiating the near field from the far field.

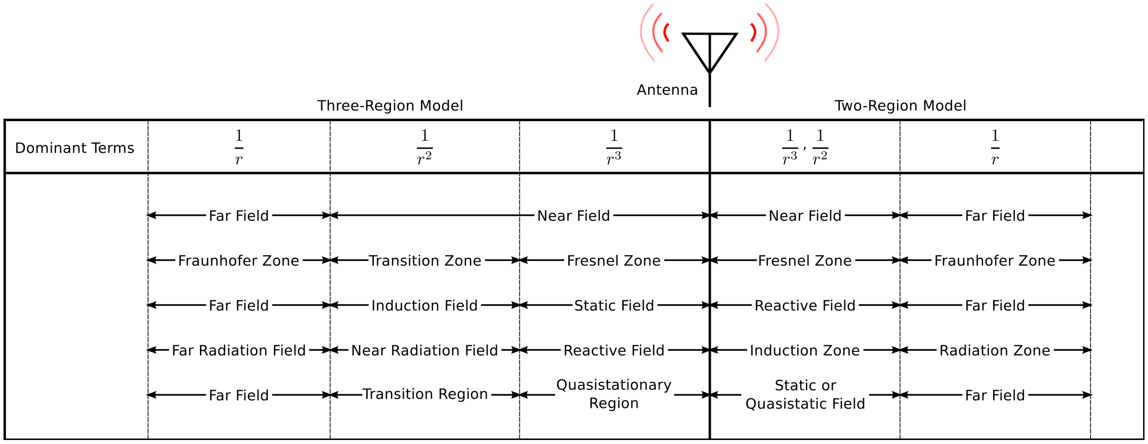

FIGURE A.1: Terminology used to describe the radiation zones surrounding an antenna for both the two and three-region model. The dominant terms in each zone are also shown (Adapted from [64]).

A.1.1 Antenna Electrical Size

In order to distinguish the two and three region model views of the radiation zones of an antenna, the electrical size of an antenna must be established, as well as the definition of electrically small and large antennas.

An antenna can be classified as being either electrically small or electrically large. The electrical size of an antenna is expressed as its physical size defined relative to the operating wavelength, where the physical size is defined by the largest dimension of the antenna, D [65, 66, 29]. The electrical size of an antenna is typically different than its physical size, as the electrical size expresses the physical size in terms of number of wavelengths, which is a frequency and dielectric medium dependent quantity.

Generally speaking, antennas that are electrically small have a physical size that is small relative to the operating wavelength, and those that are electrically large have a physical size that is large compared to the operating wavelength. A rigorous definition for electrically small antennas was developed by Wheeler in 1947, the first work to address the fundamental limits of electrically small antennas [67]. In this work, Wheeler defined an electrically small antenna as follows:

$$ka' < 1 \tag{A.1}$$

where k is the wavenumber and is equivalent to $\frac{2\pi}{\lambda}$ (radians/meter), λ is the wavelength in meters, and a' is the radius of a sphere that encloses the maximum dimension of the antenna, expressed in meters.

If the maximum dimension of the antenna is defined as D, where D is measured from the antenna's phase center, the definition of an electrically small antenna can be simplified to obtain:

$$D < \frac{\lambda}{\pi} \tag{A.2}$$

That is, an antenna is defined to be electrically small if its maximum dimension is approximately less than one-third of the propagating wavelength. Consequently, an antenna whose maximum dimension is approximately larger than one-third of the wavelength is classified as an electrically large antenna.

However, there are various rules of thumb for the criteria required for an antenna to be classified as electrically small in addition to that developed by Wheeler. The most common definition is that the largest dimension of the antenna must not exceed one-tenth of a wavelength [68, 69]. In other words:

$$D < \frac{\lambda}{10} \tag{A.3}$$

Therefore, according to this criteria, a dipole must have a length of less than one-tenth of a wavelength, a loop must have a diameter less than one-tenth of a wavelength, and a patch antenna must have a diagonal dimension less than one-tenth of a wavelength. The wavelength considered is the guided wavelength in the medium surrounding the antenna. Antennas that do not meet this criteria are considered electrically large.

While this rule of thumb is useful in prototyping antennas, accurately determining the classification of an antenna as electrically small or electrically large can be performed through simulation, or through careful measurement of the emitted fields of the antenna. Electrically small and electrically large antennas exhibit different field distributions, as explained below.

This section has defined the characteristics for electrically large and small antennas, without delving into the fundamental limits in terms of bandwidth and efficiency of each class of antenna. A rigorous definition of electrically large and small antennas is needed to distinguish the two models for the radiation zones surrounding an antenna, as these antennas operate differently in terms of radiated and static fields, and current distribution, as discussed below. For further information about the fundamental limits of electrically large and small antennas, see [29, 70, 71, 68].

A.1.2 Two-Region Model

For electrically small antennas, the radiation zone where the $\frac{1}{r^2}$ term is dominant, typically called the radiating near field as seen in Figure A.1, is minimal if it exists at all. The reason for the limited size of the radiating near field for electrically small antennas is a combination of the fundamental limits on the radiation efficiency, gain, current distribution, and bandwidth limitations [71, 68].

The radiation characteristics of electrically small antennas can therefore be accurately described by two regions, since the radiating sub-region of the near field can be neglected. The regions where the $\frac{1}{r^3}$ and $\frac{1}{r^2}$ terms are dominant are grouped together, resulting in a model with only two regions, the reactive near field and the far field.

Since the radiating near field for electrically small antennas can be neglected, only evanescent wave modes exist in the reactive near field zone. Propagating modes only exist in the far field. Thus, communication with electrically small antennas can only be performed by coupling in the near field, but in the far field, communication can be performed via scattered fields.

A.1.3 Three-Region Model

For electrically large antennas, the radiating near field where the $\frac{1}{r^2}$ term is dominant, cannot be neglected, and therefore these antennas require a three region model to accurately describe the emitted and static fields. This region where the $\frac{1}{r^2}$ term is dominant is often referred to as the transition between the near field where the $\frac{1}{r^3}$ term is dominant, and the far field where the $\frac{1}{r}$ term is dominant. In this region, the emitted fields from the antenna are transitioning into far field waves, but have distinct characteristics from the static fields in the $\frac{1}{r^3}$ dominant region, and the propagating waves in the $\frac{1}{r}$ dominant region.

While this transition zone is located between the static fields in the near field where the $\frac{1}{r^3}$ term dominates and the propagating waves in the far field where the $\frac{1}{r}$ term dominates, it is considered part of the near field. Therefore, for electrically large antennas which require a three-region model to accurately describe the emitted and static fields, the near field can be broken down into two sub-regions, the reactive near field, where the fields are static and the $\frac{1}{r^3}$ term dominates, and the radiating near field, where propagating waves exist distinct from those in the far field and the $\frac{1}{r^2}$ term dominates. The nomenclature for these radiation zones varies, as shown in Figure A.1.

Communication with an electrically large antenna can be performed by coupling in the reactive near field, and by scattered fields in the far field, similar to an electrically small antenna. However, with the existence of a radiating near field of non-negligible size, scattering can also be performed in the radiating near field. This mode of communication in the radiating near field is beneficial as there is more power available in the near field, with the added potential to more easily focus this power on a receiving element.

A.2 Far Field

Far field radiation is well understood, and is the mode used in many standard applications. Radiation in the far field occurs only in a radial direction, with the E and H fields mutually perpendicular, unlike their complicated relationship in the near field. The strength of each components falls off as $1/r$, with the power density falling off as $1/r^2$.

Unlike the near field, the absorption of energy in the far field has no direct effect on the transmitter. The transmitter will draw constant power whether or not the energy in the far field is absorbed, whereas in the near field, a greater power draw on the transmitter will be seen if the energy available in the near field is absorbed. That is to say, the radiation in the near field does not extend out to infinity due to the more rapid fall-off in signal strength and power density. The power available close to the antenna in the near field may be quite large, but this will not extend to great distances like the energy in the far field.

A.3 Near Field

A.3.1 Reactive Near Field

The reactive near field is the region that is closest to the antenna. Here, the relation between the E and H fields is complicated, thus finding the true power density analytically is prohibitively complex. The EM waves in this region are not only being radiated out into space, but they possess a reactive component, making the fields sensitive to EM absorption by nearby conductors, unlike far field signals.

If the energy in this zone is not absorbed, it is held close to the antenna. This energy is traded between the antenna and the fields in a regenerative manner, so the energy is not lost. However, if any of this energy is absorbed by a nearby conductor, it is not sent back to the antenna and is lost. This is seen as an extra drain on the transmitter side since the energy is not returned. This is manifested by a different antenna impedance seen by the transmitter.

Finally, due to the complicated nature of the E and H fields in this zone, the power density does not follow the well-known inverse-square law as it does in the far field. Thus, even small decreases in distance near the antenna can result in drastic increases in the power density, making this zone potentially unsafe for both humans and equipment.

A.3.2 Radiating Near Field

In contrast to the reactive near field, the radiating near field, also called the Fresnel region, contains no reactive components. Fields in this zone are too far, based again on antenna size and wavelength, from the antenna for any back-coupled fields to be in-phase with the antenna signal and thus cannot efficiently store or replace energy from the antenna. All the energy in this zone is radiant energy.

However, the angular field distribution between the E and H fields depends on distance, unlike the far field relationship between these components. While this field relationship can become more predictable further in the radiating near field, it is generally still complicated. Moreover, the radiating zone, being a part of the near field, is still subject to unanticipated effects. Metal objects in this region can act as antennas and re-radiate some of the field energy, creating both a new surface to consider, and a new antenna which in turn generates its own radiation zones.

A.4 Zone Boundaries

The boundaries of the radiation zones surrounding an antenna are critical factors in communication systems. Where the near field ends and the far field begins can affect communication distance, as well as placement of a receiving or transmitting antenna.

Due to the complex nature of the near field zones, defining a rigid boundary for the radiation zones of an antenna is not a straightforward manner.

Since the boundary between the near field and the far field occurs when the $\frac{1}{r^3}$ and $\frac{1}{r^2}$ terms decay and the $\frac{1}{r}$ begins dominating, one of the most commonly cited definitions stems from equating the magnitude of the first two terms in Equation 2.3 [64]:

$$\frac{1}{kr} = \frac{1}{(kr)^2} \tag{A.4}$$

employing some algebra and using the fact that $k = \frac{2\pi}{\lambda}$, we find that:

$$r = \frac{\lambda}{2\pi} \tag{A.5}$$

This particular definition of the boundary between the near field and the far field of an antenna is a function of wavelength. This implies that the distance of the boundary from the antenna is inversely proportional to frequency, thus the boundary moves closer to the antenna as the frequency increases, shrinking the near field zones, and moves further away from the antenna as the frequency decreases, causing the near field zone to increase in size.

However, while this particular definition of the boundary between the near field and the far field provides a rule of thumb when designing certain systems, it ignores the electrical size of the antenna, especially the limitations on electrically small antennas [71, 68], as well as the phase, amplitude, and impedance characteristics of the surrounding field.

Owing to the complex nature of the field configuration in the near field coupled with the design criteria for a given system, the definition of the boundary between the near and far field takes different forms, as shown in Table A.1.

Table A.1: Definitions of the Near Field/Far Field Boundary in the Literature (Adapted from [64])

Shielding Criteria	Comments	Reference(s)
$\lambda/2\pi$	$1/r$ terms dominant	[72, 73]
$5\lambda/2\pi$	Wave impedance = 377 Ω	[74]
Antenna Criteria		
$\lambda/2\pi$	$1/r$ terms dominant	[29]
3λ	D not >> λ	[73, 75]
$\lambda/16$	Measurement error < 0.1 dB	[73, 76]
$\lambda/8$	Measurement error < 0.3 dB	[73, 76]
$\lambda/4$	Measurement error < 1 dB	[73, 76]
$\lambda/2\pi$	Satisfies the Rayleigh criteria	[77]
$\lambda/2\pi$	Electrically small antennas (D << λ)	[73, 63, 78, 79]
$0.62\sqrt{\frac{D^3}{\lambda}}$	Electrically large antennas (D >> λ) reactive zone boundary	[78, 63]
$2D^2/\lambda$	Electrically large antennas (D >> λ) radiating zone boundary	[73, 63, 78]
$3\lambda/16$	For dipoles	[73]

The variety of definitions for the boundary between the near and far field stem from considering different aspects of the fields – wave impedance, phase, amplitude – and how those characteristics vary with distance.

A.4.1 Wave Impedance

One way to determine the end of the near field and the beginning of the far field is to consider the wave impedance. The wave impedance of an EM wave is equal to the ratio of the transverse components of the electric and magnetic fields. For a transverse electromagnetic (TEM) plane wave in a homogeneous medium, the wave impedance is everywhere equivalent to the intrinsic impedance of the medium. The intrinsic impedance of a given homogenous medium is defined as:

$$\eta = \sqrt{\frac{j\omega\mu}{\sigma_e + j\omega\epsilon'}} \tag{A.6}$$

As plane waves are a far field phenomenon, the wave impedance of an EM wave in the near field is not equivalent to the medium's intrinsic impedance as a consequence of the interactions between the electric and magnetic fields. In the near field, the wave impedance fluctuates with distance before better approximating a plane wave and approaching the intrinsic impedance of the medium. Thus, the boundary between the near field and the far field can be obtained by determining where the wave impedance of the emitted fields approaches a constant value[1]. This definition of the boundary between the near field and the far field is of particular use to shield designers, as the effectiveness of a shield depends on the ratio of the shield's impedance to that of the incident wave.

Using the aforementioned field equations from an electric and magnetic dipole, the wave impedance of an electric dipole is computed by the ratio of Equation 2.1 and 2.2 as follows:

$$Z_E(r) = \left|\frac{E_\theta}{H_\phi}\right| = \left|\eta\left[\frac{\frac{1}{kr} + \frac{-j}{(kr)^2} + \frac{-1}{(kr)^3}}{\frac{1}{kr} + \frac{-j}{(kr)^2}}\right]\right| \tag{A.7}$$

$$= \left|\eta\left[\frac{1 + \frac{1}{jkr} + \frac{1}{(jkr)^2}}{1 + \frac{1}{jkr}}\right]\right| \tag{A.8}$$

Similarly, the wave impedance for a magnetic dipole can be computed from the ratio of Equations 2.4 and 2.6:

$$Z_H(r) = \left|\frac{E_\phi}{H_\theta}\right| = \left|-\eta\left[\frac{\frac{1}{kr} + \frac{-j}{(kr)^2}}{\frac{1}{kr} + \frac{-j}{(kr)^2} + \frac{-1}{(kr)^3}}\right]\right| \tag{A.9}$$

$$= \left|-\eta\left[\frac{1 + \frac{1}{jkr}}{1 + \frac{1}{jkr} + \frac{1}{(jkr)^2}}\right]\right| \tag{A.10}$$

---

[1] Theoretically, the wave impedance never reaches a constant, but becomes asymptotic to a value over distance. In free space, for example, the wave impedance of a plane TEM wave is asymptotic to $\sqrt{\frac{\mu_0}{\epsilon_0}} \approx 377\Omega$

It's clear from equations A.7 and A.9 that $\lim_{r\to+\infty} Z_E(r) = \lim_{r\to+\infty} Z_H(r) = \eta$, which implies that a plane TEM wave's impedance is everywhere equivalent to the intrinsic impedance of the medium since the wave will be in the far field as r approaches infinity. Observing the fluctuation of the wave's impedance over distance as it approaches the far field reveals the near field to far field transition from the perspective of wave impedance.

Using Equations A.7 and A.9, we can plot the impedance of the emitted wave from the electric and magnetic dipoles to determine where the impedance begins to approach a constant value, thus determining the beginning of the far field from the wave impedance perspective. Figure A.2 shows the wave impedance in free space as a function of range and wavenumber. Using equation A.6, the intrinsic impedance of free space, where $\sigma_e \approx 0$, is:

$$\eta = \sqrt{\frac{\mu_0}{\epsilon_0}} \approx 120\pi\,\Omega \approx 377\,\Omega \tag{A.11}$$

The distance at which the intrinsic impedance of free space starts to become constant is approximately $r = \frac{5\lambda}{2\pi}$, as labeled on Figure A.2. This distance is considered the boundary between the near field and far field for shield designers (Table A.1). The distance often cited as the boundary between the near field and far field, $\frac{\lambda}{2\pi}$, is approximately the location of a local maximum for the wave impedance of the magnetic dipole, and a local minimum for the wave impedance of the electric dipole.

A more thorough method of describing the variation in wave impedance involves separating the wave impedance into three regions, corresponding to the reactive near field, the radiating near field (or transition region), and the far field. The shape of the wave impedance versus range and wavenumber can be naturally separated into three regions – the region preceding the local minimum or maximum, the region containing the local minimum or maximum, and the region succeeding the local minimum or

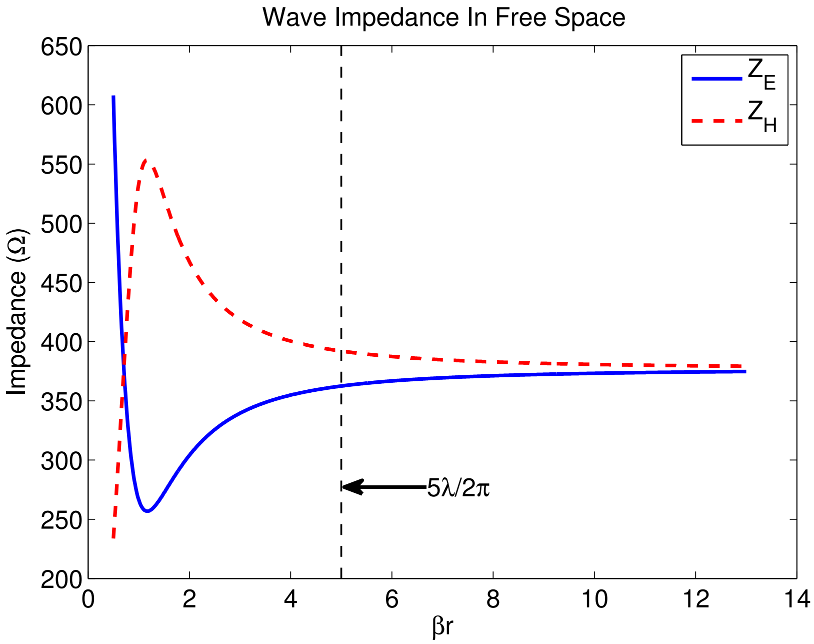

FIGURE A.2: Wave impedance of the electric and magnetic dipoles in free space as a function of range and wavenumber

maximum, where the wave impedance begins to asymptotically approach a constant value.

Separating the wave impedance into three regions, the reactive near field is the region before the local minimum or maximum where:

$$r < 0.8\frac{\lambda}{2\pi} \tag{A.12}$$

The radiating near field, or the transition region, occurs where the local maximum or minimum exists:

$$0.8\frac{\lambda}{2\pi} < r < 2.4\frac{\lambda}{2\pi} \tag{A.13}$$

And finally, the far field is the region where the wave impedance begins to asymptotically approach a constant value, for:

$$r > 2.4\frac{\lambda}{2\pi} \tag{A.14}$$

These definitions of the boundaries between the regions of the near field and the far field are based upon the wave impedance of the emitted signal, and are most useful in designing shielding. These boundaries do not take the wave amplitude, phase, or shape into account, and represent a single criteria in defining the boundaries between the radiation zones of an antenna. The following sections derive the radiation zone boundaries considering the antenna parameters and the wave phase front.

A.4.2 Antenna Parameters

The boundaries for the near and far field may be determined by considering the geometry of an antenna, as well as the emanating phase front. Figure A.3 shows the geometry of a transmitting antenna of length l, oriented along the z-axis, when the receiving antenna is close to the transmitter as in Figure A.3(a), and far away from the transmitter as in Figure A.3(b).

Figure A.3 shows two lines emanating from each antenna, r and r'. The line labeled r traces a path from a point on the antenna to a point in space, P. The line labeled r' traverses a path from the midpoint of the antenna to the same point in space. Along line r', the radiation zones of the antenna exist, and at certain distances, the reactive near field ends and the radiating near field begins, after which the radiating near field will end and the far field begins.

Based on the geometry shown in Figure A.3, line r' is longer than r. The law of cosines states that the following relationship exists between r' and r:

$$r' = \sqrt{r^2 + z^2 - 2zr\cos(\theta)} \tag{A.15}$$

Assuming that point P is very far away from the transmitting antenna as shown

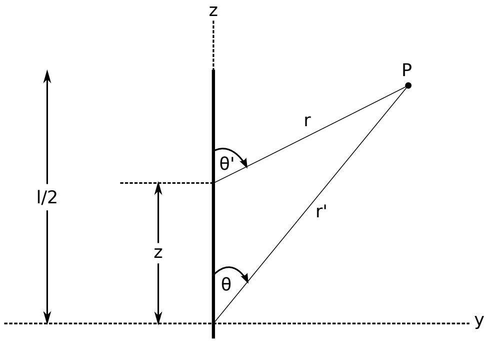

(a) Receiver close to transmitting antenna

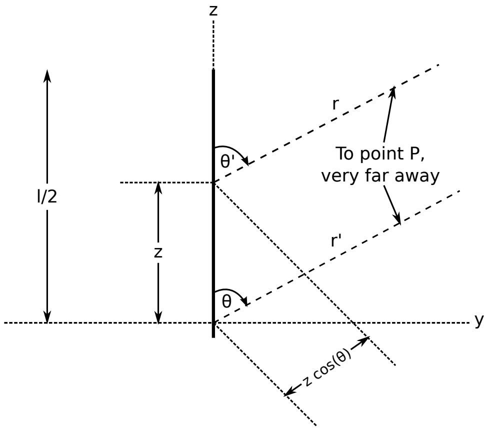

(b) Receiver far away from transmitting antenna

FIGURE A.3: Geometry of an antenna and receiver for determining near and far field boundaries

in Figure A.3(b), the receiver is in the far field, the lines r and r' become parallel, and $r >> z$ such that equation A.15 can be simplified as follows:

$$r' = \sqrt{r^2 - 2zr\cos(\theta)} \tag{A.16}$$

Applying the binomial theorem to equation A.16 results in the following expansion:

$$r' = r - z\cos(\theta) - \frac{1}{r}\frac{z^2\cos^2(\theta)}{2} - \frac{1}{r^2}\frac{z^3\cos^3(\theta)}{2} - \cdots \tag{A.17}$$

While the binomial expansion is in theory an infinite series, for practical use it can be truncated to any number of finite terms for a desired accuracy. The expansion for

r' in equation A.17 can be truncated after the second term, resulting in the following error:

$$\text{Error} = \frac{1}{r}\frac{z^2\cos^2(\theta)}{2} \tag{A.18}$$

This error is maximized when $\theta = \frac{\pi}{2}$, such that:

$$\max(\text{Error}) = \frac{z^2}{2r}, \quad \theta = \frac{\pi}{2} \tag{A.19}$$

By ignoring the terms beyond the second term in equation A.17, the error in equation A.19 must be taken into consideration when determining the boundaries of the radiation zones surrounding the antenna. It has been shown that the amplitude of a radiated wave has minimal effect on measurement error, but the phase has a significant impact [29, 80, 81]. As distance and phase are directly related for radio waves, the error in the distance the far field begins is critical. For acceptable errors in antenna measurements, phase differences with a maximum value of $\pi/8$ are tolerable. Therefore, the error in the distance measurement coupled with the wavenumber has a maximum value as follows:

$$\frac{\beta z^2}{2r} \leqslant \frac{\pi}{8} \tag{A.20}$$

Thus:

$$r \cong \frac{2z^2}{\lambda} = \frac{2D^2}{\lambda} \tag{A.21}$$

for $z = D$, the maximum length of the antenna.

For a tolerable phase measurement error, which translates to a distance measurement error, the far field begins at a distance of $\frac{2D^2}{\lambda}$.

A wave emanating from the center of the antenna must travel an additional distance of $z\cos(\theta)$ to point P when compared to a wave from z, which travels $r = r' - z\cos(\theta)$. The extra distance traveled causes the wave from the center of the antenna to arrive at point P attenuated and with a phase shift when compared to the wave from z.

The far field effects can be reflected in the equations for the fields generated by the antenna by taking the computed path differences into account. For an electric dipole, the electric field generated in the radial direction, equation 2.3, can be rewritten to take the far field effects into account:

$$E_r = \frac{ID\beta^2}{4\pi\omega\epsilon_0}\left[\frac{j}{r}\right]e^{-j\beta(r'-z\cos(\theta))} \tag{A.22}$$

The r^2 and r^3 terms are omitted as those terms are insignificant in the far field, and the $r' - z\cos(\theta)$ term in the denominator reduces to r since $r \sim r'$ in the far field. In this manner, the attenuation effects of waves emanating from different areas of the antenna are accounted for. The phase effects are accounted for by modifying the exponential phase term as shown in equation A.22 by $r' - z\cos(\theta)$. This term cannot be simplified further, as small changes in distance can significantly affect the phase term.

The boundary between the near field and the far field by taking the antenna parameters into account has been determined by the amount of error that measurement can tolerate. The amount of tolerable error can be changed, which would then be reflected in the near field/far field boundary in equations A.20 and A.21. A similar method for determining the near field/far field boundary involves considering the wave front of the emanating fields.

A.4.3 Phase Wavefront

The boundary between the near field and the far field can also be determined from the perspective of the wavefronts emanating from an antenna. When electromagnetic waves are in the far field, it is often assumed that they take on the form of plane waves. A plane wave contains wavefronts, or surfaces of constant phase, that are parallel planes. In practice, the existence of a plane wave is physically impossible as only a plane wave of infinite extent will propagate as such, however, many types of waves are approximately plane waves in localized regions of space.

From a localized radiation source, such as an antenna, a field is produced that is approximately a plane wave far away from the antenna, in its far field zone. From the viewpoint of the phase wavefront of emanated waves from an antenna, it is thus possible to determine the near field/far field boundary to a desired degree of accuracy as the distance at which the emanated waves are approximately plane waves.

Figure A.4 shows the wavefronts emanating from transmit antennas, and their gradual transition to plane waves.

There are two antennas on the z-axis, perpendicular to the plane wavefront in Figure A.4. The circles surrounding the antennas represent the emanating waves from each antenna. The wavefront created by Antenna 1 better approximates a plane wave than does the wavefront created by Antenna 2. As the distance between a transmitting and receiving antenna increases, the emanating wavefront created by the transmit antenna approximates a plane wave impinging on the receiving antenna with a decreasing amount of error. This scenario can be described geometrically using the labels from Figure A.4. When r is far away from the transmitting antenna:

$$(r + \Delta r)^2 = \left(\frac{z}{2}\right)^2 + r^2 \tag{A.23}$$

Expanding equation A.23:

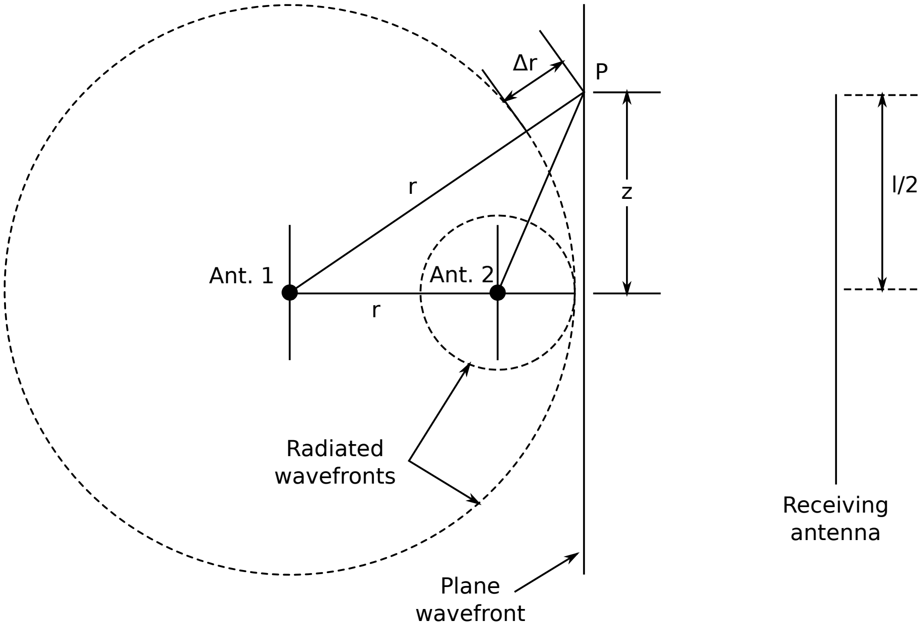

FIGURE A.4: Radiated wavefronts emanating from a transmit antenna and received at a separate antenna

$$r^2 + 2r\Delta r + \Delta r^2 = \frac{z^2}{4} + r^2 \tag{A.24}$$

Solving equation A.24 for r, the distance at which the phase wavefront is approximately a plane wave with a path length error of Δr results in:

$$r = \frac{z^2}{8\Delta r} - \frac{\Delta r}{2} \tag{A.25}$$

Assuming the path length error, Δr, is small, the expression for r becomes:

$$r \cong \frac{z^2}{8\Delta r} \tag{A.26}$$

The path length error, Δr, more specifically represents the difference in path length between the middle of the phase front and separate point P on the phase front. This difference in path length is the source of errors at the receiving antenna, which are mainly due to phase deviations. Errors arise from amplitude differences as well, but are negligible when compared to the errors resulting from phase differences. The path length difference, Δr, is determined by expressing its value in terms of the fraction of a wavelength that produces phase errors within the maximum tolerable error for the given scenario. Defining this error effectively defines the boundary between the near field and the far field.

In the previous section, the criteria for the path difference required it to be no larger than an eighth of a wavelength in order to fall within acceptable measurement error. This threshold, when applied from the viewpoint of the phase wavefront, corresponds to $\Delta r = \frac{\lambda}{8}$, and when substituted into equation A.26, the far field begins at a distance of:

$$r \cong \frac{z^2}{\lambda} = \frac{D^2}{\lambda} \tag{A.27}$$

for $z = D$, the maximum length of the receiving antenna.

Another criteria for the path difference that produces a tolerable amount of error is the Rayleigh criteria [82], which is the generally accepted criterion for the minimal resolvable detail. In terms of microwave scattering, the Rayleigh criteria states that the phase error should be no greater than one-sixteenth of a wavelength. Thus, $\Delta r = \frac{\lambda}{16}$, and the far field begins at a distance of:

$$r \cong \frac{2z^2}{\lambda} = \frac{2D^2}{\lambda} \tag{A.28}$$

This distance for the beginning of the far field is the same expression derived from the viewpoint of the parameters of the antenna. As with the computed distance for the near field/far field boundary from the viewpoint of the antenna parameters, there is a direct dependence on the tolerable measurement error and desired accuracy. Various boundaries and accuracies are documented in Table A.1.

Emphasis must be placed on the fact that the computed boundaries between the near field and the far field in this section are guidelines, directly dependent on the tolerable measurement error and desired accuracy. The relationship between the path loss, distance from the antenna, and the corresponding radiation zone holds true for antennas of any shape and size. Determining the true location of each radiation zone is accomplished through accurate measurement of the changing path loss slope of the emitted field.

Appendix B

Maxwell's Equations & Constitutive Relations

Maxwell's equations are included here for completeness. For an in-depth explanation, see [30].

B.1 Differential Form

B.1.1 Time-Varying Fields

For the time-varying differential form of Maxwell's equations, the instantaneous field values are functions of both time and space, i.e. $\vec{\mathcal{H}} = \vec{\mathcal{H}}\left(x, y, z; t\right)$.

$$\nabla \times \vec{\mathcal{E}} = -\vec{\mathcal{M}}_i - \frac{\partial \vec{\mathcal{B}}}{\partial t} = -\vec{\mathcal{M}}_i - \vec{\mathcal{M}}_d \tag{B.1}$$

$$\nabla \times \vec{\mathcal{H}} = \vec{\mathcal{J}}_i + \vec{\mathcal{J}}_c + \frac{\partial \vec{\mathcal{D}}}{\partial t} = \vec{\mathcal{J}}_i + \vec{\mathcal{J}}_c + \vec{\mathcal{J}}_d \tag{B.2}$$

$$\nabla \cdot \vec{\mathcal{D}} = \mathcal{Q}_{ev} \tag{B.3}$$

$$\nabla \cdot \vec{\mathcal{B}} = \mathcal{Q}_{mv} \tag{B.4}$$

where $\vec{\mathcal{J}}_d = \frac{\partial \vec{\mathcal{D}}}{\partial t}$ and $\vec{\mathcal{M}}_d = \frac{\partial \vec{\mathcal{B}}}{\partial t}$

B.1.2 Time-Harmonic Fields

In many practical systems utilizing EM waves, the variations of the fields are sinusoidal. These field variations are often referenced as time-harmonic fields. This sinusoidal variation can be represented by[1] $e^{j\omega t}$, which allows a simple relationship between the time-varying fields and their complex counterparts as follows:

$$\vec{\mathcal{E}}\left(x, y, z; t\right) = \mathrm{Re}\left[\vec{E}\left(x, y, z\right) e^{j\omega t}\right] \tag{B.5}$$

$$\vec{\mathcal{H}}\left(x, y, z; t\right) = \mathrm{Re}\left[\vec{H}\left(x, y, z\right) e^{j\omega t}\right] \tag{B.6}$$

$$\vec{\mathcal{D}}\left(x, y, z; t\right) = \mathrm{Re}\left[\vec{D}\left(x, y, z\right) e^{j\omega t}\right] \tag{B.7}$$

$$\vec{\mathcal{B}}\left(x, y, z; t\right) = \mathrm{Re}\left[\vec{B}\left(x, y, z\right) e^{j\omega t}\right] \tag{B.8}$$

$$\vec{\mathcal{J}}\left(x, y, z; t\right) = \mathrm{Re}\left[\vec{J}\left(x, y, z\right) e^{j\omega t}\right] \tag{B.9}$$

$$\mathcal{Q}_{ev}\left(x, y, z; t\right) = \mathrm{Re}\left[q_{ev}\left(x, y, z\right) e^{j\omega t}\right] \tag{B.10}$$

$$\mathcal{Q}_{mv}\left(x, y, z; t\right) = \mathrm{Re}\left[q_{mv}\left(x, y, z\right) e^{j\omega t}\right] \tag{B.11}$$

The time-harmonic form of Maxwell's equations can be be formed from the time-varying equations by replacing the instantaneous field vectors with their complex spatial counterparts, and by replacing $\partial/\partial t$ by $j\omega$ (due to the time dependence being represented by $e^{j\omega t}$) as follows:

---

[1] Time-harmonic fields may also be represented by $e^{-j\omega t}$, which is often seen in physics literature. All time varying fields in this document are of the $e^{j\omega t}$ form, a common engineering practice.

$$\nabla \times \vec{E} = -\vec{M}_i - j\omega\vec{B} \tag{B.12}$$

$$\nabla \times \vec{H} = \vec{J}_i + \vec{J}_c + j\omega\vec{D} \tag{B.13}$$

$$\nabla \cdot \vec{D} = q_{ev} \tag{B.14}$$

$$\nabla \cdot \vec{B} = q_{mv} \tag{B.15}$$

B.2 Constitutive Relations

The constitutive relations represent, on a macroscopic scale, the interaction between the charged particles in a material and EM fields. The following relationships are represented in the frequency domain. In the time domain, the products become convolutions.

$$\vec{D} = \epsilon\vec{E} \tag{B.16}$$

$$\vec{B} = \mu\vec{H} \tag{B.17}$$

$$\vec{J}_c = \sigma_s\vec{E} \tag{B.18}$$

Appendix C

Derivation of the Wave Equation

The derivation of the electromagnetic wave equation is included here for completeness.

C.1 Time-Varying Electromagnetic Fields

Taking the curl of both sides of equations B.1 and B.2, incorporating the constitutive relations and assuming a homogenous medium, it can be written that:

$$\nabla \times \nabla \times \vec{\mathcal{E}} = -\nabla \times \vec{\mathcal{M}}_i - \mu \nabla \times \left(\frac{\partial \vec{\mathcal{H}}}{\partial t} \right) = -\nabla \times \vec{\mathcal{M}}_i - \mu \frac{\partial}{\partial t} \left(\nabla \times \vec{\mathcal{H}} \right) \tag{C.1}$$

$$\nabla \times \nabla \times \vec{\mathcal{H}} = \nabla \times \vec{\mathcal{J}}_i + \sigma_e \nabla \times \vec{\mathcal{E}} + \epsilon' \nabla \times \left(\frac{\partial \vec{\mathcal{E}}}{\partial t} \right) \tag{C.2}$$

$$= \nabla \times \vec{\mathcal{J}}_i + \sigma_e \nabla \times \vec{\mathcal{E}} + \epsilon' \frac{\partial}{\partial t} \left(\nabla \times \vec{\mathcal{E}} \right) \tag{C.3}$$

Substituting equation B.2 into equation C.1 and using the following vector identity

$$\nabla \times \nabla \times \vec{A} = \nabla \left(\nabla \cdot \vec{A} \right) - \nabla^2 \vec{A} \tag{C.4}$$

equation C.1 can be written as:

$$\nabla \left(\nabla \cdot \vec{\mathcal{E}} \right) - \nabla^2 \vec{\mathcal{E}} = -\nabla \times \vec{\mathcal{M}}_i - \mu \frac{\partial}{\partial t} \left[\vec{\mathcal{J}}_i \sigma_e \vec{\mathcal{E}} + \epsilon' \frac{\partial \vec{\mathcal{E}}}{\partial t} \right] \tag{C.5}$$

$$= -\nabla \times \vec{\mathcal{M}}_i - \mu \frac{\partial \vec{\mathcal{J}}_i}{\partial t} - \mu \sigma_e \frac{\partial \vec{\mathcal{E}}}{\partial t} - \mu \epsilon' \frac{\partial^2 \vec{\mathcal{E}}}{\partial t^2} \tag{C.6}$$

Using equation B.3 and substituting the constitutive relation in equation B.16 results in:

$$\nabla \cdot \vec{\mathcal{D}} = \mathcal{Q}_{ev} \quad \Rightarrow \quad \epsilon \nabla \cdot \vec{\mathcal{E}} = \mathcal{Q}_{ev} \quad \Rightarrow \quad \nabla \cdot \vec{\mathcal{E}} = \frac{\mathcal{Q}_{ev}}{\epsilon} \tag{C.7}$$

Substituting equation C.7 into equation C.5, the vector wave equation for the electric field is determined as follows:

$$\nabla^2 \vec{\mathcal{E}} = \nabla \times \vec{\mathcal{M}}_i + \mu \frac{\partial \vec{\mathcal{J}}_i}{\partial t} + \frac{1}{\epsilon} \nabla \mathcal{Q}_{ev} + \mu \sigma_e \frac{\partial \vec{\mathcal{E}}}{\partial t} + \mu \epsilon' \frac{\partial^2 \vec{\mathcal{E}}}{\partial t^2} \tag{C.8}$$

Similarly, the vector wave equation for the magnetic field can be determined by substituting equation B.1 into equation C.2 and using the vector identity in equation C.4, which results in:

$$\nabla \left(\nabla \cdot \vec{\mathcal{H}} \right) - \nabla^2 \vec{\mathcal{H}} = \nabla \times \vec{\mathcal{J}}_i + \sigma_e \left(-\vec{\mathcal{M}}_i - \mu \frac{\partial \vec{\mathcal{H}}}{\partial t} \right) + \epsilon' \frac{\partial}{\partial t} \left(-\vec{\mathcal{M}}_i - \mu \frac{\partial \vec{\mathcal{H}}}{\partial t} \right) \tag{C.9}$$

$$= \nabla \times \vec{\mathcal{J}}_i - \sigma_e \vec{\mathcal{M}}_i - \mu \sigma_e \frac{\partial \vec{\mathcal{H}}}{\partial t} - \epsilon' \frac{\partial \vec{\mathcal{M}}_i}{\partial t} - \mu \epsilon' \frac{\partial^2 \vec{\mathcal{H}}}{\partial t^2} \tag{C.10}$$

Equation B.4 and B.17 results in:

$$\nabla \cdot \vec{\mathcal{B}} = \mathcal{Q}_{mv} \quad \Rightarrow \quad \mu \nabla \cdot \vec{\mathcal{H}} = \mathcal{Q}_{mv} \quad \Rightarrow \quad \nabla \cdot \vec{\mathcal{H}} = \frac{\mathcal{Q}_{mv}}{\mu} \tag{C.11}$$

Substituting equation C.11 into equation C.9 results in the vector wave equation for the magnetic field as follows:

$$\nabla^2 \vec{H} = -\nabla \times \vec{\mathcal{J}}_i + \sigma_e \vec{\mathcal{M}}_i + \frac{1}{\mu} \nabla \left(\mathcal{Q}_{mv} \right) + \epsilon' \frac{\partial \vec{\mathcal{M}}_i}{\partial t} + \mu \sigma_e \frac{\partial \vec{\mathcal{H}}}{\partial t} + \mu \epsilon' \frac{\partial^2 \vec{\mathcal{H}}}{\partial t^2} \tag{C.12}$$

For source-free regions, where $\vec{\mathcal{J}}_i = \mathcal{Q}_{ev} = \vec{\mathcal{M}}_i = \mathcal{Q}_{mv} = 0$, the vector wave equations in equations C.8 and C.12 reduce to, respectively:

$$\nabla^2 \vec{\mathcal{E}} = \mu \sigma_e \frac{\partial \vec{\mathcal{E}}}{\partial t} + \mu \epsilon' \frac{\partial^2 \vec{\mathcal{E}}}{\partial t^2} \tag{C.13}$$

$$\nabla^2 \vec{\mathcal{H}} = \mu \sigma_e \frac{\partial \vec{\mathcal{H}}}{\partial t} + \mu \epsilon' \frac{\partial^2 \vec{\mathcal{H}}}{\partial t^2} \tag{C.14}$$

C.1.1 Wave Propagation Speed

Based on the standard mathematical definition of a wave equation, the propagation speed of the wave, v, can be defined as follows:

$$v = \frac{1}{\sqrt{\mu' \epsilon'}} = \frac{1}{\sqrt{\mu_0 \epsilon_0 \mu_r' \epsilon_r'}} \tag{C.15}$$

Using the speed of light in a vacuum, defined as $c = \frac{1}{\sqrt{\mu_0 \epsilon_0}} \approx 2.998 \times 10^8$ meters/sec, equation C.15 can be simplified to:

$$v = \frac{1}{\sqrt{\mu_0 \epsilon_0}} \frac{1}{\sqrt{\mu_r' \epsilon_r'}} = \frac{c}{\sqrt{\mu_r' \epsilon_r'}} \tag{C.16}$$

Thus, the wave propagation speed of EM waves in a specific medium scales the wave propagation speed in a vacuum by the medium's dielectric properties.

C.2 Time-Harmonic Electromagnetic Fields

The wave equation for time-harmonic EM fields can be derived from the time-varying fields by replacing the time-varying field vector components with their spatial counterparts, and by replacing $\partial/\partial t \equiv j\omega$, $\partial^2/\partial t^2 \equiv (j\omega)^2 = -\omega^2$. Using these relationships in equations C.13 and C.14, the vector wave equations for time-harmonic fields are determined as follows:

$$\nabla^2 \vec{E} = j\omega\mu\sigma_e \vec{E} - \omega^2 \mu\epsilon' \vec{E} = \gamma^2 \vec{E} \tag{C.17}$$

$$\nabla^2 \vec{H} = j\omega\mu\sigma_e \vec{H} - \omega^2 \mu\epsilon' \vec{H} = \gamma^2 \vec{H} \tag{C.18}$$

where

$$\gamma^2 = j\omega\mu\sigma_e - \omega^2\mu\epsilon' = j\omega\mu\left(\sigma_e + j\omega\epsilon'\right) \tag{C.19}$$

$$\gamma = \alpha + j\beta \tag{C.20}$$

The propagation constant, γ, represents the phase and attenuation constants of a wave in a specific medium due to dielectric effects.

Appendix D

Publications

All publications to date are listed below, including those in progress.

[**1**] **J. S. Besnoff**, M. Reynolds, "Near Field Modulated Backscatter For *in vivo* Biotelemetry," in *2012 IEEE International Conference on RFID (RFID)*, April 2012, pp. 135 - 140.
[**2**] S. Thomas, **J. S. Besnoff**, and M. Reynolds, "Modulated Backscatter for Ultra-low Power Uplinks from Wearable and Implantable Devices," in *2012 ACM MedCOMM: Workshop on Medical Communication Systems*, pp. 1 - 6.
[**3**] **J. S. Besnoff**, T. Deyle, R. R. Harrison, M. S. Reynolds, "Battery-Free Multichannel Digital ECG Biotelemetry Using UHF RFID Techniques," in *2013 IEEE International Conference on RFID (RFID)*, April 2013, pp. 16 - 22.
[**4**] **J. S. Besnoff**, and M. S. Reynolds, "Single-Wire RF Transmission Lines for Implanted Devices," in *2013 IEEE Biomedical Circuits and Systems Conference*, October 2013.

In progress:

[**5**] **J. S. Besnoff**, T. Deyle, S. J. Thomas, and M. S. Reynolds, "Near Field Ultra-High Frequency (UHF) Backscatter Biotelemetry," in *IEEE Transactions on Microwave Theory and Techniques*, (In Progress).

[6] J. S. Besnoff, and M. S. Reynolds, “Single-Wire RF Transmission Lines In Biological Tissue,” in *Applied Physics Letters*, (In Review).

Bibliography

[1] P. J. Ifft, S. Shokur, Z. Li, M. A. Lebedev, and M. A. L. Nicolelis, “A brain-machine interface enables bimanual arm movements in monkeys,” *Science Translational Medicine*, November 2013.

[2] S. Thomas, R. Harrison, A. Leonardo, and M. Reynolds, “A battery-free multichannel digital neural/EMG telemetry system for flying insects,” in *2011 IEEE Biomedical Circuits and Systems Conference (BioCAS)*, November 2011, pp. 229–232.

[3] S. Thomas, R. R. Harrison, A. Leonardo, and M. S. Reynolds, “A battery-free multichannel digital neural/EMG telemetry system for flying insects,” *IEEE Transactions on Biomedical Circuits and Systems*, vol. 6, no. 5, pp. 424–436, October 2012.

[4] D. Yeager, F. Zhang, A. Zarrasvand, N. George, T. Daniel, and B. Otis, “A 9 μ a, addressable Gen 2 sensor tag for biosignal acquisition,” *IEEE Journal of Solid-State Circuits*, vol. 45, no. 10, pp. 2198–2209, October 2010.

[5] E. Chow, A. Chlebowski, S. Chakraborty, W. Chappell, and P. Irazoqui, “Fully wireless implantable cardiovascular pressure monitor integrated with a medical stent,” *IEEE Transactions on Biomedical Engineering*, vol. 57, no. 6, pp. 1487–1496, 2010.

[6] L. Rousseau, E. Scorsone, A. Bendali, M. Djilas, H. Girard, M. Cottance, S. Joucla, E. Dubus, J. Degardin, B. Yvert, G. Lissorgues, P. Bergonzo, and S. Picaud, “Soft 3D retinal implants with diamond electrode a way for focal stimulation,” in *The 17th International Conference on Solid-State Sensors, Actuators and Microsystems (TRANSDUCERS EUROSENSORS XXVII), 2013 Transducers Eurosensors XXVII*, June 2013, pp. 1227–1230.

[7] W. G. Scanlon, B. Burns, and N. E. Evans, “Radiowave propagation from a tissue-implanted source at 418 MHz and 916.5 MHz,” *IEEE Transactions on Biomedical Engineering*, vol. 47, no. 4, pp. 527–534, April 2000.

[8] J. I. Agbinya, *Wireless Power Transfer.* River Publishers, 2012.

[9] K. Keikhosravy, P. Kamalinejad, S. Mirabbasi, K. Takahata, and V. Leung, “An ultra-low-power monitoring system for inductively coupled biomedical implants,” in *2013 IEEE International Symposium on Circuits and Systems (ISCAS)*, May 2013, pp. 2283–2286.

[10] M. Zaheer, J. Suri, and H. Nemade, “Primary side control based inductively coupled powering scheme for biomedical implants,” in *2012 IEEE-EMBS International Conference on Biomedical and Health Informatics (BHI)*, January 2012, pp. 174–179.

[11] Y.-X. Guo and R. Jegadeesan, “Efficient inductive power transfer for biomedical applications,” in *2012 IEEE International Workshop on Electromagnetics; Applications and Student Innovation (iWEM)*, August 2012, pp. 1–2.

[12] S. Kim, J. Ho, L. Y. Chen, and A. Poon, “Wireless power transfer to a cardiac implant,” *Applied Physics Letters*, vol. 101, no. 7, pp. 073 701–073 701–4, August 2012.

[13] H. Ali, T. Ahmad, and S. Khan, “Inductive link design for medical implants,” in *IEEE Symposium on Industrial Electronics Applications, 2009. ISIEA 2009.*, vol. 2, October 2009, pp. 694–699.

[14] M. Ghovanloo and S. Atluri, “An integrated full-wave CMOS rectifier with built-in back telemetry for RFID and implantable biomedical applications,” *IEEE Transactions on Circuits and Systems -I: Regular Papers*, vol. 55, no. 10, pp. 3328–3334, November 2008.

[15] Federal Communications Commission, “FCC table of frequency allocations,” July 2014.

[16] K. Finkenzeller, *RFID Handbook*, 2nd ed. Chapter 3, pages 42-43: Wiley, 2003.

[17] A. L. Owens, T. J. Denison, H. Versnel, M. Rebbert, M. Peckerar, and S. A. Shamma, “Multi-electrode array for measuring evoked potentials from surface of ferret primary auditory cortex,” *Journal of Neuroscience Methods*, vol. 58, pp. 209–220, 1995.

[18] R. Harrison, “The design of integrated circuits to observe brain activity,” *Proceedings of the IEEE*, vol. 96, no. 7, pp. 1203–1216, July 2008.

[19] K. Cha, K. Horch, and R. Normann, “Simulation of a phosphine based visual field: Visual acuity in a pixelized vision system,” *Annals of Biomedical Engineering*, vol. 20, no. 4, pp. 439–449, 1992.

[20] J. Weiner. (2003, December) Sight seeing. USC health magazine. [Online]. Available: http://www.usc.edu/hsc/info/pr/hmm/win03/sight.html

[21] E. e. a. Margalit, "Retinal prosthesis for the blind," *Survey Ophthalmology*, vol. 47, no. 4, pp. 335–356, 2002.

[22] M. Ghovanloo and S. Atluri, "A wide-band power-efficient inductive wireless link for implantable microelectronic devices using multiple carriers," *IEEE Transactions on Circuits and Systems I: Regular Papers*, vol. 54, no. 10, pp. 2211–2221, 2007.

[23] C. T. Nordhausen, E. M. Maynard, and R. A. Normann, "Single unit recording capabilities of a 100 microelectrode array," *Brain Research*, vol. 726, pp. 129–140, March 1996.

[24] K. D. Wise, D. J. Anderson, J. F. Hetke, D. R. Kipke, and K. Najafi, "Wireless implantable microsystems: High-density electronic interfaces to the nervous system," vol. 92, no. 1. Proceedings of the IEEE, January 2004, pp. 76–97.

[25] M. A. L. Nicolelis, D. Dimitrov, J. M. Carmena, R. Crist, G. Lehew, J. D. Kralik, and S. P. Wise, "Chronic, multisite, multielectrode recordings in macaque monkeys," *Proceedings of the National Academy of Sciences (PNAS)*, pp. 11 041–11 046, 2003.

[26] Federal Communications Commission, "OET bulletin 65: Evaluating compliance with FCC guidelines for human exposure to radiofrequency electromagnetic fields," August 1997.

[27] R. R. Harrison, P. T. Watkins, R. J. Kier, R. O. Lovejoy, D. J. Black, B. Greger, and F. Solzbacher, "A low-power integrated circuit for a wireless 100-electrode neural recording system," *IEEE Journal of Solid-State Circuits*, vol. 42, no. 1, pp. 123–133, January 2007.

[28] R. R. Harrison, H. Fotowat, R. Chan, R. J. Kier, R. Olberg, A. Leonardo, and F. Gabbiani, "Wireless neural/EMG telemetry systems for small freely moving animals," *IEEE Transactions on Biomedical Circuits and Systems*, vol. 5, no. 2, pp. 103 – 111, April 2011.

[29] C. A. Balanis, *Antenna Theory.* Wiley-Interscience, 2005.

[30] ——, *Advanced Engineering Electromagnetics.* John Wiley & Sons, 1989.

[31] P. J. Bevelacqua. (2011). [Online]. Available: www.antenna-theory.com

[32] D. Staelin, "Receivers, antennas, and signals," MIT OpenCourseWare, Tech. Rep., 2003.

[33] H. Friis, "A note on a simple transmission formula," *Proceedings of the IRE*, vol. 34, no. 5, pp. 254–256, May 1946.

[34] S. Gabriel, R. Lau, and C. Gabriel, "The dielectric properties of biological tissues ii: Measurements in the frequency range 10 hz to 20 ghz," *Physics in Medicine and Biology*, vol. 41, pp. 2251–2269, 1996.

[35] D. Andreuccetti, R. Fossi, and C. Petrucci. (1997) An internet resource for the calculation of the dielectric properties of body tissues in the frequency range 10 Hz - 100 GHz. [Online]. Available: http://niremf.ifac.cnr.it/tissprop/

[36] M. Mollazadeh, K. Murari, H. Schwerdt, X. Wang, N. Thakor, and G. Cauwenberghs, "Wireless multichannel acquisition of neuropotentials," in *Biomedical Circuits and Systems Conference (BioCAS 2008).* Baltimore, MD: IEEE, November 2008, pp. 49–52.

[37] S. Mandal and R. Sarpeshkar, "Power-efficient impedance-modulation wireless data links for biomedical implants," *IEEE Transactions on Biomedical Circuits and Systems*, vol. 2, no. 4, pp. 301–315, December 2008.

[38] Y. Hu and M. Sawan, "A fully integrated low-power BPSK demodulator for implantable medical devices," *IEEE Transactions on Circuits and Systems -I: Regular Papers*, vol. 52, no. 12, pp. 2552–2562, December 2005.

[39] X. Qing, C. Goh, and Z. Chen, "A broadband UHF near-field RFID antenna," *IEEE Transactions on Antennas and Propagation*, vol. 58, no. 12, pp. 3829–3838, December 2010.

[40] A. Stogryn, "Equations for calculating the dielectric constant of saline water," *IEEE Transactions on Microwave Theory and Techniques*, vol. 19, no. 8, pp. 733–736, 1971.

[41] "Wideband 2.5 GHz, 37 dB isolation at 1 GHz, CMOS 1.65 v to 2.75 v, 4:1 mux/SP4T," Analog Devices ADG904 Datasheet, 2007.

[42] M. Mark, T. Bjö Andrninen, L. Ukkonen, L. Sydä andnheimo, and J. Rabaey, "SAR reduction and link optimization for mm-size remotely powered wireless implants using segmented loop antennas," in *2011 IEEE Topical Conference on Biomedical Wireless Technologies, Networks, and Sensing Systems (BioWireleSS)*, January 2011, pp. 7 –10.

[43] E. Moradi, T. Bjorninen, L. Sydanheimo, L. Ukkonen, and J. Rabaey, "Analysis of wireless powering of mm-size neural recording tags in RFID-inspired wireless brain-machine interface systems," in *2013 IEEE International Conference on RFID (RFID)*, 2013, pp. 8–15.

[44] S. Ahmed and T. Kwasniewski, "Overview of oversampling clock and data recovery circuits," in *Canadian Conference on Electrical and Computer Engineering, 2005.* IEEE, 2005, pp. 1876–1881.

[45] D. M. Pozar, *Microwave Engineering*, 3rd ed. Wiley, 2005.

[46] [Online]. Available: http://www.fao.org/docrep/T0667E/t0667e05.htm

[47] S. M. H. Saif, Y. Lan, and S. Wang, "Electrical resistivity of chicken meat and pork chop," *ASABE Paper No. 046030. St. Joseph, Mich.: ASABE*, 2004.

[48] A. S. Y. Poon, S. O'Driscoll, and T. H. Meng, "Optimal frequency for wireless power transmission into dispersive tissue," *IEEE Transactions on Antennas and Propagation*, vol. 58, no. 5, pp. 1739–1749, May 2010.

[49] M. Kiani and M. Ghovanloo, "The circuit theory behind coupled-mode magnetic resonance-based wireless power transmission," *IEEE Transactions on Circuits and Systems —I: Regular Papers*, vol. 59, no. 9, pp. 2065–2074, September 2012.

[50] G. Goubau, "Surface waves and their application to transmission lines," *Journal of Applied Physics*, vol. 21, November 1950.

[51] A. Sommerfeld, "Propagation of electro-dynamic waves along a cylindric conductor," *Ann. der Physik und Chemie*, vol. 67, pp. 233–290, December 1899.

[52] J. Zenneck, "About the propagation of electromagnetic plane waves along a conductor plane and their relationship to wireless telegraphy," *Ann. der Physik*, vol. 23, pp. 846–866, September 1907.

[53] B. Rama Rao, "Subnanosecond pulse propagation in a Goubau line immersed in a lossy dielectric medium," *Electronics Letters*, vol. 20, no. 4, pp. 162–164, 1984.

[54] G. John, R. Chatterjee, and S. K. Chatterjee, "Surface wave characteristics of a lossy dielectric-coated conductor immersed in a lossy dielectric medium," *India, IEE-IERE Proceedings*, vol. 12, no. 6, pp. 210–228, 1974.

[55] S. Saario, J. Lu, and D. Thiel, "Full-wave analysis of choking characteristics of sleeve balun on coaxial cables," *Electronics Letters*, vol. 38, no. 7, pp. 304–305, 2002.

[56] J. Chirba, "Experimental studies of the losses and radiations due to bend in the Goubau line," *IEEE Transactions on Microwave Theory and Techniques*, vol. 25, no. 2, 1977.

[57] J. S. Besnoff and M. S. Reynolds, "Near field modulated backscatter for in vivo biotelemetry," in *2012 IEEE International Conference on RFID (RFID)*, April 2012, pp. 135–140.

[58] S. M. D. et al, "Cervical intraspinal stimulation evokes robust forelimb movements before and after injury," *Journal of Neural Engineering*, 2013.

[59] S. Seran, T. Karacolak, and J. Donohoe, “A small implantable dual band biocompatible antenna for medical wireless telemetry applications,” in *2013 USNC-URSI Radio Science Meeting (Joint with AP-S Symposium)*, July 2013, pp. 212–212.

[60] S. Islam, K. Esselle, D. Bull, and P. Pilowsky, “Making a telemetry system implantable: Challenges and opportunities in antenna design,” in *Microwave Workshop Series on RF and Wireless Technologies for Biomedical and Healthcare Applications*, 2013, pp. 1–3.

[61] N. Ramli, M. Kamarudin, N. Samsuri, E. Ahyat, and N. Khamis, “A 4.8 GHz implantable small printed antenna for wireless implantable body area network applications,” in *2013 IEEE International RF and Microwave Conference (RFM)*, 2013, pp. 210–213.

[62] A. Treizebre, T. Akalin, and B. Bocquet, “Planar excitation of Goubau transmission lines for THz BioMEMS,” *IEEE Microwave and Wireless Components Letters*, vol. 15, no. 12, pp. 886 – 888, December 2005.

[63] T. Lecklider, “The world of the near field,” October 2005. [Online]. Available: http://www.evaluationengineering.com/search/article.php?aid=5446

[64] C. Capps, “Near field or far field?” *EDN*, pp. 95–102, August 2001.

[65] (2012, December) Tn-261 - safety code 6 (sc6) radio frequency exposure compliance evaluation template (uncontrolled enviornment exposure limits). [Online]. Available: http://www.ic.gc.ca/eic/site/smt-gst.nsf/eng/sf10112.html

[66] Wire antennas. [Online]. Available: www.ece.msstate.edu/~donohoe/ece4990notes4.pdf

[67] H. A. Wheeler, “Fundamental limits of small antennas,” 1947, pp. 1479 – 1484.

[68] G. Breed, “Basic principles of electrically small antennas,” *Journal of High Frequency Electronics*, pp. 50–53, 2007.

[69] D. B. Miron, *Small Antenna Design.* Newnes, 2006.

[70] T. Sarkar, E. Arvas, and S. Rao, “Application of FFT and the conjugate gradient method for the solution of electromagnetic radiation from electrically large and small conducting bodies,” *IEEE Transactions on Antennas and Propagation*, vol. 34, no. 5, pp. 635–640, May 1986.

[71] R. Bancroft, “Fundamental dimension limits of antennas,” *Centurion Wireless Technologies*, pp. 1–14.

[72] H. Ott, *Noise Reduction Techniques in Electronic Systems*, second edition ed. New York, NY: John Wiley Interscience, 1988.

[73] D. White, *EMI Control Methods and Techniques.* Gainesville, VA: Don White Consultants, 1981, vol. 1-5.

[74] B. Keiser, *Principles of Electromagnetic Compatibility.* Norwood, MA: Artech House, 1979.

[75] C. Paul, *Introduction to Electromagnetic Compatibility.* New York, NY: John Wiley Interscience, 1992.

[76] J. D. Kraus, *Antennas.* New York, NY: McGraw-Hill, 1950.

[77] B. Berkowitz, *Basic Microwaves.* New York, NY: Hayden, 1966.

[78] P. V. Nikitin, V. S. Rao, and S. Lazar, "An overview of near field UHF RFID," *IEEE International Conference on RFID*, pp. 167–174, March 2007.

[79] S. Laybros and P.-F. Combes, "On radiating-zone boundaries of short, lambda/2, and lambda dipoles," *IEEE Antennas and Propagation Magazine*, vol. 46, no. 5, pp. 53–64, 2004.

[80] K. Bakshi, A. Bakshi, and U. Bakshi, *Antennas And Wave Propagation*, 1st ed. Pune, India: Technical Publications Pune, 2009.

[81] "Antenna measurement theory: Introduction to antenna measurement," Agilent, Tech. Rep.

[82] I. H. Woodhouse, *Introduction to Microwave Remote Sensing*, ser. Chapter 5. Boca Raton, FL: CRC Press, 2006.

Biography

Jordan Seth Besnoff was born in Bridgeport, CT on January 28, 1987, and grew up in the small town of Branford, CT. After attending Branford High School and graduating as Valedictorian in 2005, he attended Tufts University in Medford, MA. In 2009, Jordan earned the Bachelor of Science in Electrical Engineering (BSEE) and graduated summa cum laude. While at Tufts, Jordan interned at MIT Lincoln Laboratory from 2008 to 2009, and decided that he wanted to pursue a post secondary degree. Jordan immediately enrolled at Duke University in 2009, and earned the Master of Science (MS) degree in 2012. Jordan then received the Ph.D degree from Duke University in 2014, and his dissertation *Exploiting Near Field and Surface Wave Propagation for Implantable devices* was completed under Dr. Matthew Reynolds.

While completing his graduate work, Jordan received a best paper award at the 2012 IEEE RFID conference for his work *Near Field Modulated Backscatter for in vivo Biotelemetry.* Jordan also won the “Rectenna Shootout!” competition at the 2013 IEEE RFID conference.

Jordan has been a student member of the IEEE since 2008, a member of Tau Beta Pi since 2007, and Eta Kappa Nu since 2008. After his graduate work at Duke, Jordan is going to be joining the lab of Dr. David Ricketts at NC State University as a postdoctoral researcher.